STRUCTURE-FUNCTION RELATIONSHIPS OF RNA AND PROTEIN IN SYNAPTIC PLASTICITY

Sarah A. Middleton

A DISSERTATION

in

Genomics and Computational Biology

Presented to the Faculties of the University of Pennsylvania

in

Partial Fulfillment of the Requirements for the

Degree of Doctor of Philosophy

2017

Supervisor of Dissertation

____

Junhyong Kim, Ph.D., Professor of Biology

Graduate Group Chairperson

____

Li-San Wang, Ph.D., Associate Professor of Pathology and Laboratory Medicine

Dissertation Committee

Li-San Wang, Ph.D., Associate Professor of Pathology and Laboratory Medicine (Chair)
Danielle Bassett, Ph.D., Associate Professor of Bioengineering
Russ Carstens, M.D., Associate Professor of Medicine
James Eberwine, Ph.D., Professor of Pharmacology
Isidore Rigoutsos, Ph.D., Professor of Pathology, Anatomy, and Cell Biology, Thomas Jefferson University

STRUCTURE-FUNCTION RELATIONSHIPS OF RNA AND PROTEIN IN SYNAPTIC

PLASTICITY

ACKNOWLEDGMENTS

I am extremely grateful to all the people who have helped and supported me throughout my graduate work: my advisor, Junhyong, who has been an inspiring and compassionate mentor; all of the members of the Kim lab, especially those who helped me get started in the wet lab (Chantal, Derek, Hoa, Jean), managed the computing resources (Jamie, Stephen), and shared computational advice and camaraderie in the dry lab (Hannah, Mugdha, Qin, Youngji); my thesis committee, for their extremely helpful advice and guidance; my collaborators, especially Joe and Kanishka, who helped with developing and testing the machine learning methods in Chapter 3 of this thesis; my fellow GCB students, for being an awesome and fun group of people—I will miss betraying each other during game nights!; and the GCB coordinators, Hannah and Maureen, for organizing events and keeping GCB running smoothly. I also want to give my sincerest thanks to my parents, who have always gone out of their way to support me; and to my husband, Julius, who can make me smile even when everything else seems to be going wrong (a regular occurrence in graduate school!). Finally, I gratefully acknowledge the Department of Energy Computational Science Graduate Fellowship (DE-FG02-97ER25308), which not only supported much of this work financially, but also provided me with amazing opportunities to expand my computational skills and knowledgebase and to interact with inspiring people in computational disciplines outside of my own.

ABSTRACT

STRUCTURE-FUNCTION RELATIONSHIPS OF RNA AND PROTEIN IN SYNAPTIC PLASTICITY

Sarah A. Middleton

Junhyong Kim

Structure is widely acknowledged to be important for the function of ribonucleic acids (RNAs) and proteins. However, due to the relative accessibility of sequence information compared to structure information, most large genomics studies currently use only sequence-based annotation tools to analyze the function of expressed molecules. In this thesis, I introduce two novel computational methods for genome-scale structure-function analysis and demonstrate their application to identifying RNA and protein structures involved in synaptic plasticity and potentiation—important neuronal processes that are thought to form the basis of learning and memory. First, I describe a new method for *de novo* identification of RNA secondary structure motifs enriched in co-regulated transcripts. I show that this method can accurately identify secondary structure motifs that recur across three or more transcripts in the input set with an average recall of 0.80 and precision of 0.98. Second, I describe a tool for predicting protein structural fold from amino acid sequence, which achieves greater than 96% accuracy on benchmarks and can be used to predict protein function and identify new structural folds. Importantly, both of these tools scale linearly with increasing numbers of input sequences, making them feasible to run on thousands of sequences at a time. Finally, I use these tools to investigate RNA localization and local translation in dendrites—two processes that are prerequisites for long-lasting synaptic potentiation. Using soma- and dendrite-specific RNA-sequencing data as a starting point, I define the full set of RNAs localized to the dendrites, identify novel secondary structure motifs enriched in these RNAs that may act as dendritic localization signals, and predict the structure of all proteins that would be produced by these localized RNAs during local translation. The results shed new light on potential regulatory mechanisms of dendritic localization and roles of locally translated proteins at the synapse, and demonstrate the utility of structure-based tools in genomics analysis.

TABLE OF CONTENTS

LIST OF TABLES

LIST OF FIGURES

Chapter 1: Introduction

As an introduction to the computational structure analysis tools and biological applications that will be presented in the main body of this thesis, I review here the basics of ribonucleic acid (RNA) secondary structure, protein tertiary structure, and the fundamental concepts of synaptic plasticity and long-term potentiation in neurons, focusing in particular on areas where structure analysis can yield new insight into biological function.

1.1. RNA structure

RNAs are versatile macromolecules that play a wide variety of roles in the cell—most notably as a mobile templates coding for proteins, but also sometimes as independent regulatory or catalytic molecules [1,2]. RNAs self-base pair to form various structures that help define their function and regulation. Below I review the basics of RNA structure, including how it can be predicted and examples of functional structures.

1.1.1. Overview

RNA is a single-stranded polymer made up of a chain of individual nucleotides, each composed of a ribose sugar with a phosphate group at the 5’ position, a nitrogenous base at the 1’ position, and hydroxyl groups at the 2’ and 3’ positions. Nucleotides are joined together by a phosphodiester bond between the phosphate group of one nucleotide and the 3’ hydroxyl of another. Thus the final RNA polymer has directionality, where one end has a free phosphate group (called the 5’ end) and the other end has a free hydroxyl (called the 3’ end). The 5’ end is considered the “beginning” of the molecule, since translation (the synthesis of protein from RNA) proceeds in a 5’ to 3’ direction.

There are four canonical types of bases used in RNA: adenine (A), guanine (G), cytosine (C), and uracil (U). Certain bases can form hydrogen bonds with each other to create base pairs. The standard “Watson-Crick” base pairs are G-C and A-U, but other pairings, most notably G-U “wobble” pairs [3], are also possible under certain conditions. Base pairing is energetically favorable, and therefore the single strand of a given RNA will tend to form base-pairing interactions with itself when possible. This causes each RNA to take on a shape determined by the base pairs that occur. The two-dimensional conformation of an RNA that results from base pairing is generally referred to as its “secondary structure”, whereas the linear sequence of nucleotides that make up the RNA is called its “primary structure”.

RNA secondary structures can be broken down into a relatively small set of building blocks. One of the most common building blocks is the stem-loop (or “hairpin”) structure. Stem-loops consist of a “stem” of consecutive paired bases, and a “loop” of at least three unpaired bases, where the single strand of RNA loops back around to pair with itself at the stem (Fig. 1-1A). Stem-loops are often interrupted by interior loops, which are regions of one or more unpaired bases within the stem; or by bulges, which are interior loops where only one side of the stem is unpaired. Branches may also occur where two or more stems split from a single stem, sometimes accompanied by internal loop (Fig. 1-1A).

The definition of secondary structure is generally restricted to only base pairing interactions that result in well-nested structures (i.e. interactions that do not cross over each other) (Fig. 1-1B). However, RNA structure also has an important three-dimensional component, referred to as its tertiary structure. For example, stem-type secondary structures form a helix in three-dimensional space (Fig. 1-1C), and this helix can have different properties and shapes depending on the combination of base pairs that form the stem and the presence of bulges or interior loops [4]. Non-nested base pairing interactions are also possible, including pseudoknots, which are regions of base pairing interactions that cross over each other (Fig. 1-1D), and G-quadruplexes, which are formed by interactions between repeated groups of guanines to form a four-stranded structure (Fig. 1-1E) [4].

1.1.2. RNA structure prediction

Experimental methods

Until recently, experimental methods for probing RNA secondary structure were relatively low-throughput. Classic methods include X-ray crystallography, nuclear magnetic resonance (NMR) spectroscopy, single-strand RNA (ssRNA)- or double strand RNA (dsRNA)-specific chemical modification followed by primer extension (e.g. SHAPE [5]), and ssRNA/dsRNA nuclease cleavage followed by fragment size analysis [6]. These methods, though accurate, are time consuming and difficult to apply to multiple RNAs in parallel. New methods for structure probing combine various chemical- and nuclease-based techniques with high-throughput RNA sequencing to greatly increase the number of RNAs that can be probed at once [7]. Although these methods show great promise, they do not always give complete information for all RNAs, and have not yet been applied to all species. Because of this, computational structure prediction methods continue to be developed to fill the holes in existing RNA structure data.

Computational methods

Given a set of parameter values defining the change in free energy associated with different base pairs (i.e. their stability), and assuming that all secondary structures will be well-nested, then the "optimal" secondary structure—that is, the structure with the minimum free energy (MFE)—for any given RNA sequence can be found in using a dynamic programming algorithm [8–12]. These thermodynamic modeling-based approaches are still widely used today to predict secondary structure in the absence of other sources of information. Although these methods are relatively fast, their main drawback is that the MFE structure is often not the structure taken on *in vivo*, due to external factors such as protein binding to the RNA or changes in environmental ion concentration [1]. The differences between the MFE structure and true *in vivo* structure are particularly apparent for longer (>700nt) sequences, for which only about 60% of predicted base pairs are estimated to be correct on average [1].

One way to improve the accuracy of *in silico* secondary structure prediction is to use comparative information across multiple homologous RNAs. If the structure of the RNA is functionally important, it may show a pattern of conservation called "covariation". Covariation is when there are compensatory base changes that maintain base-pairing potential of the sequence. In a multiple sequence alignment of homologous RNAs, this manifests as columns of the alignment with pairing-compatible changes—for example, when the base in one column changes from a G to an A, the base in the other column changes from C to U (Fig. 1-2). Such a change maintains the ability of the RNA to form a base pair between those particular bases. The observation of multiple compensatory changes across evolution provides strong evidence for *in vivo* base-pairing interactions, and can therefore be used to guide structure prediction [13–17]. Often, this is used in combination with thermodynamic modeling to arrive at the final structure prediction [18–21]. Although these covariation-based methods can be very accurate, they are much more computationally intensive than thermodynamic modeling alone due to the need to calculate a multiple alignment of the input sequences. This method is therefore not feasible for all applications, as will be discussed further in Chapter 2.

1.1.3. Structure-function relationships

One of the primary roles of RNA is to serve as a template for the creation of proteins. Within protein-coding RNAs, also known as messenger RNAs (mRNAs), three functionally distinct regions are defined: the coding region (CDS), which is the part of the mRNA that is translated into protein; the 5' untranslated region (UTR), which is upstream of the CDS and is not translated; and the 3'UTR, which is downstream of the CDS and also not translated. The 5'UTR is generally relatively short (a few hundred nucleotides (nt)), but can occasionally contain sequence and structure motifs that help recruit and position translational machinery, such as the ribosome, at the correct start site of the CDS [22–24]. The 3'UTR, on the other hand, is often much longer (up to several thousand nt) and contains a rich variety of sequence and structure motifs involved in various aspects of mRNA regulation, including subcellular localization, translation, and degradation [25].

There are several mechanisms by which secondary structures can play a functional role in the mRNA. Most prominently, structures often serve as binding sites for RNA-binding proteins (RBPs). Depending on the RBP, it may be the RNA structure itself that is recognized (e.g. binding of the RBP Staufen to dsRNA [26]), or the structure may help position a linear sequence of unpaired nucleotides (e.g. within a loop) into a more favorable position for recognition [27]. Once bound, RBPs can initiate and regulate a variety of different functions. For example, Staufen2 likely helps mediate dendritic localization of the RNAs to which it binds [28,29]. Another example is the ADAR (adenosine deaminase acting on RNA) RBPs, which bind to long stems of dsRNA and perform RNA editing to change adenines to inosines [30]. Conversely, a secondary structure can also function by occluding a binding site for an RBP or microRNA, blocking those molecules from binding. In rare cases, secondary structures mediate function by mimicking or replacing other molecules. For example, an mRNA from the cricket paralysis virus contains an internal ribosome entry site (IRES) that mimics the structure of tRNA-Met and forms a pseudoknot with the initiation codon. This allows the virus to initiate translation in the absence of canonical initiation factors [31,32].

Another large class of RNA is non-coding RNA (ncRNA), which includes functionally diverse subclasses such as microRNAs (miRNAs), transfer RNAs (tRNAs), ribosomal RNAs (rRNAs), long non-coding RNAs (lncRNAs), among others [33]. For these RNAs, structure is often a vital determinant of function [34]. For example, the cloverleaf structure of tRNA is strongly conserved across species, despite substantial variation on the sequence level (46% pairwise identity on average according to the Rfam database [35]), which allows it to associate with the ribosome. In the case of ribozymes, such as 23S rRNA, RNaseP, and self-splicing introns, the structure of the RNA actually confers independent catalytic activity to the RNA [33]. For other ncRNAs, structure plays the most important role during biogenesis. Examples of this are the hairpin structures of pri- and pre-miRNA that are necessary for cleavage into mature miRNA by Drosha and Dicer proteins [36]. There are many more examples of functional ncRNA structures in the literature, and many families of such structures have been compiled into the Rfam database [35].

There are two particular ideas worth noting regarding the structure-function relationship of RNA. The first is that if we know of a structure that plays a functional role in one RNA, we can search the transcriptome for similar structures to identify other RNAs that have a common function (in the case of ncRNAs) or are co-regulated by the same RBP or pathway (in the case of mRNA regulatory motifs). This is the basis of the Rfam database [35], which uses covariance models—a type of stochastic context-free grammar that can model both sequence and secondary structure—to scan for new instances of known functional structures. Secondly, and relatedly, if we know a set of mRNAs are co-regulated, we can look for structural motifs shared between them to find candidates for the regulatory element or RBP binding site. Computational methods for performing this particular kind of analysis are currently lacking due to the difficulty of obtaining accurate structure predictions for large datasets and the difficulty of measuring the notion of similar secondary structures. This problem will be addressed in Chapter 2.

1.2. Protein structure

Proteins are the main workhorses of the cell, participating in almost all aspects of cellular function, including gene expression, energy production, signaling, catalysis, transport, and cytoskeleton formation. Structure is an indispensable aspect of function for almost all proteins, and even small disruptions of structure can lead to serious diseases [37]. In this section, I review the basics of protein structure-function relationships and how they can be predicted.

1.2.1. Overview

A protein is composed of a linear chain of amino acid residues linked by peptide bonds between the carboxyl group of one amino acid and the amino group of the next. There are 20 canonical amino acids that vary in size, charge, hydrophobicity, polarity, and modifiability. The unique combination and ordering of residues in a protein are the basis for protein structure and function.

Protein structure is often described as having four levels: primary, secondary, tertiary, and quaternary. The primary structure is simply the linear sequence of amino acids making up the protein. The secondary structure is defined as the local patterns of hydrogen bonding between a carboxyl oxygen and amino hydrogen of nearby residues. The most common and stable secondary structures are the α-helix [38] and β-sheet [39], but other conformations such as coils and turns are also observed. Tertiary structure is the full three-dimensional conformation of the protein, which is stabilized by covalent interactions, hydrogen bonds, hydrophobic interactions, van de Waals forces, electrostatic interactions, and repulsive forces. It is the tertiary structure that is considered most important for overall function of most proteins, although individual primary and secondary features can also have functional roles. Finally, the quaternary structure refers to the organization of multiple separate protein chains into a functional complex.

Many proteins have smaller subregions called domains. In the context of structural biology, a domain is usually defined as a compact, stable, independent folding unit [40]—that is, if the domain sequence were to be cleaved from the rest of the protein, it would still take on its native, stable tertiary structure. Alternatively, in the context of evolutionary sequence analysis, a domain is defined as a conserved region of the protein sequence, often with a conserved function (for example, the domains defined in the Pfam database [41] are of this type). It is important to note that in practice these two definitions often coincide, since structural domains are usually evolutionarily conserved and have a specific function [40]. The definition of a structural domain is broader, however, because it is possible for non-homologous sequences to have the same structure. In this thesis, I will primarily use the word "domain" to refer to the union of these definitions, and specify "structural domain" or "sequence domain" when distinction is necessary.

A remarkable feature of domains is their modularity. Most proteomes appear to be composed of a finite library of domains that have been "mixed and matched" to produce various functional combinations within multi-domain proteins [40]. Due to accumulated sequence variation over time, the instances of a domain have varying levels of sequence similarity across different proteins and species. Many domains have become so diverged that it is impossible to recognize them based on sequence alone. In these cases, structural information can be used to identify domains, because structure is usually more conserved than sequence [42]. Given the complexity of relationships between domains, several hierarchical classification schemes have been created to organize domain instances (that is, individual observations of a domain in a protein) based on defined levels of similarity and evolutionary relationship. The Structural Classification of Proteins (SCOP) database, for example, manually curates groups of domains on four main levels: family, superfamily, fold, and class [43]. "Families" group together homologous domains with highly similar sequence and closely related function (although there can be fine-grained functional differences between members of a family, such as different binding preferences for DNA-binding domains). "Superfamilies" group together families with more divergent, but still recognizable, sequence similarities. Superfamilies also tend to have a general conserved function. The next level is "fold", which groups together superfamilies with similar tertiary structures (that is, similar numbers and topological arrangements of secondary structures). Folds are defined purely based on structure, and it is not always clear if the constituent superfamilies are related evolutionarily or have arrived at similar structures by convergent evolution. Nonetheless, members of a fold typically still have similar coarse-grain functions, with the exception of some highly diversified and prevalent "superfolds", which have been adapted to a variety of distinct purposes [44]. Interestingly, there appears to be a limited number of folds used by natural proteins—only a little over 1,000 folds are currently defined, and the rate of new fold discoveries has steadily declined over the past few years. Finally, the "class" level of SCOP groups folds very roughly based on overall secondary structure composition and other properties, such as all-α-helix, all-β-sheet, mixed-α-β, membrane proteins, and a few others. Overall, this taxonomically-inspired classification scheme (and others, such as CATH [45]) provides a convenient discretization of domain similarity that enables analysis at defined levels of evolutionary and structural relationship.

1.2.2. Protein structure prediction

Experimental methods

Protein tertiary structure can be experimentally determined ("solved") using several methods, most commonly X-ray crystallography and NMR spectroscopy. X-ray crystallography requires purification and crystallization of the protein of interest, which is then exposed to X-rays to obtain a diffraction pattern. This diffraction pattern is analyzed to infer the location of atoms in the structure. Although crystallography can be very accurate, it is limited by the difficulty of obtaining protein crystals. Proteins with flexible domains are particularly difficult to crystalize, and must be split into non-flexible fragments to obtain partial crystal structures. NMR spectroscopy, on the other hand, is well-suited for flexible proteins, since it works on proteins in solution and does not require crystallization. NMR spectroscopy measures atomic resonance while exposing the protein to various radio frequencies in a strong magnetic field, which can be analyzed to identify nearby atoms in the structure. This is then used to infer the three-dimensional structure. The drawbacks of NMR spectroscopy are that it is generally limited to only small proteins, cannot be used for insoluble proteins such as membrane proteins, and has low spatial resolution. Recently, another method called Cryo-electron microscopy (Cryo-EM) has improved in resolution to the point where it can be used for atomic-level structure solving. Cryo-EM has promise to alleviate several of the difficulties facing crystallography, since it freezes molecules rather than crystalizing them, but the method is still under development [46]. Overall, all three methods are limited to various degrees by expense and throughput capacity, and because of this only a fraction of known protein sequences have been structurally characterized. This has motivated the development of a wide array of computational structure prediction methods.

Computational methods

Computational methods for predicting protein tertiary structure can generally be divided into two categories: *ab initio* and template-based [47]. *Ab initio* (or *de novo*) methods attempt to determine a protein's structure directly from the sequence using first-principles molecular dynamics simulations. However, due to the enormous search space of possible three-dimensional conformations for an average-sized protein, *ab initio* methods are generally only computationally feasible for the smallest proteins [48]. Therefore, template-based modeling has been the more popular method over the last two decades.

Template-based modeling covers a wide variety of methods that make use of currently known information about protein structures—e.g. experimentally solved protein structures in the Protein Data Bank (PDB) [49]—as a starting point (or "template") for predicting the structures of new proteins. Template-based modeling can be subdivided into two main types: homology modeling and threading. Homology modeling, also called comparative modeling, uses sequence alignment methods to match a query sequence to any homologous sequences within the database of structurally-solved proteins. These methods work on the assumption that homologous proteins are likely to share a conserved structure, and therefore the structure of the homolog can be used to predict the structure of the query. Homology modeling methods such as HHPred [50]—which uses hidden Markov model (HMM)-based profile-profile alignments to increase sensitivity—have demonstrated good results when a homolog can be detected. However, the major challenge facing these methods is the difficulty of detecting more remote homologs—those falling within the "twilight zone" of sequence similarity, usually <30% identity [51]. This includes a large fraction of proteins at the current time, and has thus motivated the second template-based method—threading. Threading or "fold recognition" methods do not require homology or sequence similarity with a structurally solved protein in order to work, but instead try to directly use structural information to find the best match for the query. Briefly, threading comprises aligning a query sequence to a structural "template", defined in this context as the three-dimensional coordinates of atoms derived from a known protein structure (usually with the side chains removed). The best alignment between the query and structure is determined based on the compatibility of residue contacts, secondary structures, solvent access, and other criteria. This process is then repeated for every template in the database to identify which structure gives the most thermodynamically favorable structure for that sequence. Although threading has the advantage of working even in the absence of homology between the query and template, it is limited by much greater computational costs than homology modeling. Nonetheless, threading is much more tractable than *ab initio* methods, and thus has been used extensively and to good success over the last several years [51].

More recently, a third category of methods has emerged that combines aspects of *ab initio* and template-based methods [47]. These hybrid methods usually cut the protein sequence into many smaller fragments, and then attempt to match each fragment to one or more templates (which themselves are fragments of known structures). Once template candidates have been identified, *ab initio* methods are used to assemble the fragments into a conformation that is energetically favorable for the protein as a whole. Using the templates as a starting point greatly limits the search space, making the *ab initio* simulations more tractable. I-TASSER [52] and Rosetta [53] are two examples of highly successful hybrid methods. However, these methods are still too slow to be applied to large scale projects, such as whole-proteome structure prediction.

1.2.3. Structure-function relationships

There is a strong association between structure and function among proteins. Proteins with similar structure very often have similar function [54], and—to a lesser extent—proteins with similar function may have similar structure. This has been shown to hold true even for highly disparate amino acid sequences, and is the main motivation behind the field of structural genomics, which makes extensive use of the experimental and computation methods described above to make inferences about function based on structural similarities between proteins on a genome scale [55].

There are limits to the amount of functional information that can be gained simply by matching proteins to similar tertiary structures. For one thing, since structure prediction is usually done on the level of individual domains, this information must be integrated to understand the overall function of multi-domain proteins. Secondly, many of the nuances of domain function are influenced by fine-grained differences in the arrangement of secondary structures or by variation of specific residues in a binding pocket or enzymatic active site. This is particularly evident in the case of “superfolds”; for example, the TIM barrel fold is primarily found in enzymes, but consists of at least 60 distinct enzyme commission (EC) classes [44]. Finally, a large fraction of proteins include “intrinsically disordered” regions that do not take on a well-defined native tertiary structure. These regions often serve as flexible linkers between domains in multi-domain proteins, or may only fold when bound by a cofactor [47,56]. The function of these regions is therefore not amenable to typical structure-based analysis.

Despite these limitations, structure prediction has proved to be an extremely useful first step towards a functional understanding of uncharacterized proteins [54]. Improving the speed of methods for recognizing structural similarities, especially in the absence of sequence similarity, will greatly increase our capability for genome-scale annotation of protein function. A new approach to this problem will be discussed in Chapter 3.

1.3. Neurons, plasticity, and structure

Neurons are highly polarized cells consisting of a cell body (soma), and long, branched processes (usually a single axon and multiple dendrites). The flow of information through the neuron typically proceeds from the dendrites, which receive signals from other neurons at synapses; to the soma, which integrates signals; and finally to the axon, which transmits signals to other neurons. Synapses show a remarkable ability to remodel themselves in response to stimulation, becoming more or less responsive to future inputs (synaptic plasticity). This is thought to be one of the mechanisms underlying the larger scale phenomena of learning and memory in the brain. Here, I will survey important concepts related to synaptic plasticity in pyramidal neurons of the CA1 hippocampus, which have been studied extensively in this context, and highlight areas where structure analysis can help further our understanding.

1.3.1. Components of pyramidal neurons

Pyramidal neurons exist in a wide variety of mammals and are generally found in brain structures associated with complex cognitive function [57,58]. The morphology of pyramidal neurons is characterized by a single axon with many branches that make excitatory glutamatergic synapses with other neurons, as well as an extensive dendritic arbor with mostly excitatory synaptic inputs [58]. Pyramidal neurons may also receive some synaptic inputs on the axon and soma, which are typically inhibitory GABAergic synapses [58].

An important set of substructures of pyramidal dendrites are the dendritic spines—small, knob-like protrusions along the dendrites which are the site of most glutamatergic synapses. Spines vary widely in size and shape [59] and show morphological and functional plasticity over time [60–62]. A single pyramidal neuron may have thousands of dendritic spines, occurring at a density of about 1-10 spines per μm of dendritic length in mature neurons [59]. Although the precise purpose of spines is unclear, one of their main functions is likely to compartmentalize synapses and help prevent important molecules from diffusing away [63,64]. The spine neck may also serve to modulate electrical conductance properties [65]. Abnormal spine morphology has been observed in many neurological disorders, including Down Syndrome [66], Fragile X Syndrome [67], and epilepsy [68].

Dendrites also contain a variety of organelles, including abundant mitochondria [69], endoplasmic reticulum (ER) [70–73], Golgi “outposts” [70], and multivesicular bodies [71,73]. An organelle called the “spine apparatus” has also been observed in dendrites [74,75], which appears in 10-15% of mature hippocampal spines [71]; however, the exact function of this organelle is not currently well understood. In addition to organelles, many components of the translational machinery have been found in dendrites at the base of spines, including tRNAs, polyribosomes, and initiation/elongation factors [76–78].

1.3.2. Long-term potentiation

The idea that the plasticity of synapses could play a central role in learning and memory was suggested over a century ago by Santiago Ramón y Cajal [79]. In 1949, Donald Hebb formalized a model of how synaptic plasticity relates to learning and memory [80], but it was not until about 20 years later that substantial evidence for a molecular basis of such a model was provided by the discovery of long-term potentiation (LTP) [81,82]. These studies showed that stimulating excitatory hippocampal synapses resulted in a long-lasting increase in synaptic strength of those synapses. Since then, LTP has become an area of intense research in the field of neuroscience, and remains one of the leading hypotheses of the molecular basis of learning and memory [83,84]. Although there are now thought to be multiple forms of LTP, which depend on factors such as brain region and stimulation frequency [84], I will focus here on N-methyl-D-aspartate (NMDA) receptor-dependent LTP that occurs in the CA1 region of the hippocampus.

LTP is often described as having two stages: an early phase (E-LTP), usually defined as the first 1-3 hours after stimulation; and a late phase (L-LTP), which requires protein synthesis and gene transcription [85]. E-LTP is triggered by activation of post-synaptic NMDA receptors (NMDARs), which open to allow calcium influx [84]. This activates Ca^{2+}/calmodulin-dependent protein kinase (CaMKII) [86], which causes a rapid increase in α-Amino-3-hydroxy-5-methyl-4-isoxazoleprpionic acid receptors (AMPARs) in the synapse membrane [87]. The exact mechanism by which CaMKII influences AMPAR synaptic trafficking is currently unclear. Several early studies suggested that CaMKII phosphorylates the carboxy-terminal tail (C-tail) of AMPAR subunit GluA1 and/or AMPAR-accessory proteins [84]. In contrast, a recent set of studies has suggested that the C-tail of GluA1 is not needed for normal LTP, and furthermore, AMPARs can be completely replaced with kainite receptors without a substantial impact on LTP [84,88]. There is also conflicting evidence about which other signaling cascades, besides that mediated by CaMKII, might be important for LTP. Many molecules have been discovered that seem to modulate LTP, but few besides CaMKII have been shown to be vital [83]. These results show that despite substantial progress over the past 20 years, there is still much that is not well understood about this process.

The second phase, L-LTP, is dependent on new protein translation. Furthermore, this new translation often occurs in the dendrites themselves, in close proximity to the activated synapse [89]. There is now substantial evidence that a subset of neuronal mRNAs are actively localized to the dendrites, usually in a translationally repressed state, and then translated locally in or near spines in response to synaptic activation. The topics of mRNA localization and local translation are discussed in more detail in the next two sections. It is worth noting that there is also evidence for an important role of new transcription for L-LTP [90], which will not be reviewed extensively here.

Beyond changing the molecular composition of the synapse, LTP also causes (and possibly is perpetuated by) changes in the shape and size of the spine in which the synapse is housed [69]. The mechanisms of how this occurs are still being investigated, but filamentous actin (F-actin) polymerization dynamics likely play an important role [69,84]. F-actin makes up one of the major structural components of spines, and inhibition of actin polymerization prevents spine growth and LTP [91,92]. Activity-dependent cytoskeletal growth may be due to CaMKII activation of Rho GTPases, which promote actin polymerization, although how this occurs is not known [84]. It is hypothesized that these changes in structure may help promote AMPAR incorporation into the synapse, and thus promotes LTP [84]. After increasing in size, the spine can be further stabilized by cell adhesion molecules, such as N-cadherin, which has been shown to increase after synaptic activity [69].

1.3.3. Importance of RNA localization and local translation

Direct evidence for the idea that new protein synthesis was required for memory formation was first demonstrated in the 1960s, where it was shown that mice injected with the protein synthesis inhibitor puromycin to the temporal lobe showed impaired long-term memory formation if the injection was given within three days [93]. A large number of follow-up studies corroborated the potential importance of new protein synthesis in a variety of memory-related behaviors [94]. On the molecular level, treatment with the protein synthesis inhibitor anisomycin was shown to inhibit spine enlargement during LTP [95], lending further support that LTP might form the molecular basis of learning and memory. However, these studies at first did not directly address the question of where within the neuron this new protein synthesis was occurring, and it was generally assumed that it would occur in the soma [85].

Following the discovery of polyribosomes [76] and multiple mRNAs [96–98] in the dendrites, the idea that translation could occur locally in the dendrites began to gain popularity. This model was attractive for several reasons. For one, it provided a simple mechanism by which newly synthesized proteins could be sorted to the correct synapse: synaptic activation could trigger translation of only those mRNAs in the vicinity of the spine, thus causing a local increase in new proteins at the activated synapse. Other theoretical benefits include reduced transport costs, faster response time, and prevention of toxic ectopic protein expression [99,100]. Finally, in 1996, two studies provided direct evidence that protein synthesis can in fact occur locally in isolated dendrites [101] and hippocampal tissue slices [102].

Although local translation is now generally accepted as being important for lasting synaptic potentiation [103], there is less known about exactly which mRNAs are localized and what roles individual locally-translated proteins play in LTP. As techniques for profiling and quantifying RNA have improved, estimates of the dendritic transcriptome have expanded from a few RNAs [98] to a few hundred [104–107] to possibly even a few thousand [108,109]. There are several RNAs that are considered "gold standard" localized RNAs, which have been observed by multiple labs and methods to be robustly localized to the dendrites, such as CaMKIIα, β-actin, Arc, and BC1. But overall, there has been surprisingly little concordance between different analyses of the dendritic transcriptome, even when the same organism and brain region are profiled. In terms of understanding the actual functional role of individual localized mRNAs and their protein products, even more work remains to be done. To show specifically that local translation of a particular protein is important for LTP, an ideal experiment would disrupt only the local translation of that protein without altering its somatic expression. So far, this has mostly been accomplished in a few isolated cases, usually by abolishing the dendritic localization of the mRNA. For example, in mice lacking the 3'UTR of CaMKIIα mRNA, which contains its dendritic targeting sequence, it was shown that protein levels of CaMKII at the synapse were greatly reduced and L-LTP was impaired [110]. Much more work remains to be done to understand the role of the many potential locally-translated proteins in LTP.

1.3.4. Mechanisms of dendritic RNA localization: a role for structures

Proper localization of RNAs to the dendrites is a prerequisite for local translation, and therefore for long-lasting synaptic potentiation. Dendritic localization is thought to be mediated by specific RNA-binding proteins (RBPs) that recognize sequence or structure motifs on their target RNAs [100,111,112]. These RBPs may recruit other proteins to the RNA, forming a ribonucleoprotein complex (RNP). The RNP typically includes proteins that interact with motor proteins such as kinesin and dynein [113–115], which move along microtubules in the soma and dendrites to bring the RNP to its destination. While in the dendrites, RNA is mostly kept in a translationally repressed state by proteins in the RNP [115–117]. This repression is then relieved when a nearby synapse is activated, allowing for local production of proteins [117,118].

Interactions between RBPs and RNAs are vital for proper localization, and much work has been done to try to identify the dendritic targeting elements (DTEs) on localized RNAs that are recognized by RBPs. Identifying these DTEs would have benefits such as (1) allowing us to predict additional localized RNAs based on the presence of similar motifs, (2) enabling the identification of co-regulated groups of RNAs based on the presence of shared DTEs, and (3) providing insights into how dysregulation of RBP binding and RNA localization can lead to disease. Thus far, however, the identification of DTEs has been challenging. Below I briefly outline what is known about the localization and DTEs of a few of the most well-characterized dendritic RNAs and localization-mediating RBPs.

BC1 RNA. Brain cytoplasmic RNA 1 (BC1) is a short (~150nt), structured non-coding RNA that is dendritically localized [119] and plays a potential role in translational regulation [120]. The stem loop structure at its 5’ end has been experimentally determined [121] and is likely the DTE [122]. A particular part of the stem loop forms a GA kink-turn motif and seems to be bound by hnRNP-A2, which mediates the localization [123]. A type of short interspersed nuclear element (SINE) called the ID element is derived from BC1 [124] and has also been shown to act as a DTE in several dendritic RNAs in rat [125,126].

Staufen. The Staufen family of proteins (Stau1 and Stau2) are RBPs that bind dsRNA such as that found in stem-loop structures. Stau1 is ubiquitously expressed across tissues and may play a role in L-LTP [127]. Stau2 protein is enriched in the brain [100], shuttles to the dendrites in RNPs [128], and is likely involved in dendritic localization [28]. Several secondary structures have been proposed to be bound by Stau2 [129], which appear mostly sequence-independent.

ZBP1 and β-actin. A 54nt region in the 3'UTR of β-actin, known as the "zipcode" sequence, is necessary and sufficient for its localization in several cell types [130]. Binding of zipcode-binding protein 1 (ZBP1, called IMP-1 in human) to the zipcode was found to be important for both the localization and translational inhibition of β-actin [131,132]. Later studies showed that most of the zipcode actually functions as a spacer for two much shorter motifs that are bound by two KH domains of ZBP1, and that similar bipartite motifs were conserved in other mouse/human mRNAs, making them potential targets of ZBP1 as well [133].

FMRP. Fragile-X mental retardation protein (FMRP) is thought to play an important role in translational repression of localized mRNAs and possibly also modulates localization [116]. It appears to bind to a wide variety of localized RNAs, including CaMKIIα, Map1b, PSD-95, and Fmr1 (its own mRNA) [100]. It has been proposed to bind to G-quadruplexes through its RGG-box domain [134,135], although a more recent study of FMRP binding using HITS-CLIP showed no enrichment for G-quadruplexes or any other motif [136].

hnRNP-A2. Heterogeneous ribonucleoprotein particle A2 (hnRNP-A2) binds to known dendritically localized RNAs such as CaMKIIα and Arc [137] and is thought to be directly involved in localization. Multiple motifs have been proposed to be recognized by this RBP, including a pair of 11nt sequences (the hnRNP-A2 recognition element, A2RE) first identified in the MBP mRNA in oligodendrocytes [138], G-quadruplex structures and CGG repeats [139,140], and GA kink-turn structural motifs [123].

CaMKIIα. Although it is one of the most extensively studied dendritically localized mRNAs, CaMKIIα still does not have a fully defined DTE. Most reports point to an element in the 3'UTR, but there is conflicting evidence about the minimal element needed for localization [110,123,141–143]. Implicated regions so far include both linear sequences and secondary structures.

A common theme in many of these examples is the lack of consensus regarding the location and nature (linear or structural) of DTEs on specific transcripts. Part of the problem may be that some localized RNAs in fact have multiple DTEs, each regulating distinct and/or redundant aspects of the localization process [99]. An interesting example of this is BC1, which was shown to have two sub-motifs within its DTE: one that was needed for nuclear export and another that was needed for transport to the distal dendrites [123]. Adding to this difficulty, many DTEs are now known to have a secondary structure component that is either central to or supports recognition by the RBP [144], which may have contributed to conflicting reports in the past that mostly focused on linear sequence DTEs. Given that there are hundreds or even thousands of localized RNAs in neurons, it seems unlikely that each one has a unique DTE and RBP mediating its localization. A more likely explanation is that multiple localized RNAs share DTEs and are recognized by the same RBP, but we are missing these signals due to a lack of tools that perform *de novo* RNA structure motif discovery in large datasets.

1.3.5. Protein structures of the synapse

One of the gaps in our understanding of long-lasting synaptic potentiation is the specific role of each locally-translated protein in this process. Although experimental work will be needed to pick apart exact functions, we can make some initial guesses using computational annotation methods. Structure-based functional annotation may be of particular use in this case, given that there are a variety of important roles for protein structures at the synapse. Examples include the PDZ domain in scaffold-associated proteins [145]; cadherins, neurexins/neuroligins, ephBs/ephrin-B, and immunoglobulin-containing cell adhesion folds at the synaptic junction [146]; transmembrane folds in membrane-bound channels and receptors; kinase and phosphatase catalytic folds involved in signaling and synaptic plasticity; and many others. Although many of the proteins containing these structures are likely to be constitutively present at the spine or post-synaptic density (surveyed in [147–149]), and thus may be primarily synthesized in the soma, it would be interesting to see if a subpopulation of these proteins is locally translated as well, and if new examples of these folds can be discovered. Furthermore, recent genome-wide analyses of neurological diseases have revealed enrichment for causative mutations in synaptic proteins in human and mouse [147,149], several of which have been shown to disrupt important structural binding sites. A better understanding of the structures of locally translated proteins will help guide future experimental work and aid in predicting the functional impact of mutations.

1.4. Overview of thesis

In this thesis, I present two new methods for structure-based analysis of large-scale datasets based on the concept of empirical feature spaces—feature spaces defined by examples of natural structures—and then apply these methods to address the questions outlined above regarding the localization of RNA in the dendrites of neurons and the possible roles of locally translated proteins.

In Chapter 2, I describe the RNA empirical structure space (RESS), which uses Rfam covariance models to map uncharacterized RNAs to a structural feature space. I will show that RNAs with similar structure cluster together within the RESS, even in the absence of sequence similarity, and use this fact to develop a pipeline for *de novo* secondary structure motif discovery that can be applied to finding functional motifs enriched in co-regulated transcripts. Since this method scales linearly with increasing input dataset size, it is feasible to run on thousands of sequences at once.

In Chapter 3, I describe the protein empirical structure space (PESS), which uses threading against a small set of known structure templates to map uncharacterized protein domain sequences to structural feature space. As with the RESS, the PESS clusters protein sequences based on structure even in the absence of detectable sequence similarity. I show that the PESS can be used for a variety of purposes including classification of sequences into known folds, identification of novel folds, and finding of distant homologs (or structural analogs) across species. This method saves substantial amounts of time compared to traditional threading methods by using only a small library of templates for threading, yet has accuracy on par with threading against a much larger set.

In Chapter 4, I will combine experimental and computational methods, including the two methods described above, to catalog the set of RNAs localized to the dendrites in mouse hippocampal neurons, identify potential linear and structural localization signals, and predict the functions of locally translated proteins based on domain-level structural prediction. The results include findings that would be difficult to identify using traditional sequence-based tools, demonstrating the utility of including structure-based tools when performing functional analysis of RNA and protein.

Finally, in Chapter 5, I discuss some of the implications and future directions suggested by this work, including several avenues where structure analysis may yield particular insight.

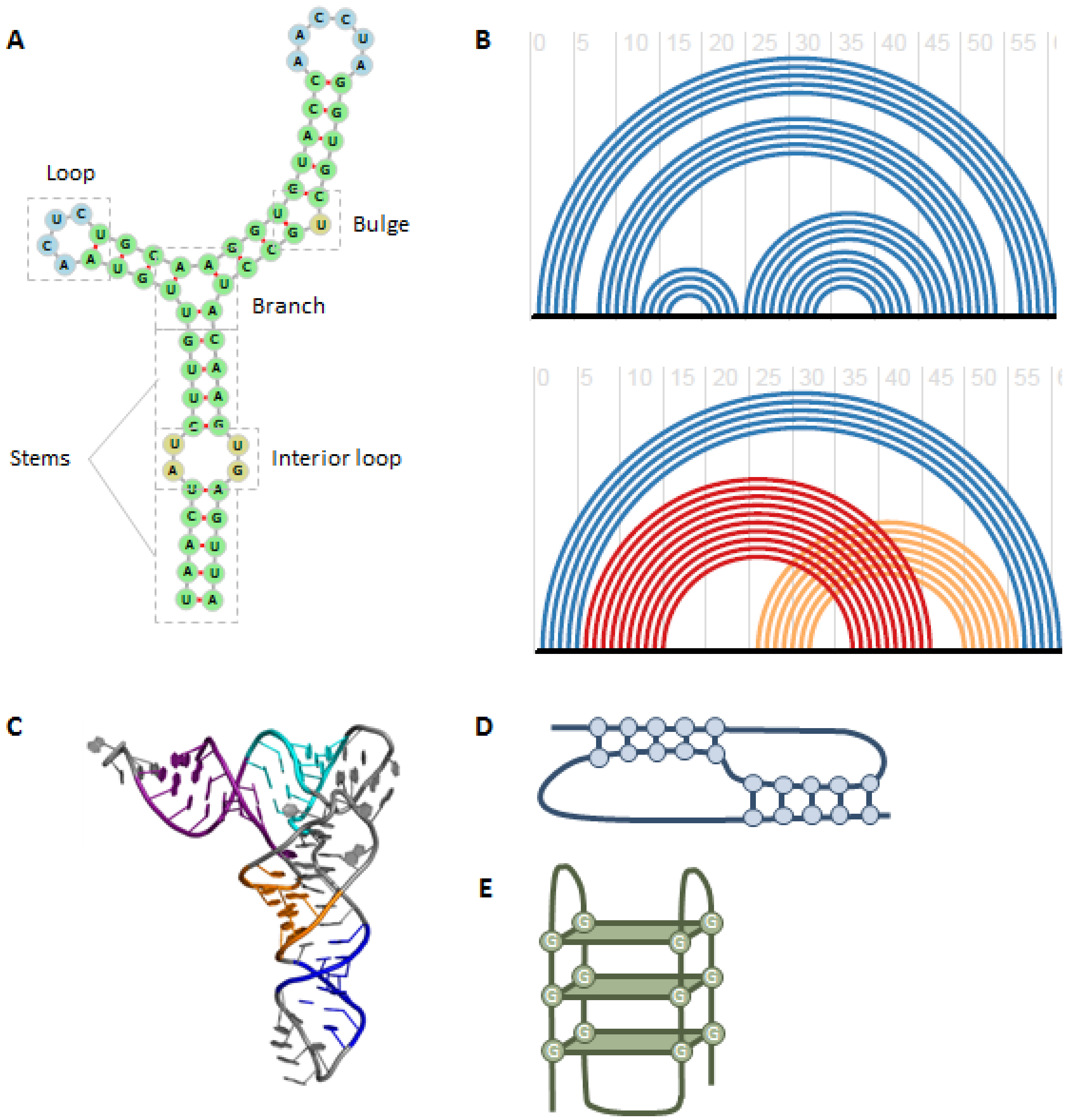

Figure 1-1. RNA structure.

(A) An example of RNA secondary structure, showing typical motifs. (B) A well nested structure (top) and non-nested structure (bottom). The black horizontal lines indicate an RNA sequence and the arches show base pairing. Red and orange arches highlight the non-nested part of the structure that crosses over itself. The top panel corresponds to the structure in (A). (C) An example of RNA tertiary structure. (Image from the public domain.) (D) An example of a pseudoknot structure, which consists of non-nested base pairing interactions. (E) An example of a G-quadruplex structure consisting of four repeating units of three G’s, separated by small loops.

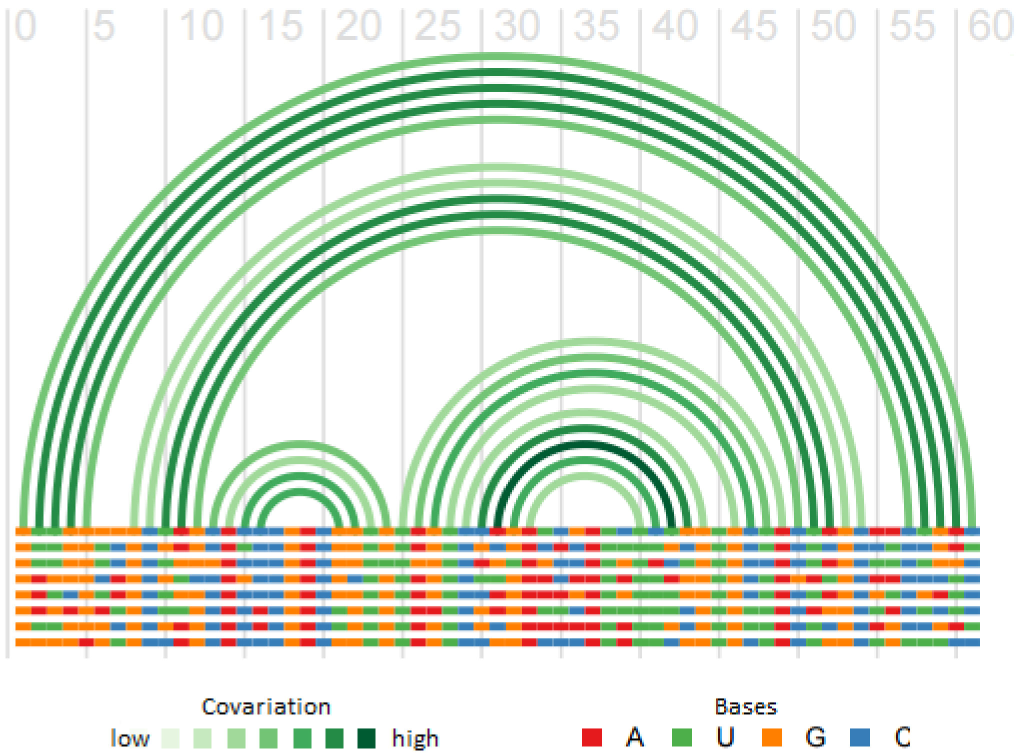

Figure 1-2. Covariation in a multiple alignment of RNA sequences.

Arches show base pairing interactions. Paired bases tend to show compensatory changes that maintain pairing, whereas non-paired bases usually show uncorrelated variation. Note that G-U pairs are generally considered compatible. Figure generated using R-chie [150].

1.5. References

1 Wan, Y. *et al.* (2011) Understanding the transcriptome through RNA structure. *Nat. Rev. Genet.* 12, 641–655

2 Geisler, S. and Coller, J. (2013) RNA in unexpected places: long non-coding RNA functions in diverse cellular contexts. *Nat. Rev. Mol. Cell Biol.* 14, 699–712

3 Varani, G. and McClain, W.H. (2000) The G-U wobble base pair. *EMBO Rep.* 1, 18–23

4 Butcher, S.E. and Pyle, A.M. (2011) The Molecular Interactions That Stabilize RNA Tertiary Structure: RNA Motifs, Patterns, and Networks. *Acc. Chem. Res.* 44, 1302–1311

5 Wilkinson, K.A. *et al.* (2006) Selective 2′-hydroxyl acylation analyzed by primer extension (SHAPE): quantitative RNA structure analysis at single nucleotide resolution. *Nat. Protoc.* 1, 1610–1616

6 Kubota, M. *et al.* (2015) Progress and challenges for chemical probing of RNA structure inside living cells. *Nat. Chem. Biol.* 11, 933–941

7 Lu, Z. and Chang, H.Y. (2016) Decoding the RNA structurome. *Curr. Opin. Struct. Biol.* 36, 142–148

8 Zuker, M. and Stiegler, P. (1981) Optimal computer folding of large RNA sequences using thermodynamics and auxiliary information. *Nucleic Acids Res.* 9, 133–148

9 Zuker, M. (1989) On finding all suboptimal foldings of an RNA molecule. *Science* 244, 48–52

10 Zuker, M. (2003) Mfold web server for nucleic acid folding and hybridization prediction. *Nucleic Acids Res.* 31, 3406–3415

11 Hofacker, I.L. (2003) Vienna RNA secondary structure server. *Nucleic Acids Res.* 31, 3429–3431

12 Hofacker, I.L. *et al.* (1994) Fast folding and comparison of RNA secondary structures. *Monatshefte fur Chemie Chem. Mon.* 125, 167–188

13 Eddy, S.R. and Durbin, R. (1994) RNA sequence analysis using covariance models. *Nucleic Acids Res.* 22, 2079–2088

14 Hofacker, I.L. *et al.* (2002) Secondary Structure Prediction for Aligned RNA Sequences. *J. Mol. Biol.* 319, 1059–1066

15 Washietl, S. *et al.* (2005) Fast and reliable prediction of noncoding RNAs. *Proc. Natl. Acad. Sci.* 102, 2454–2459

16 Griffiths-Jones, S. (2003) Rfam: an RNA family database. *Nucleic Acids Res.* 31, 439–441

17 Yao, Z. *et al.* (2006) CMfinder--a covariance model based RNA motif finding algorithm. *Bioinformatics* 22, 445–52

18 Torarinsson, E. *et al.* (2007) Multiple structural alignment and clustering of RNA sequences. *Bioinformatics* 23, 926–32

19 Mathews, D.H. and Turner, D.H. (2002) Dynalign: an algorithm for finding the secondary structure common to two RNA sequences. *J. Mol. Biol.* 317, 191–203

20 Will, S. *et al.* (2007) Inferring noncoding RNA families and classes by means of genome-scale structure-based clustering. *PLoS Comput. Biol.* 3, e65

21 Sankoff, D. (1985) Simultaneous solution of the RNA folding, alignment and protosequence problems. *SIAM J. Appl. Math.* 45, 810–825

22 Shatsky, I.N. *et al.* (2010) Cap- and IRES-independent scanning mechanism of translation initiation as an alternative to the concept of cellular IRESs. *Mol. Cells* 30, 285–93

23 Wellensiek, B.P. *et al.* (2013) Genome-wide profiling of human cap-independent translation-enhancing elements. *Nat. Methods* 10, 747–50

24 Weingarten-Gabbay, S. *et al.* (2016) Systematic discovery of cap-independent translation sequences in human and viral genomes. *Science (80-.).* 351, aad4939-aad4939

25 Tian, B. and Manley, J.L. (2016) Alternative polyadenylation of mRNA precursors. *Nat. Rev. Mol. Cell Biol.* DOI: 10.1038/nrm.2016.116

26 Heraud-Farlow, J.E. and Kiebler, M.A. (2014) The multifunctional Staufen proteins: conserved roles from neurogenesis to synaptic plasticity. *Trends Neurosci.* 37, 470–479

27 Li, X. *et al.* (2014) Finding the target sites of RNA-binding proteins. *Wiley Interdiscip. Rev. RNA* 5, 111–130

28 Tang, S.J. *et al.* (2001) A role for a rat homolog of staufen in the transport of RNA

to neuronal dendrites. *Neuron* 32, 463–475

29 Heraud-Farlow, J.E. *et al.* (2013) Staufen2 regulates neuronal target RNAs. *Cell Rep.* 5, 1511–1518

30 Savva, Y.A. *et al.* (2012) The ADAR protein family. *Genome Biol.* 13, 252

31 Au, H.H.T. and Jan, E. (2012) Insights into Factorless Translational Initiation by the tRNA-Like Pseudoknot Domain of a Viral IRES. *PLoS One* 7, e51477

32 Kanamori, Y. and Nakashima, N. (2001) A tertiary structure model of the internal ribosome entry site (IRES) for methionine-independent initiation of translation. *RNA* 7, 266–274

33 Cech, T.R. and Steitz, J.A. (2014) The Noncoding RNA Revolution—Trashing Old Rules to Forge New Ones. *Cell* 157, 77–94

34 Mercer, T.R. and Mattick, J.S. (2013) Structure and function of long noncoding RNAs in epigenetic regulation. *Nat. Struct. Mol. Biol.* 20, 300–307

35 Nawrocki, E.P. *et al.* (2014) Rfam 12.0: updates to the RNA families database. *Nucleic Acids Res.* 43, 130–137

36 Ha, M. and Kim, V.N. (2014) Regulation of microRNA biogenesis. *Nat. Rev. Mol. Cell Biol.* 15, 509–524

37 Khan, S. and Vihinen, M. (2007) Spectrum of disease-causing mutations in protein secondary structures. *BMC Struct. Biol.* 7, 56

38 Pauling, L. *et al.* (1951) The structure of proteins; two hydrogen-bonded helical configurations of the polypeptide chain. *Proc. Natl. Acad. Sci. U. S. A.* 37, 205–211

39 Pauling, L. and Corey, R.B. (1951) The pleated sheet, a new layer configuration of polypeptide chains. *Proc. Natl. Acad. Sci. U. S. A.* 37, 521–526

40 Koonin, E. V *et al.* (2002) The structure of the protein universe and genome evolution. *Nature* 420, 218–223

41 Finn, R.D. *et al.* (2016) The Pfam protein families database: towards a more sustainable future. *Nucleic Acids Res.* 44, D279–D285

42 Illergård, K. *et al.* (2009) Structure is three to ten times more conserved than sequence-A study of structural response in protein cores. *Proteins Struct. Funct. Bioinforma.* 77, 499–508

43 Fox, N.K. *et al.* (2014) SCOPe: Structural Classification of Proteins—extended, integrating SCOP and ASTRAL data and classification of new structures. *Nucleic Acids Res.* 42, D304–D309

44 Lee, D. *et al.* (2007) Predicting protein function from sequence and structure. *Nat. Rev. Mol. Cell Biol.* 8, 995–1005

45 Sillitoe, I. *et al.* (2015) CATH: comprehensive structural and functional annotations for genome sequences. *Nucleic Acids Res.* 43, D376–D381

46 Callaway, E. (2015) The Revolution Will Not Be Crystallized. *Nature* 525, 172–174

47 Dorn, M. *et al.* (2014) Three-dimensional protein structure prediction: Methods and computational strategies. *Comput. Biol. Chem.* 53, 251–276

48 Dill, K.A. and MacCallum, J.L. (2012) The Protein-Folding Problem, 50 Years On. *Science (80-.).* 338, 1042–1046

49 Berman, H.M. (2000) The Protein Data Bank. *Nucleic Acids Res.* 28, 235–242

50 Soding, J. *et al.* (2005) The HHpred interactive server for protein homology detection and structure prediction. *Nucleic Acids Res.* 33, W244–W248

51 Khor, B.Y. *et al.* (2015) General overview on structure prediction of twilight-zone proteins. *Theor. Biol. Med. Model.* 12, 15

52 Roy, A. *et al.* (2010) I-TASSER: a unified platform for automated protein structure and function prediction. *Nat. Protoc.* 5, 725–38

53 Raman, S. *et al.* (2009) Structure prediction for CASP8 with all-atom refinement using Rosetta. *Proteins Struct. Funct. Bioinforma.* 77, 89–99

54 Shin, D.H. *et al.* (2007) Structure-based inference of molecular functions of proteins of unknown function from Berkeley Structural Genomics Center. *J. Struct. Funct. Genomics* 8, 99–105

55 Zhang, C. and Kim, S.H. (2003) Overview of structural genomics: From structure to function. *Curr. Opin. Chem. Biol.* 7, 28–32

56 Dyson, H.J. and Wright, P.E. (2005) Intrinsically unstructured proteins and their functions. *Nat. Rev. Mol. Cell Biol.* 6, 197–208

57 Elston, G.N. (2003) Cortex, Cognition and the Cell: New Insights into the Pyramidal Neuron and Prefrontal Function. *Cereb. Cortex* 13, 1124–1138

58 Spruston, N. (2008) Pyramidal neurons: dendritic structure and synaptic integration. *Nat. Rev. Neurosci.* 9, 206–221

59 Sorra, K.E. and Harris, K.M. (2000) Overview on the structure, composition, function, development, and plasticity of hippocampal dendritic spines. *Hippocampus* 10, 501–511

60 Hering, H. and Sheng, M. (2001) Dendritic spines: structure, dynamics and regulation. *Nat. Rev. Neurosci.* 2, 880–888

61 Holtmaat, A.J.G.D. *et al.* (2005) Transient and persistent dendritic spines in the neocortex in vivo. *Neuron* 45, 279–291

62 Holtmaat, A. and Svoboda, K. (2009) Experience-dependent structural synaptic plasticity in the mammalian brain. *Nat. Rev. Neurosci.* 10, 759–759

63 Nimchinsky, E.A. *et al.* (2001) Structure and function of dendritic spines. *Annu. Rev. Physiol.* 64, 313–353

64 Koch, C. and Zador, A. (1993) The Function of Dendritic Spines: Devices Subserving Biochemical Rather Than Electrical Compartmentalization. *J. Neurosci.* 13, 413–422

65 Tsay, D. and Yuste, R. (2004) On the electrical function of dendritic spines. *Trends Neurosci.* 27, 77–83

66 Haas, M. a *et al.* (2013) Alterations to Dendritic Spine Morphology, but Not Dendrite Patterning, of Cortical Projection Neurons in Tc1 and Ts1Rhr Mouse Models of Down Syndrome. *PLoS One* 8, e78561

67 Irwin, S.A. *et al.* (2001) Abnormal dendritic spine characteristics in the temporal and visual cortices of patients with fragile-X syndrome: A quantitative examination. *Am. J. Med. Genet.* 98, 161–167

68 Swann, J.W. *et al.* (2000) Spine loss and other dendritic abnormalities in epilepsy. *Hippocampus* 10, 617–625

69 Bourne, J.N. and Harris, K.M. (2008) Balancing Structure and Function at Hippocampal Dendritic Spines. *Annu. Rev. Neurosci.* 31, 47–67

70 Horton, A.C. and Ehlers, M.D. (2004) Secretory trafficking in neuronal dendrites. *Nat. Cell Biol.* 6, 585–91

71 Spacek, J. and Harris, K.M. (1997) Three-Dimensional Organization of Smooth Endoplasmic Reticulum in Hippocampal CA1 Dendrites and Dendritic Spines of the Immature and Mature Rat. *J. Neurosci.* 17, 190–203

72 Steward, O. and Reeves, T.M. (1988) Protein-synthetic machinery beneath postsynaptic sites on CNS neurons: association between polyribosomes and other organelles at the synaptic site. *J. Neurosci.* 8, 176–84

73 Cooney, J.R. *et al.* (2002) Endosomal compartments serve multiple hippocampal dendritic spines from a widespread rather than a local store of recycling membrane. *J. Neurosci.* 22, 2215–2224

74 Gray, E.G. (1959) Axo-somatic and Axo-Dendritic Synapses of the Cerebral Cortex: an Electron Microscope Study. *J. Anat.* 93, 420–433

75 Segal, M. *et al.* (2010) The Spine Apparatus, Synaptopodin, and Dendritic Spine Plasticity. *Neurosci.* 16, 125–131

76 Steward, O. and Levy, W.B. (1982) Preferential localization of polyribosomes under the base of dendritic spines in granule cells of the dentate gyrus. *J. Neurosci.* 2, 284–291

77 Tiedge, H. and Brosius, J. (1996) Translational machinery in dendrites of hippocampal neurons in culture. *J. Neurosci.* 16, 7171–7181

78 Kiebler, M.A. and DesGroseillers, L. (2000) Molecular Insights into mRNA Transport and Local Translation in the Mammalian Nervous System. *Neuron* 25, 19–28

79 Cajal, S.R. y (1911) *Histologie du systeme nerveux de l'homme et des vertebres, transl. N Swanson, LWSwanson*, Oxford University Press.

80 Hebb, D.O. (1949) *The organization of behavior: A neuropsychological theory*, John Wiley and Sons, Inc.

81 Lømo, T. (1966) Frequency potentiation of excitatory synaptic activity in the dentate area of the hippocampal formation. *Acta Physiol. Scand.* 68, 128

82 Bliss, T. V and Lømo, T. (1973) Long-lasting potentiation of synaptic transmission in the dentate area of the unanaestetized rabbit following stimulation of the perforant path. *J. Physiol.* 232, 331–356

83 Malenka, R.C. (2003) Opinion: The long-term potential of LTP. *Nat. Rev. Neurosci.* 4, 923–926

84 Herring, B.E. and Nicoll, R.A. (2016) Long-Term Potentiation: From CaMKII to AMPA receptor trafficking. *Annu. Rev. Physiol.* 78, 351–65

85 Sutton, M.A. and Schuman, E.M. (2006) Dendritic protein synthesis, synaptic plasticity, and memory. *Cell* 127, 49–58

86 Lisman, J. *et al.* (2012) Mechanisms of CaMKII action in long-term potentiation. *Nat. Rev. Neurosci.* 257, 2432–2437

87 Patterson, M.A. *et al.* (2010) AMPA receptors are exocytosed in stimulated spines and adjacent dendrites in a Ras-ERK-dependent manner during long-term potentiation. *Proc. Natl. Acad. Sci. U. S. A.* 107, 15951–6

88 Granger, A.J. *et al.* (2012) LTP requires a reserve pool of glutamate receptors independent of subunit type. *Nature* 493, 495–500

89 Buxbaum, A.R. *et al.* (2014) In the right place at the right time: visualizing and understanding mRNA localization. *Nat. Rev. Mol. Cell Biol.* 16, 95–109

90 Nguyen, P. *et al.* (1994) Requirement of a critical period of transcription for induction of a late phase of LTP. *Science (80-.).* 265, 1104–1107

91 Kim, C.H. and Lisman, J.E. (1999) A role of actin filament in synaptic transmission and long-term potentiation. *J. Neurosci.* 19, 4314–4324

92 Huber, L. and Menzel, R. (2004) Structural basis of long-trm potentiation in single dendritic spines. *Nature* 429, 761–766

93 Flexner, J. *et al.* (1963) Memory in mice as affected by intracerebral puromycin. *Science (80-.).* 141, 57–59

94 Davis, H.P. and Squire, L.R. (1984) Protein synthesis and memory: a review. *Psychol. Bull.* 96, 518–59

95 Fifková, E. *et al.* (1982) Effect of anisomycin on stimulation-induced changes in dendritic spines of the dentate granule cells. *J. Neurocytol.* 11, 183

96 Davis, L. *et al.* (1987) Selective dendritic transport of RNA in hippocampal neurons in culture. *Nature* 330, 477–479

97 Garner, C. *et al.* (1988) Selective localization of messenger RNA for cytoskeletal protein MAP2 in dendrites. *Nature* 336,

98 Miyashiro, K. *et al.* (1994) On the nature and differential distribution of mRNAs in hippocampal neurites: implications for neuronal functioning. *Proc. Natl. Acad. Sci. U. S. A.* 91, 10800–4

99 Medioni, C. *et al.* (2012) Principles and roles of mRNA localization in animal development. *Development* 139, 3263–3276

100 Doyle, M. and Kiebler, M.A. (2011) Mechanisms of dendritic mRNA transport and its role in synaptic tagging. *EMBO J.* 30, 3540–3552

101 Crino, P.B. and Eberwine, J. (1996) Molecular characterization of the dendritic growth cone: regulated mRNA transport and local protein synthesis. *Neuron* 17, 1173–87

102 Kang, H. and Schuman, E.M. (1996) A requirement for local protein synthesis in neurotrophin-induced hippocampal synaptic plasticity. *Science* 273, 1402–6

103 Martin, K.C. *et al.* (2000) Local protein synthesis and its role in synapse-specific plasticity. *Curr. Opin. Neurobiol.* 10, 587–592

104 Eberwine, J. *et al.* (2001) Local translation of classes of mRNAs that are targeted to neuronal dendrites. *Proc. Natl. Acad. Sci.* 98, 7080–7085

105 Moccia, R. *et al.* (2003) An unbiased cDNA library prepared from isolated Aplysia sensory neuron processes is enriched for cytoskeletal and translational mRNAs. *J. Neurosci.* 23, 9409–17

106 Poon, M.M. *et al.* (2006) Identification of process-localized mRNAs from cultured rodent hippocampal neurons. *J. Neurosci.* 26, 13390–9

107 Zhong, J. *et al.* (2006) Dendritic mRNAs encode diversified functionalities in hippocampal pyramidal neurons. *BMC Neurosci.* 7, 17

108 Ainsley, J.A. *et al.* (2014) Functionally diverse dendritic mRNAs rapidly associate with ribosomes following a novel experience. *Nat. Commun.* 5, 4510

109 Cajigas, I.J. *et al.* (2012) The local transcriptome in the synaptic neuropil revealed by deep sequencing and high-resolution imaging. *Neuron* 74, 453–66

110 Miller, S. *et al.* (2002) Disruption of Dendritic Translation of CaMKIIα Impairs Stabilization of Synaptic Plasticity and Memory Consolidation. *Neuron* 36, 507–519

111 Bramham, C.R. and Wells, D.G. (2007) Dendritic mRNA: transport, translation and function. *Nat. Rev. Neurosci.* 8, 776–789

112 Chabanon, H. *et al.* (2004) Zipcodes and postage stamps: mRNA localisation signals and their trans-acting binding proteins. *Brief. Funct. Genomic. Proteomic.* 3, 240–56

113 Kanai, Y. *et al.* (2004) Kinesin Transports RNA: Isolation and Characterization of an RNA-Transporting Granule. *Neuron* 43, 513–525

114 Dictenberg, J.B. *et al.* (2008) A Direct Role for FMRP in Activity-Dependent Dendritic mRNA Transport Links Filopodial-Spine Morphogenesis to Fragile X Syndrome. *Dev. Cell* 14, 926–939

115 Buxbaum, A.R. *et al.* (2015) Single-molecule insights into mRNA dynamics in neurons. *Trends Cell Biol.* 25, 468–475

116 Costa-Mattioli, M. *et al.* (2009) Translational control of long-lasting synaptic plasticity and memory. *Neuron* 61, 10–26

117 Fernandez-Moya, S.M. *et al.* (2014) Meet the players: local translation at the synapse. *Front. Mol. Neurosci.* 7, 1–6

118 Buxbaum, A.R. *et al.* (2014) Single β-actin mRNA detection in neurons reveals a mechanism for regulating its translatability. *Science* 343, 419–22

119 Tiedge, H. *et al.* (1991) Dendritic location of neural BC1 RNA. *Proc. Natl. Acad. Sci.* 88, 2093–2097

120 Wang, H. *et al.* (2005) Dendritic BC1 RNA in translational control mechanisms. *J. Cell Biol.* 171, 811–821

121 ROZHDESTVENSKY, T.S. *et al.* (2001) Neuronal BC1 RNA structure: Evolutionary conversion of a tRNA(Ala) domain into an extended stem-loop structure. *RNA* 7, S1355838201002485

122 Muslimov, I.A. *et al.* (1997) RNA transport in dendrites: a cis-acting targeting element is contained within neuronal BC1 RNA. *J. Neurosci.* 17, 4722–4733

123 Muslimov, I.A. *et al.* (2006) Spatial codes in dendritic BC1 RNA. *J. Cell Biol.* 175, 427–439

124 Kim, J. *et al.* (1994) Rodent BC1 RNA gene as a master gene for ID element amplification. *Proc. Natl. Acad. Sci. U. S. A.* 91, 3607–11

125 Buckley, P.T. *et al.* (2011) Cytoplasmic intron sequence-retaining transcripts can be dendritically targeted via ID element retrotransposons. *Neuron* 69, 877–84

126 Muslimov, I. a. *et al.* (2014) Interactions of noncanonical motifs with hnRNP A2 promote activity-dependent RNA transport in neurons. *J. Cell Biol.* 205, 493–510

127 Lebeau, G. *et al.* (2008) Staufen1 Regulation of Protein Synthesis-Dependent Long-Term Potentiation and Synaptic Function in Hippocampal Pyramidal Cells. *Mol. Cell. Biol.* 28, 2896–2907

128 Köhrmann, M. *et al.* (1999) Microtubule-dependent Recruitment of Staufen-Green Fluorescent Protein into Large RNA-containing Granules and Subsequent Dendritic Transport in Living Hippocampal Neurons. *Mol. Biol. Cell* 10, 2945–2953

129 Laver, J.D. *et al.* (2013) Genome-wide analysis of Staufen-associated mRNAs identifies secondary structures that confer target specificity. *Nucleic Acids Res.* DOI: 10.1093/nar/gkt702

130 Kislauskis, E.H. *et al.* (1994) Sequences responsible for intracellular localization of beta-actin messenger RNA also affect cell phenotype. *J. Cell Biol.* 127, 441–451

131 Ross, A.F. *et al.* (1997) Characterization of a beta-actin mRNA zipcode-binding protein. *Mol. Cell. Biol.* 17, 2158–2165

132 Hüttelmaier, S. *et al.* (2005) Spatial regulation of β-actin translation by Src-dependent phosphorylation of ZBP1. *Nature* 438, 512–515

133 Patel, V.L. *et al.* (2012) Spatial arrangement of an RNA zipcode identifies mRNAs under post-transcriptional control. *Genes Dev.* 26, 43–53

134 Darnell, J.C. *et al.* (2001) Fragile X mental retardation protein targets G quartet mRNAs important for neuronal function. *Cell* 107, 489–499

135 Schaeffer, C. *et al.* (2001) The fragile X mental retardation protein binds specifically to its mRNA via a purine quartet motif. *EMBO J.* 20, 4803–4813

136 Darnell, J.C. *et al.* (2011) FMRP stalls ribosomal translocation on mRNAs linked to synaptic function and autism. *Cell* 146, 247–61

137 Gao, Y. *et al.* (2008) Multiplexed Dendritic Targeting of Calcium Calmodulin-dependent Protein Kinase II, Neurogranin, and Activity-regulated Cytoskeleton-associated Protein RNAs by the A2 Pathway. *Mol. Biol. Cell* 19, 2311–2327

138 Ainger, K. *et al.* (1997) Transport and Localization Elements in Myelin Basic Protein mRNA. *J. Cell Biol.* 138, 1077–1087

139 Sofola, O.A. *et al.* (2007) RNA-Binding Proteins hnRNP A2/B1 and CUGBP1 Suppress Fragile X CGG Premutation Repeat-Induced Neurodegeneration in a Drosophila Model of FXTAS. *Neuron* 55, 565–571

140 Muslimov, I. a *et al.* (2011) Spatial code recognition in neuronal RNA targeting: role of RNA-hnRNP A2 interactions. *J. Cell Biol.* 194, 441–57

141 Mori, Y. *et al.* (2000) Two cis-acting elements in the 3’ untranslated region of alpha-CaMKII regulate its dendritic targeting. *Nat. Neurosci.* 3, 1079–1084

142 Blichenberg, A. *et al.* (2001) Identification of a cis -acting dendritic targeting element in the mRNA encoding the alpha subunit of Ca 2+ /calmodulin-dependent protein kinase II. *Eur. J. Neurosci.* 13, 1881–1888

143 Subramanian, M. *et al.* (2011) G-quadruplex RNA structure as a signal for neurite mRNA targeting. *EMBO Rep.* 12, 697–704

144 Martin, K.C. and Ephrussi, A. (2009) mRNA Localization: Gene Expression in the Spatial Dimension. *Cell* 136, 719–730

145 Zheng, C.-Y. *et al.* (2011) MAGUKs, Synaptic Development, and Synaptic Plasticity. *Neurosci.* 17, 493–512

146 Dalva, M.B. *et al.* (2007) Cell adhesion molecules: signalling functions at the synapse. *Nat. Rev. Neurosci.* 8, 206–220

147 Bayés, À. *et al.* (2011) Characterization of the proteome, diseases and evolution of the human postsynaptic density. *Nat. Neurosci.* 14, 19–21

148 Bayés, À. *et al.* (2012) Comparative Study of Human and Mouse Postsynaptic Proteomes Finds High Compositional Conservation and Abundance Differences for Key Synaptic Proteins. *PLoS One* 7,

149 Grant, S.G. (2012) Synaptopathies: diseases of the synaptome. *Curr. Opin. Neurobiol.* 22, 522–529

150 Lai, D. *et al.* (2012) R-CHIE: a web server and R package for visualizing RNA secondary structures. *Nucleic Acids Res.* 40, e95–e95

Chapter 2: An empirical structure space for functional motif analysis of RNA

> Middleton, S. A. & Kim, J. NoFold: RNA structure clustering without folding or alignment. *RNA* **20**, 1671–1683 (2014).

2.1 Introduction

RNA structures play an important role in the function and regulation of almost all known classes of RNA. In coding transcripts, conserved secondary structures have been found in the untranslated regions (UTRs) that operate in *cis* to regulate processes such as alternative splicing, translation, and subcellular localization (for review see [1]). Several of these *cis*-structures have been found to be motifs—modular elements that occur across multiple different transcripts and provide a similar function or regulatory signal. Examples include the selenocysteine insertion sequence [2], the iron response element [3], and some localization signals [4]. Structure motifs also play a well-documented role in non-coding RNA function, such as the cloverleaf structure of tRNAs and the long hairpin structure of pre-microRNAs. The Rfam database [5] has organized many of these known motifs into structure “families” and provides a covariance model (CM) [6] for each family, which can be used to quickly scan new sequences to infer instances of known motifs. However, the identification of novel motifs that are not already modeled by Rfam remains a challenging problem.

Existing algorithms for finding novel secondary structure motifs differ widely in their approaches, but almost all begin with some form of structure prediction. Structure prediction can be done for single sequences individually by maximizing thermodynamic stability, as in MFOLD [7,8] and RNAfold [9,10], or can be done using covariance information of stem nucleotide pairs from a multiple alignment. Although alignment-based methods generally result in more reliable predictions than thermodynamic stability alone, building a multiple alignment of RNAs can be difficult when the primary sequences are highly diverged. For most traditional sequence aligners, performance drops off dramatically when aligning families with less than 60% sequence identity [11]. Given that many highly conserved structure families have an average sequence identity lower than this threshold (e.g. the tRNA family with 46% sequence identity), such aligners are often not sufficient for identifying RNA structure families. To address this issue, methods such as FoldalignM [12], Dynalign [13], and LocARNA [14] attempt to align RNAs by both sequence and structure simultaneously, using approximations of the Sankoff align-and-fold algorithm [15]. While these methods generally perform better than traditional aligners on structural RNAs, they are computationally intensive and require time-saving heuristics when used to align a large number of sequences.

In order to identify structures that occur multiple times in a given dataset, an additional step of clustering is needed. The choice of distance metric and clustering algorithm depend largely on the method used for structure prediction. Individually predicted structures can be compared by computing a distance metric over the base pair probability matrices [16,17] or the dot-bracket structure representations [18]. A popular approach is to first reduce each individual structure to a tree representation, where stems and loops are reduced a graph-theoretic representation, before computing a tree alignment or edit-distance [9,19–22]. A recent algorithm in this vein is GraphClust [23], which uses the RNAshapes software [21] to sample several low-energy structures that are then encoded as graphs and compared using a graph kernel. Alternatively, instead of predicting each individual structure and then comparing pairs of structures, the structural similarity between two RNAs can be derived directly from their pairwise alignment using an align-and-fold algorithm. This is the strategy employed by RNAclust [14] and FoldalignM. Once a distance matrix has been created for the sequences of interest, common clustering methods can be employed to identify recurring structures. However, since these algorithms all use as their basis some form of folding or pairwise sequence alignment, they are limited by the tradeoff between speed and accuracy.

Here we describe a novel approach to RNA structure clustering which does not require folding or pairwise alignment of the input sequences. Our approach is inspired by the idea of an “empirical kernel”, where the distance between any two objects is computed within an observation-spanned subspace by comparing each object to a set of empirical examples or models [24]. Using Rfam CMs as our empirical models, we thus measure the structural distance between two RNA sequences based on their respective scores against each CM. In this way, we represent each input sequence as a superposition of known structures. Part of the motivation for this approach comes from known examples of such superposition in nature, such as the presence of tRNA-like motifs in transfer-messenger RNA (tmRNA) [25] and in some internal ribosome entry sites [26]. However, as we will show here, this approach can identify motifs even in the absence of trivial similarity between the motif and the reference models. Using this folding- and alignment-free distance measure as a basis, we developed a pipeline called NoFold for clustering and automatically extracting cohesive clusters, which can be used to find structure motifs in any set of RNA sequences. In a benchmark containing 20 Rfam structure families, we demonstrate that NoFold can simultaneously recapitulate almost all of the families with high sensitivity and precision and that this performance is robust to the presence of unrelated sequences within the dataset or extraneous flanking sequence on the structural sequences. Using NoFold, we identify 213 motifs that are enriched in the 3'UTRs and retained introns of dendritically localized transcripts, including a previously identified localization-mediating motif and several potentially novel structures with similarity to the *Drosophila* K10 localization element.

2.2 Results

2.2.1 Construction and normalization of the structural feature space

Our approach is akin to measuring the distance between two locations not by direct measurement but by using their respective distance to a set of landmarks. For example, the distance between two street corners A and B might be measured by measuring the distance between A to three tall buildings, X, Y, and Z and also measuring the distance between B to the same X, Y, and Z buildings. The accuracy of such triangulation will depend on the relative location and the number of such landmark buildings. The advantage is that we do not have to make direct measurements between A and B, which might be difficult (e.g., because the streets are blocked).

Here, we used Rfam CMs as our landmarks to triangulate RNAs of unknown secondary structure, which enabled us to identify groups of similarly-structured RNAs (motifs) without explicitly predicting the structures of those RNAs. CMs are a form of stochastic context-free grammar used by the Rfam database to model the consensus sequence and secondary structure of RNA structure families [5,6]. We used all 1,973 CMs in Rfam v.10.1 to create an empirical feature space for triangulation and clustering of RNAs. The raw feature space consisted of 1,973 dimensions, each corresponding to one CM. The coordinates of an arbitrary RNA sequence within this space was determined by scoring it against each CM using the *cmscore* module of Infernal (v.1.0.2) [27] and using the resulting bitscores as the coordinates along each axis. These bitscores indicate how well a sequence matches each CM, taking into account compensatory base changes that maintain conserved pairing interactions. Thus, the feature space can map RNA sequences according to their similarity to known structures. We note that although scoring an RNA sequence against a CM can be considered a form of alignment, there was distinctly no pairwise sequence alignment of the RNA sequences to each other during this stage of the algorithm. Therefore, in contrast to existing alignment-based clustering algorithms, our algorithm had linear growth in the number of "alignments" with increasing dataset size, rather than quadratic growth. Although the subsequent clustering step in our method was quadratic [28], in practice this part of the process was much faster than in alignment-based algorithms because only a simple distance measure needed to be calculated for each comparison, rather than an alignment (that will typically add another quadratic factor in terms of sequence length).

Initial analysis of the raw feature space using randomly selected transcript sequences revealed a relationship between the length of an RNA sequence and the score it received against a CM (Fig. 2-1A). For a given CM, this relationship was strongest for sequences that were shorter than the length of the CM itself and indicated that shorter sequences were being penalized in a manner proportional to their deficiency in length. We also observed that larger CMs tended to produce lower scores on average, even when only considering sequences longer than the length of the CM (Fig. 2-1B). To normalize for these two length effects, we separately estimated the mean and standard deviation of scores for each combination of sequence length (between 10nt and 500nt) and CM, and used these parameters to produce Z-standardized scores (Z-scores) according to the length of the original sequence and the particular CM. Specifically, the Z-score Z for a sequence of length l against CM c is calculated as $Z = (x - \mu_{lc}) / \sigma_{lc}$, where x is the raw score and μ_{lc} and σ_{lc} are the mean and standard deviation, respectively, of the scores of sequences of length l against CM c. We applied this normalization to an independent dataset and found that this procedure greatly reduced the relationship between sequence length and score (Fig. 2-1C) and zero-centered the range of scores produced by each CM (Fig. 2-1D).

Although Rfam CMs model a wide variety of structures, there are several subgroups of CMs that are structurally related (e.g. microRNAs) that may therefore produce very similar scores for a given RNA sequence even if the sequence does not belong to the CM model families. In agreement with this, we observed correlation in the scores produced by several groups of CMs; for example, mir-70 (RF00833) and mir-355 (RF00797) had a Spearman correlation of 0.72 in their scores against random sequences. These kinds of correlation over random sequences imply structural correlation of the models rather than biological correlation of the sequences and as such the model correlations are likely to distort the biological information from the ensemble of the CMs. To reduce our feature space to a set of independent axes, we first assessed the structural correlation of the CM models by measuring their length-normalized scores (Z-scores) over a randomly sampled set of 24,550 sub-sequences from the mouse and human transcriptome (see "Normalization of feature space" in Methods). We then performed principle components analysis (PCA) on the Z-scores, which resulted in an orthogonal set of axes (i.e., uncorrelated) ordered by the total variance explained by each coordinate. We selected the first 100 principle component axes as representing informative variation (see “Normalization of feature space” in Methods) and used the loadings of these axes directions to construct our final feature space for subsequent measurements. Another view is to think of the loadings as a set of weights on the CM Z-scores that results in a 100-dimensional RNA structure feature space. We refer to this space here as the RNA Empirical Structure Space (RESS). Each RESS coordinate is a weighted linear combination of the CM Z-scores; therefore, the RESS feature scores of a given sequence can be back transformed into individual CM Z-scores and analyzed in terms of Rfam models as demonstrated later in our Results section. The contributions of each CM to each RESS axis, as well as the correlations of each axis with GC content, CM length, and number of hairpins, are available on our supplementary website (kim.bio.upenn.edu/software/nofold.shtml).

2.2.2 Suitability of the RESS for structure similarity analysis

We first asked whether structurally similar sequences become grouped together when mapped to the RESS. As an initial test, we created three synthetic structures of the same length but with different numbers of hairpins (Fig. 2-2A) and generated sequences that had the appropriate base complementarity to form each of these structures. These sequences were generated randomly (but respecting pairing constraints; see “Synthetic structures” in Methods) to ensure that the members of each structure group were not trivially similar on the primary sequence level. We created 50 sequences for each structure and verified that, as expected, the sequences appeared random on the primary sequence level (25% average pairwise sequence identity). We scored the sequences against the Rfam CMs and projected them into the RESS. As an initial assessment of the relative positioning of the sequences within the RESS, we visualized the sequences using PCA ordination of the 100-dimensional RESS coordinates (Fig. 2-2B). The different structural sequences formed three well-separated clusters along the first and second PC axes, indicating that the RESS mapped the sequences with similar structure closer together than sequences of different structure.

We next sought to define a distance measure that could be used within the RESS to identify structurally related sequences. An appropriate distance measure should assign a small distance between pairs of related structures and a larger distance between pairs of unrelated structure. To test this, we used our dataset of synthetic structure sequences to calculate distance measures on (1) pairs of sequences with the same structure, (2) pairs with different structure, and (3) pairs of completely random sequence. We found that Spearman distance (defined as one minus the Spearman correlation across RESS coordinates) worked well to distinguish the pairs of related structure from other types of pairs, and was a marked improvement over sequence identity alone (Fig. 2-2C) or Euclidean distance (see supplementary website). We therefore used this measure as the basis for identifying similar structures and clustering.

2.2.3 Automated structural clustering for motif identification

Towards the goal of identifying secondary structure motifs in large sequence datasets, we developed a pipeline for clustering sequences within the RESS and automatically extracting clusters with a sufficiently small diameter (calculated as the average pairwise Spearman distance among the cluster members). We call this pipeline "NoFold" to highlight the fact that it does not use folding or alignment in the initial steps of sequence comparison and clustering. The overall steps of the pipeline are illustrated in Fig. 2-3 and explained in detail in the Methods. Briefly, input sequences were scored against the 1,973 Rfam CMs, normalized and mapped to the RESS, and clustered by average-linkage hierarchical clustering using Spearman distance as the distance measure. The resulting hierarchical tree was cut into all possible clusters with three or more members, and all non-overlapping clusters with a diameter below a certain threshold were extracted. The threshold was designed to control the false positive rate (FPR) and was derived from the distribution of cluster diameters that we observed when clustering randomly generated sequences. The threshold was set such that only about 5% of non-structural clusters will have a small enough diameter to pass this filter. To improve the sensitivity of the method, we aligned and folded the sequences within each passing cluster using LocARNA and used this to train a new CM for each cluster ("cluster-CMs"). We then used each cluster-CM to search the original sequence dataset for additional instances of the modeled structure, similarly to what has been done in GraphClust [23] and CMfinder [22]. When searching the dataset, sequences were allowed to match to multiple cluster-CMs, which can occasionally lead to substantial overlap between the final clusters. We therefore merged any clusters that overlapped by > 50% of their members.

To test the ability of NoFold to identify multiple structure motifs simultaneously, we created a dataset consisting of sequences from the seed alignments of 20 Rfam structure families that varied widely in size and structure (Table 2-1). The sequences of each family were filtered such that no pair of sequences shared more than 75% sequence identity (after alignment), which resulted in an average sequence identity of 32-54% per family and a total of 978 sequences. We used this dataset to test NoFold under three conditions: (1) a basic test using the exact sequences reported by Rfam (“plain sequences”), (2) a test where 10-50nt of random sequence was added to both ends of every sequence (“embedded sequences”), and (3) a repeat of the first test but with the addition of 3,000 random, unrelated sequences matched to the di-nucleotide frequency and length distribution of the Rfam sequences (“plain sequences with background”). These last two tests were designed to emulate common, yet challenging situations in RNA structure analysis where the exact boundaries of the RNA structures are not known (test 2) or a large proportion of the sequences in the dataset do not contain an instance of a motif (test 3).

We note that since the Rfam families used in these test datasets are also represented directly by CMs that form the basis of the RESS, this potentially makes clustering of these sequences easier for NoFold. To reduce this effect, we removed from the feature space the test family CMs and any CMs that appeared to be very similar to one of the test families. We did this by examining the Z-scores (before projection into the RESS) of each test family against all CMs and removing CMs with an average Z-score > 3 for any family. Since the parameters used to calculate Z-scores are derived from a large sample of transcript sequences, a high Z-score for a given CM indicates that a sequence is more similar to that CM than what is typically observed. This procedure resulted in the removal of 44 CMs (see “Rfam benchmark tests” in Methods for full list). We verified through linear discriminant analysis that the top discriminating CMs for this dataset were not related to the dataset families after this removal process. All Rfam tests were carried out using this modified feature space.

We compared the performance of NoFold to GraphClust on the three test sets described above (Table 2-1). Default parameters were used for both methods, with the exception that sliding window generation was turned off for GraphClust so that full-length structures would be clustered (we note that this may negatively affect the performance of GraphClust). We measured performance based on how well each family was reconstructed in the final set of clusters. In this context, we defined family *sensitivity* as the fraction of sequences from that family that were present in any cluster dominated by that family, and family *precision* as the fraction of sequences in clusters dominated by that family that actually belonged to that family. Both NoFold and GraphClust performed very well, but NoFold consistently detected more of the families and had a higher average sensitivity than GraphClust in all three tests. NoFold also had a slightly higher proportion of families that were detected in a single cluster rather than being split into multiple separate clusters (Fig. 2-4). Family sensitivity was not significantly correlated with the standard deviation of family sequence length (NoFold: r = -0.005, p = 0.98; GraphClust: r = 0.18, p = 0.45), indicating that the good clustering performance was not simply due to length similarity within families. Notably, both methods had very high precision (0.98-0.99) across all tests and did not return any clusters dominated by background sequences in the third test, indicating that these methods can appropriately distinguish between clusters of related and unrelated structure. The test set where sequences were embedded in random flanking sequence proved to be the most difficult, resulting in an average sensitivity drop of about 0.15 for both methods. The performance drop for each family was significantly correlated with the length of the sequences in the family (Spearman correlation -0.53, $p < 2.2e-16$), indicating that detection of smaller structures was impacted the most. We note that although some of the test families were related to each other (e.g. RF00009, RF00010, and RF00011), both NoFold and GraphClust were generally able to separate these families into separate clusters. Overall, these results demonstrate that NoFold can simultaneously detect multiple structural motifs of different sizes with very high sensitivity and precision and is comparable to or exceeds the performance of the current state of the art software.

To verify that NoFold can perform well on structures that bear absolutely no evolutionary homology to CMs in the feature space, we additionally performed clustering on the sequences derived from the three synthetic structures described in the previous section. The results of this test for NoFold and GraphClust are summarized in Table 2-2. GraphClust detected all members of the 1-hairpin and 2-hairpin families, but did not detect the 3-hairpin structure. In contrast, NoFold detected all three structures with reasonable sensitivity. Most notably, the average precision of the NoFold clusters was much higher than the GraphClust clusters (0.81 vs. 0.53, respectively), suggesting that the use of information from Rfam CMs by NoFold improved clustering even though the synthetic structures were not members of any Rfam family. Upon individual inspection of the clusters, we found that the GraphClust clusters each contained a substantial mix of all three structures, with a high degree of overlap between each cluster. For example, the largest cluster contained all 50 of the 1-hairpin sequences, but also contained 38 of the 2-hairpin sequences and 18 of the 3-hairpin sequences. The NoFold clusters, in contrast, were generally much more specific to a single family, as is reflected in its higher precision. Although it is possible that fine-tuning some of the GraphClust parameters (such as the number of clustering iterations) may improve its performance in these tests, these results are meant to represent the "out-of-the-box" performance of each method. Altogether, these results demonstrate that NoFold can reliably detect structure motifs in the complete absence of sequence conservation or homology to the feature space.

Finally, we performed clustering on the entire Rfam database using a setup similar to a cross-validation analysis. Specifically, we grouped all 1,973 Rfam families into 10 subsets such that similar families were put into the same subset. This grouping was done by hierarchically clustering the CMs based on their scores against random sequences and then cutting the dendrogram to create exactly 10 clusters. The CMs in each cluster then determined which families were grouped together for the analysis (see "Rfam benchmark tests" in methods). For each subset, we extracted up to 15 sequences per family such that no pairwise sequence identity exceeded 75%. We removed any families with less than 3 sequences, resulting in a total of 937 families (6085 sequences) included across all subsets. We ran each subset separately through NoFold, removing any CMs from the feature space that had an average Z-score > 3 for any family, as described above. GraphClust was run for 25 iterations (10 clusters/iteration) on each subset. The average family sensitivity across the 10 subsets was 0.57 for NoFold and 0.55 for

GraphClust (0.51 and 0.55, respectively, when averaging directly across the families rather than the subsets). The lower sensitivity of both methods in this test reflects the inherent difficulty of this test compared to the 20-family test, as it requires the methods to separate many more families simultaneously, and each subset may contain several related families with similar structure. In addition, the performance of NoFold was likely impacted by the need to remove large portions of the feature space for each subset. The specificity of both methods remained high at 0.99. Full results of this analysis are available on our supplementary website.

2.2.4 Application of NoFold to novel motif discovery

Dendritic localization

An important process in neurons is the localization of specific transcripts to the dendrites, which allows for local translation and spatially restricted synaptic remodeling [29–31]. Targeting of transcripts to the dendrites is thought to be mediated primarily by RNA binding proteins, which recognize *cis*-elements on the transcripts called dendritic targeting elements (DTEs). Under the assumption that some DTEs may be motifs that appear across multiple different transcripts, it should be possible to identify these motifs computationally. However, despite much work over the last 25 years to pinpoint such motifs, only a few have so far been found [32,33]. Given that almost all previous searches for DTEs have focused on primary sequence motifs, we asked whether it might instead be secondary structures that provide the common recognition element between transcripts.

We decided to apply NoFold to a dataset of known dendritically localized transcripts from rat to see if we could identify any structural motifs enriched in these sequences, which might explain their localization.

To aid in the functional interpretation of novel motifs, we added several types of automatic annotations to NoFold. First, since we had already scored each sequence against all Rfam CMs in the first step of NoFold, we made use of this rich source of information in order to annotate each cluster with the Rfam families it most resembles. To do this, we calculated the average Z-score of the sequences in the novel cluster for each CM and reported the 10 CMs with the highest average Z-score. As mentioned previously, the parameters for calculating the Z-scores were derived from an independent sampling of transcript sequences, so a high Z-score (> 3) for a CM indicates that a sequence scored unusually well against that CM compared to the general transcriptome. Averaging Z-scores across a whole cluster tends to highlight the CMs that scored highly for multiple sequences in the cluster, suggesting a structural resemblance to the family modeled by these CMs. Although a high Z-score does not necessarily indicate functional homology, we have found it to be a useful first-pass annotation to guide deeper analysis. For additional annotation, we also created a multiple alignment and predicted a consensus structure for each final cluster using LocARNA. Using this alignment, we ran RNAz [34] with default parameters to obtain several statistics such as the structure conservation index (SCI). We note, however, that these statistics should be interpreted with caution because RNAz was trained on different window sizes and different types of alignments.

Finally, we automatically trained a new CM for each final cluster which can be used in the future to search additional databases for instances of the motifs.

As a first step towards identifying structural DTEs, we compiled a list of 211 transcripts with experimental evidence for dendritic localization in rat neurons. From each transcript, we obtained from RefSeq (rn4) the 3’UTR sequence as well as the sequence of any cytoplasmically retained introns [35], which have previously been shown to harbor DTEs [36]. To focus our search on smaller structure elements, we used a sliding window approach to split each 3’UTR and intron sequence into several smaller segments. We have validated that the use of a sliding window still allows for good sensitivity of motif detection (see supplementary website). We created 50nt and 150nt sliding window sets for the retained intron and 3’UTR sequences of the dendritically localized transcripts and searched these regions for motifs using NoFold (Table 2-3). NoFold identified a total of 290 clusters (“motifs”) that contained three or more sequences. To test whether these motifs were enriched within dendritic transcripts, we created a background datasets consisting of introns or 3’UTRs (RefSeq, rn4) from non-dendritically localized transcripts and scanned this set for matches to the NoFold motifs (see “Dendritic localization dataset” in Methods). This was done using the cluster-CM for each motif in conjunction with the *cmsearch* program [27]. We compared the number of motif matches between the dendritic sequences and non-dendritic sequences and found a total of 213 of the motifs were significantly enriched in the dendritic transcripts (Fisher’s exact test, FDR-adjusted $p < 0.05$).

Previously, Buckley and colleagues found that a ~74nt hairpin structure within the retained introns of several dendritic transcripts was sufficient to confer dendritic localization in rat hippocampal neurons [36]. These structures were instances of the ID element, a type of rodent SINE retrotransposon element that likely arose from the dendritically-localized *BC1* gene [37]. We asked whether the ID element structure was among the motifs found by NoFold in our intron sequences. We found two motifs in the 50nt set (M28 and M51) and one motif in the 150nt set (M3) that had high sequence identity with the ID element, all of which were significantly enriched in the dendritic introns (Fisher's exact test, FDR-adjusted $p < 0.05$). M3 was additionally predicted to form a highly similar structure to the ID hairpin (Fig. 2-5A). This cluster contained sequences overlapping 10 of the 12 BLAST hits for the ID element within the intron sequences (see "Dendritic localization dataset" in Methods), and additionally contained one extra instance of the ID element not found by BLAST. Although this extra sequence had low sequence identity with the ID hairpin sequence (59%), it was structurally conserved (SCI = 0.83) and was predicted to form a similar hairpin structure. Using the top ten CM list annotation generated by NoFold, we found that the tRNA CM was the top CM for M3 by average Z-score (Z = 4.87), which is not surprising given that the ID element and *BC1* RNA are evolutionarily related to alanine tRNA. We note that despite this similarity, scanning the full length intron sequences with the tRNA CM using the traditional Rfam *cmsearch* only identified four instances of the ID element, highlighting the improved sensitivity that NoFold provides for motifs that are not directly modeled in Rfam.

In addition to the ID element, we also identified several motifs with similarity to known localization elements from *Drosophila*. Most strikingly, we found that 37 motifs were annotated as having the K10 transport/localization element CM (K10_TLS; RF00207) among their top ten best CMs, with five of these motifs having an average Z-score > 5 and 28 having a Z-score > 3 for this CM. The K10_TLS is a 44nt hairpin structure that mediates localization of the *K10* mRNA during *Drosophila* oocyte development [38]. The majority of our K10_TLS-like motifs were predicted to have a stem-loop consensus structure enriched with AU base pairs (72% AU-content on average), similar to K10_TLS (Fig. 2-5B), although primary sequence identity was low. Overall, these 37 clusters encompassed a total of 60 unique genes, which is 28% of the total genes in the datasets, and 28 of the clusters were significantly enriched in dendritic transcripts (Fisher's exact test, FDR-adjusted $p < 0.05$). We also found nine motifs with another *Drosophila* localization structure, the Wingless localization element 3 (WLE3; RF01046), within their top ten CMs, although only one had an average $Z > 3$. To our knowledge, a role for these motifs has not yet been described in mammals. Additionally, we identified several potentially novel motifs with stable and conserved structure, such as hairpin motif M172, which is found in six dendritic transcripts, and double-hairpin motif M158, which is found in four transcripts (Fig. 2-5C). Full data on all identified motifs are available on our supplementary website.

Non-canonical translation initiation sites

Translation initiation can be altered by RNA structures that reveal or occlude a potential start codon [39,40] or recruit initiation factors and ribosomes to otherwise unfavorable initiation sites. Structures in this latter category include internal ribosome entry sites (IRES), cap-independent initiation enhancers [41], and certain hairpin-forming nucleotide repeats [42–44]. Two recent studies utilized ribosome profiling in combination with harringtonine [45] or lactimidomycin [46] treatment to capture the locations of initiating ribosomes across the entire mouse and human transcriptomes. Their results revealed that translation initiation at non-AUG codons—including both “near-AUG” codons and completely non-canonical codons—may be more common than previously thought. Although initiation at near-AUG sites in good Kozak context is thought to be possible through wobble base pairing of the methionine tRNA [47], it is unknown whether the traditional ribosome scanning mechanism can support initiation at completely non-canonical sites. Previously, certain IRES [48,49] and hairpin structures [42–44] have been shown to facilitate initiation at non-canonical codons, suggesting that RNA structures may play a central role in this phenomenon.

To determine if novel families of structure could be promoting initiation at these sites, we extracted and clustered 50nt of sequence immediately upstream of each non-canonical translation initiation site (ncTIS) identified in humans by Lee *et al.* (2012). We discovered a total of 21 clusters, all of which were found to be significantly enriched upstream of ncTIS relative to non-ncTIS positions in the same transcripts. Several of these clusters score highly on average for CMs with translation-related functions, such as tRNA-like structures, upstream pseudoknot domains (UPD), and IRES. For example, the top scoring CM for cluster T17 (Fig. 2-6) was the human heat shock protein 70 IRES (*Z*-score = 3.8). Two tRNA-like structures (TLS), TLS-PK3 and TLS-PK2, were also within the top ten best CMs for this cluster (Z = 2.8 and 2.7, respectively). The sequences in cluster T1 (Fig. 2-6) scored highly against the CMs for two human IRES, the insulin-like growth factor II IRES (*Z* = 2.5) and the fibroblast growth factor-2 IRES (*Z* = 2.0). In addition, this cluster scored relatively highly against the tRNA-like TLS-PK4 (p = 8.9e-9).

The largest cluster we found contained six sequences belonging to histone subunit H4 genes, as well as one sequence belonging to heat shock protein 60. This cluster scored highly for the L-myc IRES and is predicted to form a small hairpin (Cluster T6, Fig. 2-6). Interestingly, H4 transcripts were recently shown in mouse to use an unusual mechanism for translational initiation that involves loading of ribosomes independently of the 5’ cap [50]. This process is thought to depend on two RNA structures, one that recruits the cap binding protein eIF4E and another that may help position the ribosome over the initiation site, similarly to an IRES. It has not yet been investigated whether this mechanism supports initiation at non-canonical initiation codons. Several other histone genes were found in other clusters, including two sequences from H2B in cluster T5 and two sequences of H3 in cluster T13. To our knowledge, initiation at non-canonical codons has not yet been investigated in these histone mRNAs.

Altogether, these results suggest that NoFold is useful as a first-pass high-throughput screen to identify the locations of recurring structural motifs in a dataset, which can then be used to prioritize sequences for lower-throughput experimental analyses.

2.3 Discussion

We have described here a novel approach for clustering RNA secondary structures that uses comparison to empirical models to map RNA sequences to a structural feature space (the RESS). By scoring primary RNA sequences across a large number of Rfam CMs and treating the scores as geometric coordinates, the RESS allows interpolation and extrapolation across existing models to identify novel combinations of structural features modeled by the original Rfam CMs. We find that sequences from the same structure family tend to cluster within the RESS and that these clusters can be extracted from unrelated sequences using unsupervised methods with very high sensitivity and precision. We use our approach to identify 213 motifs enriched in dendritically localized transcripts in rat. We hypothesize that some of these motifs may play a functionally important role in dendritic localization given their enrichment within dendritic transcripts and, for several motifs, high scores for CMs related to localization.

Within the dendritic RNAs we identified a large number of clusters that scored highly against the K10_TLS CM. It is unclear whether these clusters represent distinct structure families or are subgroups of one larger structure family that might include K10_TLS. Early studies of the K10_TLS indicated that the size and shape of the structure were most important for localization and that most nucleotides in the stem and loop regions can be changed as long as they do not disrupt base pairing [38]. More recently, a tertiary structure analysis of K10_TLS by NMR spectroscopy revealed that extensive purine stacking within the AU-rich stem region causes K10_TLS to take on an A'-form helix conformation with a widened major groove, and that this geometry is important for localization [51]. Although tertiary features such as this are not directly modeled by CMs and therefore may not be captured by our method, it is possible that the high AU content found in most of our K10_TLS-like motifs could allow them take on an A'-form helix and therefore be localized by a similar mechanism. As these results are still preliminary, additional experiments will be needed to verify these motifs and identify which proteins recognize them.

Of the 21 structure clusters found upstream of human ncTIS, all contained seven or fewer sequences, indicating that no single structure accounts for a large portion of human non-canonical initiation. A possible complicating factor in this analysis is that initiation-promoting motifs do not necessarily occur immediately upstream of the ncTIS. Some IRES are located distally from the start codon and interact with the initiation site by pseudoknot formation [49]. This makes it difficult to find motifs specifically involved in non-canonical initiation, since one must link the distal motif with the ncTIS using either pseudoknot prediction, which is computationally intensive for long sequences, or direct experimental probing. Therefore, we expect that our analysis of only the regions upstream of ncTIS is an underestimation of the motifs involved in non-canonical initiation. In some cases, small hairpin structures located immediately upstream of initiation sites have been shown to help mediate pseudoknot interactions. The Cricket paralysis virus (CrPV) IRES, for example, utilizes a pseudoknot between an ncTIS and a slightly upstream tRNA-like hairpin to cause translation initiation in the absence of initiation factors (including tRNA-Met) [48,49]. Hairpins such as this should be detectable by our analysis, provided they are within the 50nt upstream window used here, and in fact we did obtain several clusters with strong hits for tRNA-like structures and hairpins (e.g. cluster T17 in Fig. 2-6B). It is possible that as more ncTIS are discovered, more instances of these motifs will be found.

Beyond the experimental dataset considered here, there are many possible applications of NoFold. For example, to identify structures bound by a particular RNA-binding protein, one could analyze sequences that are known to be bound by that protein to see if any common motifs emerge. A similar tactic could be applied to find motifs involved in splicing, RNA stability, and translational efficiency. The RESS itself could also be used directly as a feature space for supervised classification of RNAs, e.g. classification of unannotated non-coding RNAs into broad functional categories, as has been attempted using other types of features [52].

We note that since the scoring process scales linearly with increasing dataset size, this approach is feasible for datasets up to several thousand sequences. Specifically, on one CPU core, a single 50nt sequence was scored in an average of 0.012s per CM, or ~24s for the entire Rfam CM set. Since the scaling for increasing sequence lengths is quadratic, we generally recommend using sequences or sliding windows of < 300nt. We have implemented an option to parallelize the scoring process and several of the downstream steps of NoFold, which can greatly decrease runtime when the appropriate hardware is available. Runtime for the downstream steps of the NoFold process generally depended on the number of clusters that passed the thresholds, but usually took substantially less time than scoring. Although the overall runtime of GraphClust was generally shorter than NoFold on a single core (3 minutes for GraphClust vs. 39 minutes for NoFold on a 100-sequence dataset), NoFold was sped up considerably when parallelized (4.2 minutes on 16 cores for the same dataset). In contrast, we observed that GraphClust did not always make use of all available cores (2.2 minutes on 16 cores for the same dataset). This appears to be dependent on the number of clusters that were actually found.

An important limitation of our approach can arise from the use of empirical models to construct the feature space. An ideal set of empirical models should comprise all of the major structures of RNA such that any RNA structure can be placed “inside” the coordinates. By using all available models, we hoped to create such a feature space, but we do not have any guarantee. Another remaining limitation of our method is the detection of structures embedded in larger sequences. Here we used a sliding window to segment larger sequences to aid in detecting such structures, at the expense of some sensitivity. More sophisticated methods that might optimize for subsequence structures will yield improvements in this area. The development of alternate methods for segmenting large sequences will likely continue to improve the sensitivity of NoFold and other existing motif finders. Another avenue for improvement is in cluster delineation. Here we developed several data-driven criteria for cluster identification, but many other machine learning approaches may be applied to the basic concept of RESS.

An interesting future consideration will be the tailoring of different collections of empirical models to suit specific applications. Although here we used the entire set of Rfam v.10.1 CMs to define our feature space, different utility might be found using different subsets of CMs (or other models). As discussed in the introduction and results, the coordinate space established by the RESS using the CMs may be seen as a set of canonical models against which novel sequences are compared to assess their inter-relationships. We hypothesize that if the models are at large scale (e.g., a sparse set of very different secondary structures), this is akin to having very coarse-grained models and such a subset of models (i.e., CMs) may be useful for large scale structure discrimination but not for fine-scaled differences. Alternatively, we hypothesize that a set of closely related CMs may help discriminate fine-scaled differences. Thus, future work may entail using different subsets of CMs and resulting RESS coordinates for different subgroups of structures.

2.4 Methods

Data and Software

NoFold is available on our website, kim.bio.upenn.edu/software/nofold.shtml. Full clustering results and input datasets used in this study are also available on the site.

Scoring of RNA sequences

Sequences were scored against each of the 1,973 Rfam CMs (v.10.1) using the *cmscore* module of Infernal (v.1.0.2) with options “--search --a” [27].

Normalization of feature space

To obtain normalization parameters, a dataset was generated by extracting sequences of varying length from random locations within transcripts sampled from the whole mouse (UCSC, mm9) and human (RefSeq, hg19) transcriptomes. Any exactly identical sequences were removed. We included 50 sequences of each length in the range of 10-500nt in the dataset, for a total of 24,550 sequences. We used this dataset to obtain the parameters for normalization and standardization of the feature space that were used for all other datasets. First, for each CM, we estimated the mean and standard deviation of scores obtained by sequences of each length. We used these parameters to Z-score sequences in a length- and CM-dependent manner, as described in the text. Next, after normalizing the scores of the 24,550 sequences in this manner, we performed PCA (using *prcomp* in R) on the dataset to obtain a set of independent axes. We retained only the axes with an eigenvalue greater than 1.0 (Kaiser criterion), which yielded 124 axes. We rounded this down to the top 100 axes and recorded the loadings for these axes to use for future datasets. Finally, we recorded a set of parameters to re-standardize the 100 PC axes. All subsequent datasets were mapped to this normalized feature space (the RESS) using the parameters estimated here.

Synthetic structures

We designed the following synthetic structures, which we show below in dot-bracket notation (where matching parentheses represent paired bases and periods represent unpaired bases):

1-hp: (((((((((((((((((((((((((((((((((.....)))))))))))))))))))))))))))))))))

2-hp: (((((((((((((((((((((((.....)))))))))))))((((((((....))))))))))))))))))

3-hp: (((((((((((((((((((....)))))(((((.....)))))(((((....)))))))))))))))))))

Two-dimensional representations of these structures are also shown in Fig. 2-2A. We randomly generated 50 sequences for each structure by generating complementary base pairs simultaneously (but randomly) as defined in the dot-bracket string. This ensured that each sequence had at least the potential to form the exact intended structure. Only Watson-Crick base pairs (A-U and G-C) were used. G-U wobble pairs were not used for simplicity. We did not require that the MFE structure be equivalent to the intended structure, although we note that the majority of the sequences did form the intended structure when folded by RNAFold.

To test distance measures, we generated all possible pairs of sequences from the same structure, different structures, or random sequences (which may or may not have stable structure). For each pair of sequences, we measured their percent sequence identity and their Spearman distance within the RESS, where Spearman distance is defined as one minus the Spearman correlation of the coordinates of the two sequences in the RESS. The random sequences were generated to have the same average di-nucleotide frequency as the structural sequences but had no particular structure. Average di-nucleotide frequency was matched by generating sequences according to a first-order Markov process where the transition probability between each pair of nucleotides was estimated from the sequences of the original dataset.

NoFold structure clustering pipeline

A procedure to delineate robust RNA sequence clusters in the structural feature space was implemented as follows. Scored sequences were clustered by hierarchical clustering (average linkage using Spearman distance) using the *fastcluster* package [28] in R. Using a procedure similar to that described in [53], the resulting dendrogram was cut into all possible clusters of size three or greater and the average pairwise Spearman distance between cluster members was calculated for each cluster (cluster "diameter"); then any clusters with a diameter larger than an empirically derived threshold were removed (see Threshold Determination, below). Since cutting the dendrogram into all possible clusters results in many clusters that contain almost the same sequences, we implemented two filters for choosing non-overlapping clusters: a "sensitive" filter (optimized for picking larger clusters) and a "specific" filter (optimized for picking tighter clusters). In the sensitive filter, clusters are first ranked by their size (large to small) and then by their diameter (small to large). Clusters were then chosen in a greedy manner from first to last, throwing out any clusters that overlap with a previously chosen cluster. In the specific filter, clusters with three or more members were simply ranked by diameter (small to large) and then chosen greedily as above. We tested these two filters using sequences from the BRAliBase II benchmark datatset [11] and found that the specific filter produced fewer false positives but sometimes missed positive examples. To improve the sensitivity of this mode without sacrificing specificity, we implemented an additional cluster-expansion step, where a new CM was trained for each cluster ("cluster-CM") based on the multiple alignment of the cluster sequences by LocARNA. These cluster-CMs were then used to pick up additional matches to the structure within the original sequence database using the *cmsearch* module of Infernal with options "--toponly --glocal". A sequence was counted as a hit for a given cluster-CM if it obtained a bitscore of at least $\log_2$(size of search database), or in the case of the dendritic and non-canonical translation datasets, a bitscore of at least 10. If any two expanded clusters overlapped by more than 50%, they were merged into one cluster. After cluster expansion and merging, each cluster was automatically annotated in several ways to help give insight into potential functions, as described in the text. RNAz was run using default parameters.

Threshold determination

An empirical threshold for filtering clusters based on diameter (average pairwise Spearman distance) was calculated based on the distribution of cluster diameters that result from clustering random, unrelated sequences. Since the expected cluster diameter is dependent on the total number of sequences in the dataset being clustered, we separately calculated this threshold for different database sizes (usually rounding the database size to the nearest 100). For a given dataset size, we also calculated a separate threshold for each cluster size (where size refers to the number of cluster members), since clusters with more members tend to have larger diameters.

We created a dataset of 10,000 random 50nt sequences with the same average di-nucleotide frequency as the mouse and human transcriptomes using a first-order Markov model as described in the "Synthetic Structures" section. Since these sequences were randomly generated, we do not expect them to share substantial structure. Sequences were scored and mapped to the RESS. To obtain the distribution of cluster diameters for a given dataset size, we used the following procedure: (1) a subset of the 10,000 sequences was picked at random to create a dataset of the desired size; (2) the subset was hierarchically clustered using Spearman distances and average linkage and all possible clusters were extracted from the resulting dendrogram; (3) the diameter of each cluster was calculated and recorded in separate lists based on the number of sequences in the cluster; (4) steps 1-3 were repeated enough times to obtain >10,000 observations of clusters of size three (this required more iterations for small datasets and fewer for large datasets). The result of this procedure was a distribution of cluster diameters for each size cluster. A "high-confidence" threshold for each cluster size was then defined as the distance at which 99% of the clusters of that size had a larger diameter than the threshold, and a "good-confidence" threshold was set at the 95% mark. At these thresholds, we would expect about 1% and 5% of structurally unrelated clusters to pass the thresholds, respectively. The 95% threshold was used for choosing clusters in all analyses described here.

Rfam benchmark tests

RNA sequences were taken from the Rfam.seed file available on the Rfam FTP (v.10.1). This file contains sequences from the seed alignments of 1,973 Rfam families. We extracted the sequences for the first 20 Rfam families (RF00001-RF00020) and filtered each family so that no pair of sequences had more than 75% sequence identity. Sequence identity was calculated using the alignments specified in the Rfam.seed file, which is a multiple alignment of the whole family. Insertion characters (e.g. ".") were therefore ignored if they were present in both sequences being compared. After the sequence identity filtering, all remaining sequences in the family were used as part of the benchmark, up to a maximum of 100 sequences per family. Family RF00014 (DsrA) had only one sequence left after filtering (of the original five) and was therefore replaced by RF00032 (Histone3), which was chosen because it is often used in the literature as a structure analysis benchmark family and is a particularly small structure. Altogether, this yielded a dataset of 978 sequences. All information about alignment was removed, including all non-nucleotide characters. We referred to this dataset as the "plain sequences". We additionally generated an "embedded sequence" dataset and a "plain sequences with background" dataset. The embedded dataset was created by adding 10-50nt (amount randomly chosen) of additional flanking sequence to both the 5' and 3' ends of each sequence in the plain dataset. The flanking sequence was matched to the average mono-nucleotide frequency of the plain sequence dataset. The background-containing dataset consisted of the plain dataset with an additional 3,000 random sequences mixed in, such that the random sequences outnumbered the Rfam sequences ~3:1. These sequences were generated to have the same average di-nucleotide frequency as the plain dataset to ensure that di-nucleotide frequency alone was not sufficient to cause clustering of random sequences. Matching of the average di-nucleotide frequency was performed using a first-order Markov process, as described in the “Synthetic structures” section.

After scoring but before clustering, we examined the sequences of each family for particularly high scores against the feature space CMs. We identified all CMs that had an average Z-score > 3 (as calculated using the Z-score parameters described in the “Normalization of feature space” section) and removed these CMs from the RESS. This also required us to re-estimate the RESS PCA projection without these CMs. The full list of CMs that were removed is: 5S_rRNA, 5_8S_rRNA, U1, U2, tRNA, tRNA-Sec, Tymo_tRNA-like, mascRNA-menRNA, tmRNA, Vault, U12, Bacteria_large_SRP, Hammerhead_1, Hammerhead_3, RNaseP_nuc, RNase_MRP, RNaseP_arch, RNaseP_bact_a, RNaseP_bact_b, ACEA_U3, Fungi_U3, Plant_U3, U3, 6S, U4, U4atac, SNORD14, SNORD53_SNORD92, Archaea_SRP, Bacteria_small_SRP, DdR20, Fungi_SRP, Metazoa_SRP, Plant_SRP, Protozoa_SRP, CsrB, CsrC, PrrB_RsmZ, RsmY, mir-299, Y_RNA, ceN72-3, U5, Histone3. Linear discriminant analysis was performed using the MASS package in R, and the top loaded CM for each axis was examined manually. A list of the loadings obtained in this analysis is available on the supplementary website.

NoFold and GraphClust were run on each of the three datasets using default parameters, with the exception that sliding window generation was turned off for GraphClust to make the results more easily compared. It is possible that the use of a sliding window with both approaches could improve performance. Although GraphClust has many parameters that could potentially be tuned to produce better results, we felt that the default parameters were reasonable for the purposes of this test. In particular, the default specifies that GraphClust will be run for two iterations and find up to 10 clusters per iteration, which is theoretically sufficient to identify the 20 expected clusters in this particular dataset. Our results should be interpreted as how each method performs "out-of-the-box", without tuning of parameters or use of *a prioi* knowledge of the size or number of motifs.

Rfam families were grouped for the cross-validation analysis by clustering all of the 1,973 CMs based on their scores against a large set of random transcripts (same dataset as described in "Normalization of feature space" above). Hierarchical clustering using Spearman distance and Ward linkage was used. The dendrogram was cut at a height such that exactly 10 clusters were created by the cut. The CMs in each cluster then determined which families were grouped together for the analysis. The reason for clustering the families in this way was to reduce the number of CM features that had to be removed for each analysis. GraphClust was set to run for 25 iterations (10 clusters per iteration) for this analysis to ensure enough clusters could be detected in each subset. NoFold was run using default parameters.

Dendritic localization dataset

Dendritic transcripts in rat hippocampal neurons were identified by *in situ* hybridization and soma-/dendrite-specific microarrays (unpublished data from J. Kim lab). A transcript was called “dendritically localized” if it had high expression in the dendrites relative to the soma in either the *in situ* or microarray analysis, yielding 182 dendritically localized transcripts. An additional 29 known dendritically localized transcripts in rodents were obtained from [54]. Sequences from the 3’UTR of these transcripts were obtained from RefSeq annotations (rn4) using the UCSC genome browser. If more than one 3’UTR was available for a given gene, only the longest sequence was used. Cytoplasmically retained intron sequence were identified in rat using RNA-seq [35] and those belonging to a dendritically localized transcript were used for the dataset. These sequences consisted only of the regions of the intron that were supported by reads, as described in [35]. Since intron and 3’UTR sequences are long and may contain multiple structures, we generated a sliding window datasets for each using a 50nt window with a 35nt slide or a 150nt with a 105nt slide. Instances of the ID element within the intron dataset were identified by a BLASTn search of the full length retained intron sequences using the default parameters on the BLAST website [55].

As a background dataset, we identified a set of non-dendritically targeted transcripts based on their very low expression in dendrites relative to the soma from the microarray analysis. Introns and 3’ UTR sequences were extracted for a random subset of the top 1000 non-dendritic transcripts and processed as above to create background datasets of 10,000-30,000 windows for each analysis. The GC content of the background datasets was 44-48%, which was similar to the test sequences (43-45% GC). To test a motif for enrichment within the dendritically localized set, we generated a cluster-CM for each final motif using *cmbuild* [27] and used this to search the background dataset as well as the original dataset. The number of hits in each dataset was used in a one-sided Fisher's exact test for enrichment of hits in the dendritic set, and Benjamini-Hochberg multiple testing correction was applied using R.

Translation initiation dataset

The transcript positions of non-canonical translation initiation sites (ncTIS) in mouse and human were obtained from Lee *et al.* [46]. Codons were defined as ncTIS if they were neither AUG nor near-AUG codons but showed translation initiation through ribosome profiling analysis. Since multiple mapping of non-unique ribosome footprints was allowed in the original dataset, we removed any ncTIS that was surrounded by >20nt of sequence that was exactly identical to any other ncTIS. Such ncTIS mostly fell within repetitive elements. We extracted 50nt upstream of each remaining ncTIS, allowing the extracted sequences to overlap by no more than 25nt. If such an overlap occurred, only the first sequence was kept. If 50nt could not be extracted due to an ncTIS falling too close to the 5' end, the 5' end was buffered with random sequence. A background database for the enrichment analysis was created from 50nt upstream of random transcript locations that were not within 25nt of an ncTIS. Only transcripts that had observed expression in the ribosome profiling experiment were used to obtain background sequences.

Figure generation

Plots were generated in R (www.r-project.org) using the ggplot2 package (ggplot2.org). Structure depictions were created using VARNA [56] based on consensus structure and sequence predictions from LocARNA.

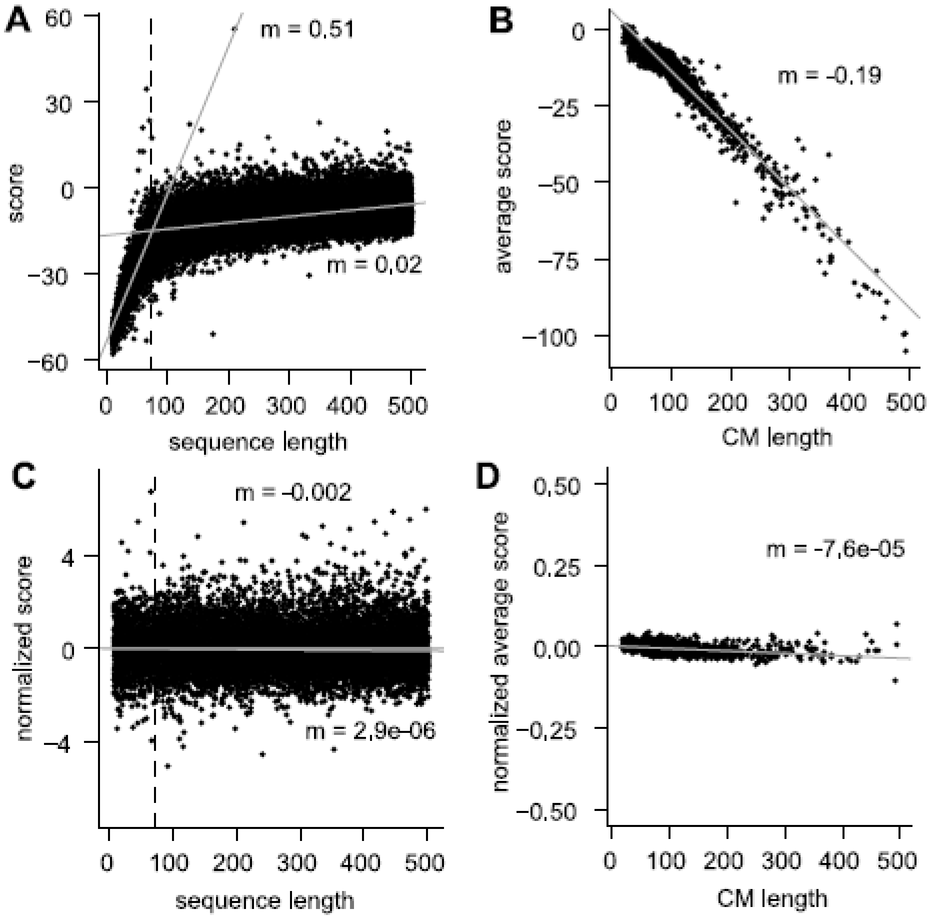

Figure 2-1. Normalization of the empirical feature space.

Examples of CM score characteristics before *(A,B)* and after *(C,D)* normalization, for sequences and CMs of length ≤ 500nt. *(A)* A representative example of the scores given to sequences of various lengths against a single CM, in this case tRNA. We consistently observe a relationship between sequence length and score that is most pronounced for sequences that are smaller than the size of the CM (73nt in this case, indicated by the dashed line). Gray lines show separate linear regression fits to the scores of sequences shorter or longer than 73nt, with slopes (m) indicated. *(B)* We additionally observed a relationship between the length of a CM and the average score that it produces. Average score was calculated based only on sequences with a length longer than the CM. *(C)* The length- and CM-specific procedure to calculate Z-scores greatly reduced the relationship between sequence length and score on an independent dataset. Linear regression fit lines and slopes are indicated as in (A). *(D)* Using Z-scores greatly reduced the relationship between CM length and the average score produced by the CM, and the average score for all CMs was close to zero.

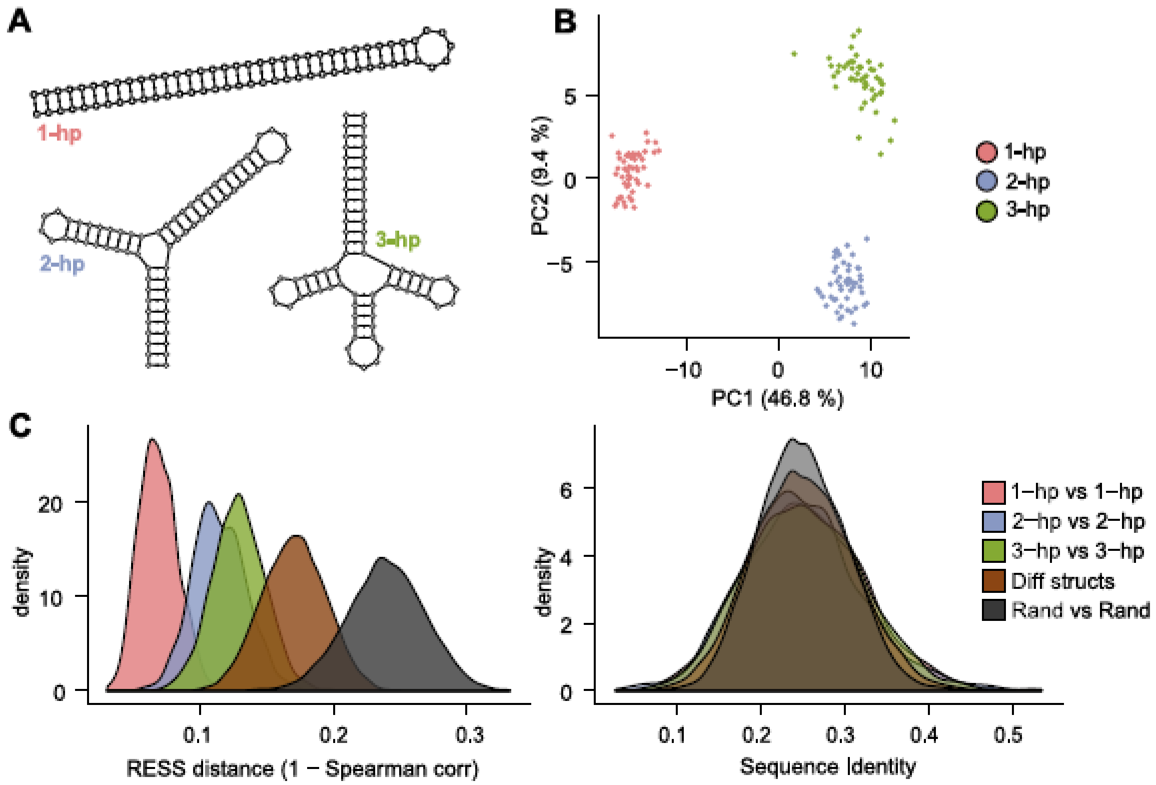

Figure 2-2. Structurally similar sequences are clustered together in the RESS.

(A) Three synthetic structures designed for this analysis. (B) PCA of the structure sequences after projection to the RESS separates the sequences based on structure. (C) Distributions of the distances between pairs of related structure ("1-hp vs 1-hp", "2-hp vs 2-hp", "3-hp vs 3-hp"), pairs of different structure ("Diff structs"), and pairs of random sequences ("Rand vs Rand"). Distance between pairs was calculated by Spearman distance (left panel) or sequence identity (right panel). Related structure pairs were closer, on average, than different or random pairs in the RESS.

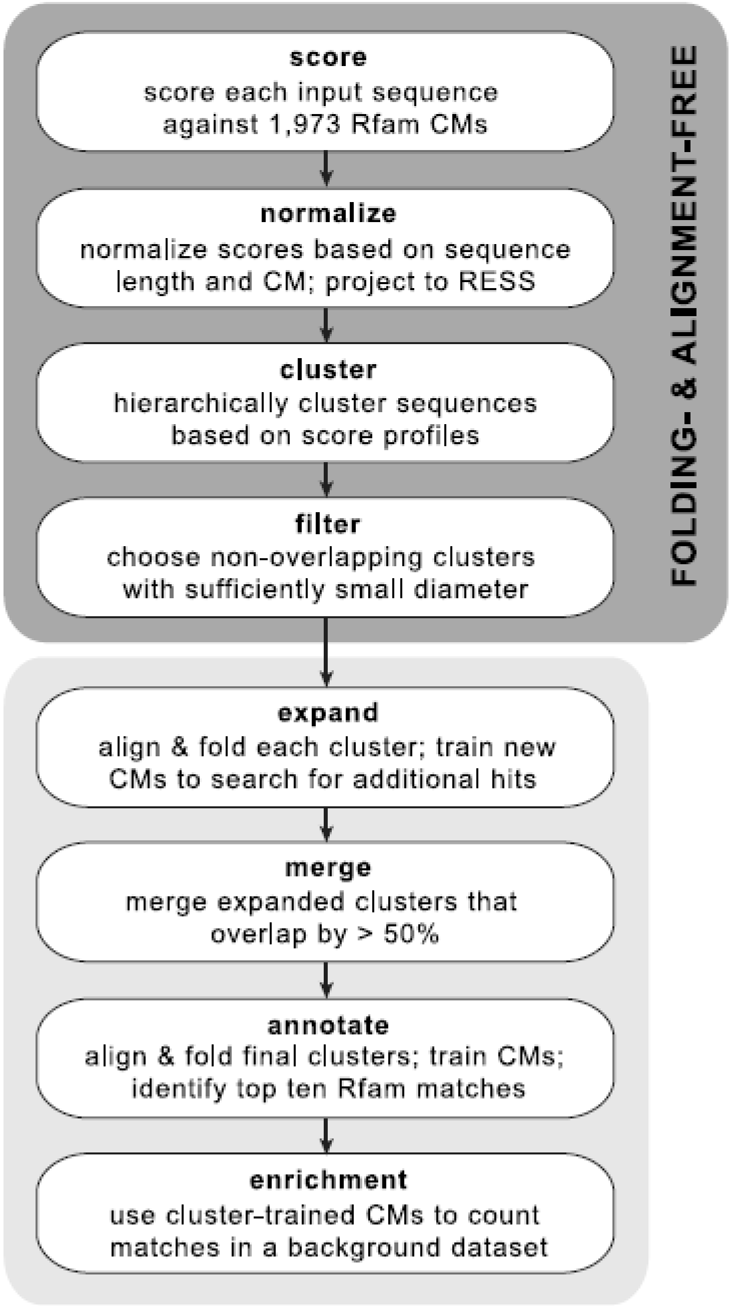
score
score each input sequence against 1,973 Rfam CMs
normalize
normalize scores based on sequence length and CM; project to RESS
cluster
hierarchically cluster sequences based on score profiles
filter
choose non-overlapping clusters with sufficiently small diameter
FOLDING- & ALIGNMENT-FREE
expand
align & fold each cluster; train new CMs to search for additional hits
merge
merge expanded clusters that overlap by > 50%
annotate
align & fold final clusters; train CMs; identify top ten Rfam matches
enrichment
use cluster-trained CMs to count matches in a background dataset

Figure 2-3. Outline of the NoFold approach.

The method does not require structure prediction or pairwise alignment of the input sequences for clustering, in contrast to existing methods.

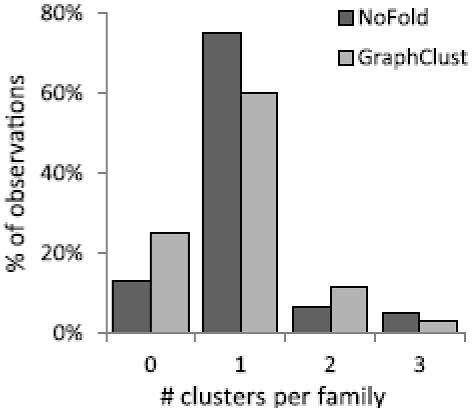

Figure 2-4. Distribution of the number of separate clusters assigned to each Rfam family for a given test.

Clusters were assigned to a family only if it was the dominant family within that cluster. The observations for all 20 families across all three tests are displayed. Most families were assigned to only one cluster per test, and the maximum number of clusters per family in any test was three.

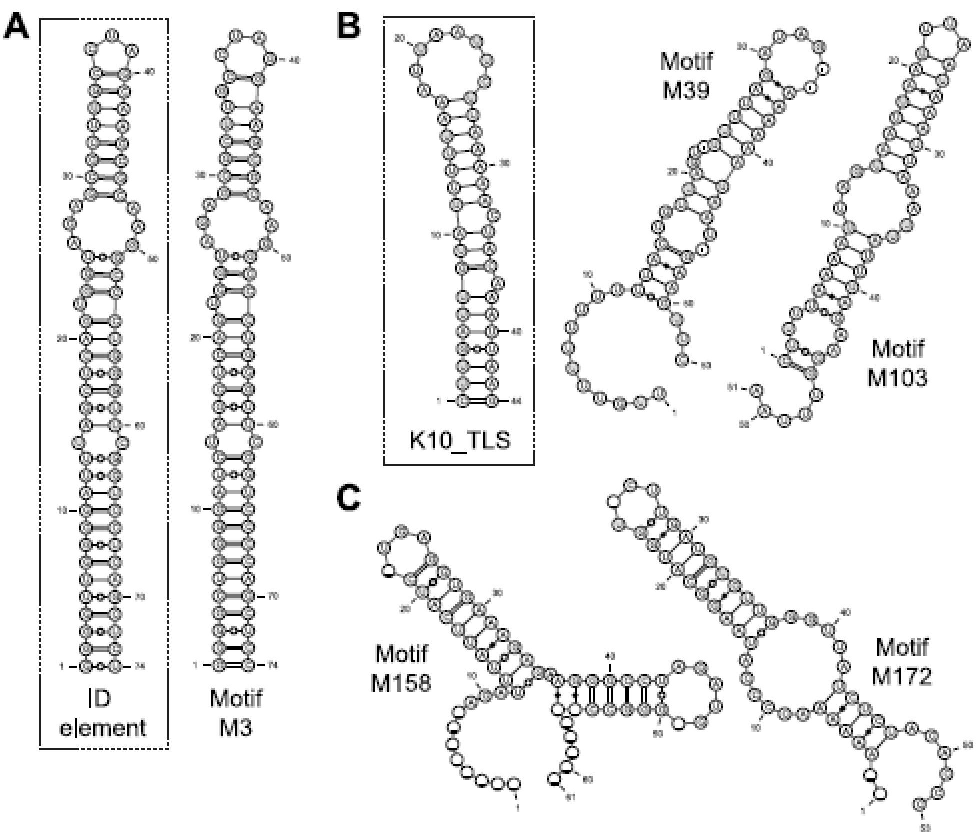

Figure 2-5. Consensus structures of motifs that are enriched in dendritically localized transcripts.

(A) A motif (M3) found within dendritic introns with high sequence and structure similarity to the ID element hairpin (inset). (B) Two motifs (M39, M103) with high average Z-scores for the K10 localization element (K10_TLS, inset) (M39, Z = 5.80; M103, Z = 5.47). Although sequence homology with K10_TLS was low, these motifs share the high AU content characteristic of K10_TLS. (C) Two examples of potentially novel structure motifs (M158, M172) found in dendritic 3'UTRs.

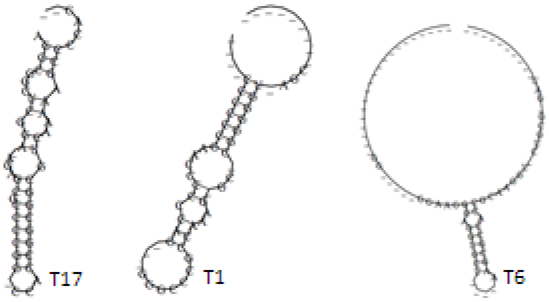

Figure 2-6. Potential translation initiation motifs.

Examples of structures strongly enriched upstream of non-canonical translation initiation sites (ncTIS) that scored highly against IRES, tRNA, and tRNA-like CMs.

Table 2-1. Clustering sensitivity of NoFold and GraphClust for three test conditions on the Rfam benchmark dataset.

					Plain sequences		Embedded sequences		Plain seqs with background	
Family	**Rfam ID**	**#Seqs**	**Avg % ID**	**Avg Len ± SD (nt)**	**NoFold**	**GraphClust**	**NoFold**	**GraphClust**	**NoFold**	**GraphClust**
5S_rRNA	RF00001	100	49%	116 ± 5.2	1.00	1.00	0.20	**1.00**	**1.00**	0.99
5_8S_rRNA	RF00002	22	54%	149 ± 14.7	0.91	**0.95**	**0.86**	0	0.86	**0.95**
U1	RF00003	20	48%	162 ± 5.3	0	0	0	0	0	0
U2	RF00004	70	47%	188 ± 14.4	1.00	1.00	1.00	1.00	1.00	1.00
tRNA	RF00005	100	40%	73 ± 5.2	**0.92**	0.91	**0.72**	0	**0.91**	0.90
Vault	RF00006	52	50%	101 ± 13.5	**0.96**	0.94	0.50	**0.94**	0.94	**0.96**
U12	RF00007	27	46%	165 ± 21.5	1.00	1.00	**1.00**	0.85	0.89	**1.00**
Hammerhead_3	RF00008	13	45%	55 ± 9.3	**0.85**	0	0	0	0.85	**0.92**
RNaseP_nuc	RF00009	68	32%	303 ± 43.3	**0.74**	0.62	0.49	**0.54**	0.50	**0.60**
RNaseP_bact_a	RF00010	100	49%	360 ± 25.8	1.00	1.00	1.00	1.00	1.00	1.00
RNaseP_bact_b	RF00011	41	53%	357 ± 26.3	0	**1.00**	1.00	1.00	1.00	1.00
U3	RF00012	38	41%	204 ± 30.8	0.92	0.92	0.87	**0.95**	**0.82**	0
6S	RF00013	86	38%	181 ± 11.6	**0.98**	0.90	**0.77**	0.60	0.79	**0.99**
U4	RF00015	61	45%	145 ± 21.1	**0.97**	0.95	0.66	**0.95**	**0.97**	0.95
SNORD14	RF00016	7	44%	110 ± 13.9	0	0	0	0	0	0
Metazoa_SRP	RF00017	17	45%	290 ± 33.3	0.94	0.94	0.94	**1.00**	0.94	0.94
CsrB	RF00018	7	53%	340 ± 18.0	**1.00**	0	**1.00**	0	**1.00**	0
Y_RNA	RF00019	24	47%	97 ± 10.5	1.00	1.00	0.96	**1.00**	1.00	1.00
U5	RF00020	82	44%	117 ± 7.2	**1.00**	0.99	1.00	1.00	**1.00**	0.99
Histone3	RF00032	43	45%	46 ± 0.4	**0.86**	0.65	**0.26**	0	0.79	**0.91**
Background	-	3000	25%	215 ± 102.0	-	-	-	-	0	0
				Avg sensitivity	**0.80**	0.74	**0.66**	0.59	**0.81**	0.76
				Avg precision	0.98	**0.99**	**0.99**	0.98	**0.99**	0.98

Table 2-2. Clustering sensitivity and precision of NoFold and GraphClust for the synthetic structure benchmark.

				NoFold		GraphClust	
Family	# Seqs	Avg % ID	Length (nt)	Sensitivity	Precision	Sensitivity	Precision
1-hairpin structure	50	25%	71	0.70	0.80	1.00	0.39
2-hairpin structure	50	25%	71	0.88	0.79	1.00	0.67
3-hairpin structure	50	25%	71	0.58	0.85	0	-
			Average	0.72	0.81	0.67	0.53

Table 2-3. Summary of motifs identified in dendritic localization datasets.

				# Motifs				
Dataset	**#Seqs**	**Window size**	**#Windows**	**≥ 3 seq**	**≥ 5 seq**	**≥ 10 seq**	**Enriched**	**SCI > 0.5**
Dendritic transcripts: retained introns	199	50 nt	1,839	89	13	2	73	33
		150 nt	727	7	7	2	4	0
Dendritic transcripts: 3'UTRs	143	50 nt	3,454	186	24	0	126	87
		150 nt	1,127	12	1	0	10	4

≥ 3 seq, ≥ 5seq, ≥ 10 seq indicates the number motifs found in at least 3, 5, or 10 different sequence windows, respectively. Enriched motifs had $p < 0.05$ after FDR correction.

2.5 References

1 Wan, Y. *et al.* (2011) Understanding the transcriptome through RNA structure. *Nat. Rev. Genet.* 12, 641–655

2 Walczak, R. *et al.* (1996) A novel RNA structural motif in the selenocysteine insertion element of eukaryotic selenoprotein mRNAs. *RNA* 2, 367–79

3 Casey, J.L. *et al.* (1988) Iron-responsive elements: regulatory RNA sequences that control mRNA levels and translation. *Science* 240, 924–8

4 Martin, K.C. and Ephrussi, A. (2009) mRNA Localization: Gene Expression in the Spatial Dimension. *Cell* 136, 719–730

5 Burge, S.W. *et al.* (2012) Rfam 11.0: 10 years of RNA families. *Nucleic Acids Res.* 41, 1–7

6 Eddy, S.R. and Durbin, R. (1994) RNA sequence analysis using covariance models. *Nucleic Acids Res.* 22, 2079–2088

7 Zuker, M. (1989) On finding all suboptimal foldings of an RNA molecule. *Science* 244, 48–52

8 Zuker, M. (2003) Mfold web server for nucleic acid folding and hybridization prediction. *Nucleic Acids Res.* 31, 3406–3415

9 Hofacker, I.L. (2003) Vienna RNA secondary structure server. *Nucleic Acids Res.* 31, 3429–3431

10 Hofacker, I.L. *et al.* (1994) Fast folding and comparison of RNA secondary structures. *Monatshefte fur Chemie Chem. Mon.* 125, 167–188

11 Gardner, P.P. *et al.* (2005) A benchmark of multiple sequence alignment programs upon structural RNAs. *Nucleic Acids Res.* 33, 2433–9

12 Torarinsson, E. *et al.* (2007) Multiple structural alignment and clustering of RNA sequences. *Bioinformatics* 23, 926–32

13 Mathews, D.H. and Turner, D.H. (2002) Dynalign: an algorithm for finding the secondary structure common to two RNA sequences. *J. Mol. Biol.* 317, 191–203

14 Will, S. *et al.* (2007) Inferring noncoding RNA families and classes by means of genome-scale structure-based clustering. *PLoS Comput. Biol.* 3, e65

15 Sankoff, D. (1985) Simultaneous solution of the RNA folding, alignment and protosequence problems. *SIAM J. Appl. Math.* 45, 810–825

16 Ding, Y. *et al.* (2005) RNA secondary structure prediction by centroids in a Boltzmann weighted ensemble. *RNA* 11, 1157–1166

17 Liu, Q. *et al.* (2008) RNACluster: An integrated tool for RNA secondary structure comparison and clustering. *J. Comput. Chem.* 29, 1517–1526

18 Moulton, V. *et al.* (2000) Metrics on RNA secondary structures. *J. Comput. Biol.* 7, 277–92

19 Höchsmann, M. *et al.* (2004) Pure multiple RNA secondary structure alignments: a progressive profile approach. *IEEE/ACM Trans. Comput. Biol. Bioinform.* 1, 53–62

20 Liu, J. *et al.* (2005) A method for aligning RNA secondary structures and its application to RNA motif detection. *BMC Bioinformatics* 6, 89

21 Steffen, P. *et al.* (2006) RNAshapes: an integrated RNA analysis package based on abstract shapes. *Bioinformatics* 22, 500–3

22 Yao, Z. *et al.* (2006) CMfinder--a covariance model based RNA motif finding algorithm. *Bioinformatics* 22, 445–52

23 Heyne, S. *et al.* (2012) GraphClust: alignment-free structural clustering of local RNA secondary structures. *Bioinformatics* 28, i224–i232

24 Scholkopf, B. and Mika, S. (1999) Input space versus feature space in kernel-based methods. *IEEE Trans. Neural Netw.* 10, 1000–1017

25 Moore, S.D. and Sauer, R.T. (2007) The tmRNA system for translational surveillance and ribosome rescue. *Annu. Rev. Biochem.* 76, 101–24

26 Jan, E. *et al.* (2003) Divergent tRNA-like element supports initiation, elongation, and termination of protein biosynthesis. *Proc. Natl. Acad. Sci. U. S. A.* 100, 15410–15415

27 Nawrocki, E.P. *et al.* (2009) Infernal 1.0: inference of RNA alignments. *Bioinformatics* 25, 1335–7

28 Müllner, D. (2011) fastcluster: Fast Hierarchical, Agglomerative Clustering Routines for R and Python. *J. Stat. Softw.* 53,

29 Job, C. and Eberwine, J. (2001) Localization and translation of mRNA in dendrites and axons. *Nat. Rev. Neurosci.* 2, 889–898

30 Sutton, M.A. and Schuman, E.M. (2006) Dendritic protein synthesis, synaptic plasticity, and memory. *Cell* 127, 49–58

31 Bramham, C.R. and Wells, D.G. (2007) Dendritic mRNA: transport, translation and function. *Nat. Rev. Neurosci.* 8, 776–789

32 Eberwine, J. *et al.* (2002) Analysis of subcellularly localized mRNAs using in situ hybridization, mRNA amplification, and expression profiling. *Neurochem. Res.* 27, 1065–77

33 Holt, C.E. and Schuman, E.M. (2013) The Central Dogma Decentralized: New Perspectives on RNA Function and Local Translation in Neurons. *Neuron* 80, 648–657

34 Washietl, S. *et al.* (2005) Fast and reliable prediction of noncoding RNAs. *Proc. Natl. Acad. Sci.* 102, 2454–2459

35 Khaladkar, M. *et al.* (2013) Subcellular RNA sequencing reveals broad presence of cytoplasmic intron-sequence retaining transcripts in mouse and rat neurons. *PLoS One* 8, e76194

36 Buckley, P.T. *et al.* (2011) Cytoplasmic intron sequence-retaining transcripts can be dendritically targeted via ID element retrotransposons. *Neuron* 69, 877–84

37 Kim, J. *et al.* (1994) Rodent BC1 RNA gene as a master gene for ID element amplification. *Proc. Natl. Acad. Sci. U. S. A.* 91, 3607–11

38 Serano, T.L. and Cohen, R.S. (1995) A small predicted stem-loop structure mediates oocyte localization of Drosophila K10 mRNA. *Development* 121, 3809–3818

39 Kozak, M. (1990) Downstream secondary structure facilitates recognition of initiator codons by eukaryotic ribosomes. *Proc. Natl. Acad. Sci. U. S. A.* 87, 8301–5

40 Gu, W. *et al.* (2010) A universal trend of reduced mRNA stability near the translation-initiation site in prokaryotes and eukaryotes. *PLoS Comput. Biol.* 6, e1000664

41 Terenin, I.M. *et al.* (2012) A novel mechanism of eukaryotic translation initiation that is neither m7G-cap-, nor IRES-dependent. *Nucleic Acids Res.* 41, 1–10

42 Zu, T. *et al.* (2011) Non-ATG-initiated translation directed by microsatellite expansions. *Proc. Natl. Acad. Sci. U. S. A.* 108, 260–5

43 Mori, K. *et al.* (2013) The C9orf72 GGGGCC Repeat Is Translated into Aggregating Dipeptide-Repeat Proteins in FTLD/ALS. *Science* 339, 1335–1338

44 Ash, P.E.A. *et al.* (2013) Unconventional Translation of C9ORF72 GGGGCC Expansion Generates Insoluble Polypeptides Specific to c9FTD/ALS. *Neuron* 77, 1–8

45 Ingolia, N.T. *et al.* (2011) Ribosome profiling of mouse embryonic stem cells reveals the complexity and dynamics of mammalian proteomes. *Cell* 147, 789–802

46 Lee, S. *et al.* (2012) Global mapping of translation initiation sites in mammalian cells at single-nucleotide resolution. *Proc. Natl. Acad. Sci. U. S. A.* 109, 1–9

47 Peabody, D. (1989) Translation initiation at non-AUG triplets in mammalian cells. *J. Biol. Chem.* 264, 5031–5035

48 Kanamori, Y. and Nakashima, N. (2001) A tertiary structure model of the internal ribosome entry site (IRES) for methionine-independent initiation of translation. *RNA* 7, 266–274

49 Au, H.H.T. and Jan, E. (2012) Insights into Factorless Translational Initiation by the tRNA-Like Pseudoknot Domain of a Viral IRES. *PLoS One* 7, e51477

50 Martin, F. *et al.* (2011) Cap-assisted internal initiation of translation of histone H4. *Mol. Cell* 41, 197–209

51 Bullock, S.L. *et al.* (2010) A'-form RNA helices are required for cytoplasmic mRNA transport in Drosophila. *Nat. Struct. Mol. Biol.* 17, 703–9

52 Leung, Y.Y. *et al.* (2013) CoRAL: predicting non-coding RNAs from small RNA-sequencing data. *Nucleic Acids Res.* 41, e137

53 Khaladkar, M. *et al.* (2008) Mining small RNA structure elements in untranslated regions of human and mouse mRNAs using structure-based alignment. *BMC Genomics* 9, 189

54 Subramanian, M. *et al.* (2011) G-quadruplex RNA structure as a signal for neurite mRNA targeting. *EMBO Rep.* 12, 697–704

55 Altschul, S.F. *et al.* (1990) Basic local alignment search tool. *J. Mol. Biol.* 215, 403–10

56 Darty, K. *et al.* (2009) VARNA: Interactive drawing and editing of the RNA secondary structure. *Bioinformatics* 25, 1974–5

Chapter 3: Extending empirical structure spaces to protein fold recognition and function prediction

Portions of this chapter will appear in the following article and are reproduced here under a Creative Commons Attribution 4.0 International License (CC-BY).

> Middleton, S.A., Illuminati, J., Kim, J. 2017. Complete fold annotation of the human proteome using a novel structural feature space. *Scientific Reports* (In press).

3.1 Introduction

Although protein sequences can theoretically form a vast range of structures, the number of distinct three-dimensional topologies (“folds”) actually observed in nature appears to be both finite and relatively small [1]: 1,221 folds are currently recognized in the SCOPe (Structural Classification of Proteins—extended) database [2], and the rate of new fold discoveries has diminished greatly over the past two decades. Nevertheless, extending the catalog of protein fold diversity is still an important problem and fold classifying the entire proteome of an organism can lead to important insights about protein function [3–5]. Large-scale fold prediction typically involves computational methods, and the computational difficulty of *ab initio* structure prediction has led to template matching (e.g., using methods such as HHPred [6]) as the most common method for predicting the structure. When sequence-based matching is difficult, other fold recognition approaches must be employed, such as protein threading. Threading-based methods, especially those that combine information from multiple templates, have been among the most successful algorithms in recent competitions for fold prediction [7,8], but are bottlenecked by long run times. Machine learning-based methods have also been used, which can be designed either to recognize pairs of proteins with the same fold [9,10] or classify a protein into a fold [11,12]. Although these methods have shown promising results for a subset of folds, they have so far not been able to generalize to the full-scale fold recognition problem. This failure can mainly be attributed to the severe lack of training data available for most SCOPe folds, as well as the highly multi-class nature of the full problem, which requires distinguishing between over 1,000 different folds [12].

Here we introduce a method for full-scale fold recognition that integrates aspects of both threading and machine learning. At the core of our method is a novel feature space constructed by threading protein sequences against a relatively small set of structure templates. These templates act as “landmarks” against which other protein sequences can be compared to infer their location within structure space. We show the utility of this feature space in conjunction with both support vector machine (SVM) and first-nearest neighbor (1NN) classifiers, and further develop our 1NN classifier into a full-scale fold recognition pipeline that can predict all currently known folds. Applied to the entire human proteome, our method achieves 95.6% accuracy on domains with a known fold and makes thousands of additional high-confidence fold predictions for domains of unknown fold. We demonstrate utility by inferring new functional information, focusing on RNA-binding ability. The structure and function annotations of the entire human proteome are provided as a resource for the community.

3.2 Results

3.2.1 The protein empirical structure space (PESS)

Our approach is based on the idea of an empirical kernel [13], where the distance between two objects is computed by comparing each object to a set of empirical examples or models. We have previously applied this idea to RNA secondary structure analysis [14], and we show here that it can be adapted to proteins. The objects being compared are amino-acid sequences and the distance we would like to compute is similarity of tertiary structure. We selected a set of 1,814 empirical threading templates that describe the three-dimensional coordinates of atoms of proteins of known structures. We use only a small subset of known structures for our template library which we find sufficient to construct an informative structural distance function. Using the threading templates we mapped amino-acid sequences to a structural feature space, where the coordinates of each sequence reflect its threading scores against the templates (see Methods). We refer to this as the protein empirical structure space (PESS). Using the PESS, we trained a classifier to recognize every fold (Fig. 3-1). Since protein domains are the unit of classification in SCOPe, we applied this approach to protein domains as units rather than full proteins.

3.2.2 Fold recognition performance

We tested the PESS in combination with 1NN or SVM classifiers (Fig. 3-2A & B) using three popular benchmarks from the TAXFOLD paper [12]. These benchmarks are designed to test the ability of a method to distinguish between increasing numbers of folds: 27 folds in EDD, 95 in F95, and 194 in F194. Each fold has at least 11 training examples. The accuracy of our classifiers are shown in Table 3-1 along with the results reported by several other published methods [12,15–19]. Our SVM classifier performed the best on all three benchmarks, with the exception of the EDD dataset, where the best performance was from the method of Zakeri et al. when it was used in combination with known Interpro functional annotations. Our 1NN classifier also performed very well on all three benchmarks, outperforming all but our SVM on F95 and F194. We note that some of these publications used slightly modified versions of the benchmarks, which may affect the comparison (see Methods for details). We next asked whether our method actually performed better than simply using the top-scoring template from our feature space. We found that directly using the fold of the top template resulted in 52.1, 56.4, and 57.4% accuracy on EDD, F95, and F194 respectively. Therefore, using the threading scores as a feature space rather than for direct classification improved performance considerably.

The benchmarks described above included only a subset of the 1,221 folds in SCOPe v.2.06. Recognizing all folds simultaneously is challenging; not only is it a highly multiclass problem, but it also suffers from a lack of training examples for a large fraction of the folds. We focused on our 1NN classifier, which requires only a single training example per fold, to scale to the full fold recognition task. To train the classifier to recognize all folds, we downloaded domain sequences from the Astral database [2] corresponding to SCOPe (v.2.06) filtered to less than 20% pairwise identity, which we call SCOP-20. This dataset contains 7,659 sequences covering all 1,221 folds in classes “a” through “g”. The same 1,814 templates were used to extract features, as before. To create a separate test set, we also downloaded the SCOPe sequences filtered to 40% identity and then removed any overlap between this set and the SCOP-20 set. This resulted in 6,322 sequences in 609 folds, which we call the SCOP-40 dataset. Using 1NN classification, 97.6% of SCOP-40 domains were classified into the correct fold (precision=0.964, recall=0.95). Using a combined SVM+1NN classifier (see Methods) did not improve performance (acc=96.9%, precision=0.917, recall=0.938), indicating that the 1NN classifier alone is sufficient for good classification on this dataset. To create a more difficult test, we filtered the SCOP-40 set so all test examples had less than 25% identity with a training example. The classification performance remained strong (acc=96.2%, precision=0.947, recall=0.922). Finally, to rule out any biasing effect of redundancy between test examples and the 1,814 feature templates, we removed any SCOP-40 examples that had more than 25% identity with one of the templates (896 examples). This had virtually no effect on the classification (acc=97.6%, precision=0.956, recall=0.951).

Of the folds represented in the SCOP-20 training set, 86.5% (1,055) have fewer than 10 training examples, and almost half (605) are “orphan” folds with only one training example. Accurate classification into these folds is expected to be particularly difficult due to the small amount of training data. To determine how well our method performs relative to the number of training examples, we calculated precision and recall separately for each fold based on the SCOP-40 classification results. Although performance on folds with fewer training examples was slightly worse overall, the vast majority of folds had perfect precision and recall, regardless of training size (Fig. 3-2B & C). Focusing specifically on orphan folds, for which classification should be most difficult, we found that 96.4% of the 275 training examples belonging to these folds were correctly classified, which was only slightly lower than the overall SCOP-40 accuracy. Thus, our method can accurately recognize folds even when there is a single training example.

3.2.3 Proteome-scale fold prediction of human proteins

The ability of the PESS to accurate recognize all folds with relatively little threading makes it well suited for classifying large, proteome-scale datasets. Here we applied our new method to predicting the fold of protein domains curated from the entire human proteome. Since the 1NN-only classifier performed better than the SVM+1NN combined classifier on the full-scale fold recognition test, we used the 1NN-only classifier to predict the folds of all human protein domains.

An overview of our whole proteome fold classification pipeline is shown in Figure 3-3A. In contrast to SCOP-derived benchmarks, whole proteomes present several additional challenges for fold recognition. One of the major bottlenecks is the process of segmenting whole proteins into domains, which is often slow and error-prone. We did not attempt to address this issue here, but instead make use of the existing domain segmentation of the human proteome performed by the Proteome Folding Project [5]. Another challenge is recognizing domains that do not belong in any of the known fold categories, e.g. due to segmentation errors, being disordered, or belonging to a previously undiscovered fold. To address this problem, we defined a distance threshold for classification based on the typical distance between a domain and its nearest neighbor when the true fold of the domain is not represented in the feature space (see Methods). When a query domain's nearest neighbor is farther than this threshold distance, the domain is assigned to a "no classification" category (Fig. 3-3A).

There were a total of 34,330 human domains with length greater than 30 residues in the Proteome Folding Project dataset, corresponding to 15,619 proteins. Of these, 20,340 domains (59%) had a nearest neighbor within the distance threshold and were classified into an existing fold by our method. Only 128 of these domains were previously placed into a fold with high confidence by the Proteome Folding Project [5]. To test how well our predictions match with what is currently known about human protein structures, we used a blastp search against PDB to identify 2,211 human domain sequences with a "known" fold; that is, an identical or highly similar PDB entry with a SCOPe fold classification. Our classifier made a fold prediction for 1,873 (84.7%) of these domains, and 95.6% of these predictions exactly matched the known SCOPe fold.

Overall, 757 of the 1,221 SCOPe folds had at least one human domain predicted by our method. The distribution of domains across folds was highly skewed, with the majority of folds having only a few predicted domains and a small number of folds having many (Fig. 3-3B). This agrees with previous observations that domains are not evenly distributed in protein structure space [1,20]. The top 10 folds accounted for 38.9% (7,908) of the classified domains, and the most common fold (Beta-beta-alpha zinc fingers) alone encompassed 9.1% (1,853) of the fold predictions (Fig. 3-3C). A full list of fold predictions is available on our website (see “Data and Code Availability” in the Methods).

Human RNA-binding proteins

RNA-binding proteins (RBPs) are an important class of proteins that function in almost all aspects of RNA biology, including splicing, translation, localization, and degradation. It would be valuable to fully define which folds have potential RNA binding function and use this information to improve our annotations of RBPs. We obtained a list of 1,541 currently known RBPs in humans from a recent RBP census [21] and extracted the corresponding domains from our dataset. There were 1,816 domains with fold predictions, matching 243 different folds.

Since not every domain in an RBP is expected to actually bind RNA, we first sorted these folds into “likely RNA-binding domain (likely RBD)” and “likely auxiliary” groups. The RBPs in the census were primarily identified based on hits to a list of Pfam families with RNA-binding function, so we defined the likely RBD folds as those with at least two RBP domains with a hit ($E < 0.01$) to this RNA-binding Pfam list. There were 720 such domains which encompassed 78 different folds. The most common folds included several with well characterized RNA-binding function, such as Ferredoxin-like, which includes the RNA recognition motif (RRM); Eukaryotic type KH-domain (KH-domain type I); and dsRBD-like (Fig. 3-3D). Next, we defined the auxiliary folds as those with at least one RBP domain but fewer than two hits to the RNA-binding Pfam list. By this criteria, we identified 165 folds, the most common being the Cytochrome C fold (14 domains) and RING/U-box E3 ligase fold (12 domains). These folds are likely to represent other functions performed by the RBPs; however, we note that the lack of a Pfam match does not preclude RNA-binding function, so some of these auxiliary folds may in fact be RNA-binding.

The RBP census contained 21 cases where a protein was known to bind RNA but the type of RBD was not yet identified. Using our method, we matched three of these RBPs to one or more of the likely-RBD folds established above. One of these RBPs was Fam120a (also called C9orf10), which was previously found to have RNA-binding activity at its C-terminal end, but the type of RNA binding domain was not determined [22]. Our method predicted a DNA/RNA-binding 3-helical bundle fold within the RNA-binding region of this protein. Loosening the classification threshold slightly (NN distance $\leq$ 20) allowed us to identify potential RBDs for three more of the RBPs, including a partial Ferredoxin-like fold at the N-terminal of Int8 and a PABP domain-like fold in Int10.

We next looked to see if there were any additional proteins represented in the likely-RBD folds that were not already annotated as being RBPs by the census. We found 6,249 such proteins, which overlapped substantially with a recently published set of

6,657 novel RBP predictions by RBPPred (1,981 overlapping genes not previously annotated as RBPs)[23]. The ~2,000 concordant predictions by these two orthogonal methods more than double the number of previous RBP annotations [21]. We note that for many of our RBP predictions, we cannot confidently predict their RBP status based on fold alone because some of the likely-RBD folds have other functions besides RNA-binding (e.g. some superfamilies of the Ferredoxin-like fold can be protein binding instead of RNA binding), which may explain some of the non-overlapping predictions between our method and RBPPred. Nonetheless, several of the likely-RBD folds appear to be highly enriched in known RNA-binding domains, suggesting that functional annotation transfer is possible for these folds. For example, of the 32 domains predicted by our method to have the KH-domain fold, only four did not have a hit to the RNA-binding Pfam list, and of these, three were already known to be KH-domain RBPs based on the RBP census. The one domain that was not in the census was part of the Blom7 protein (also called KIAA0907), which has an experimentally determined structure (PDB: 2YQR) that confirms structural similarity to the KH-domain, despite the lack of a Pfam match. A full list of our new RBP predictions and likely-RBD folds is available on our website (see “Data and Code Availability” in the Methods).

Novel folds in the human proteome

Each year at least a few new folds are added to SCOPe (e.g. 13 new folds were added in the latest release). As noted above, there were ~14,000 human protein domains, or ~40% of domains, that were not assigned to known folds. While some of these might be due to problems of segmentation, we hypothesize many of them represent uncharacterized folds. As a preliminary analysis of potential novel folds in the human proteome, we extracted a set of human domains that were not close to any of our training examples (NN distance ≥ 30) and clustered them (Methods). This resulted in 36 clusters (Fig. 3-4A), which we examined for evidence of novel folds.

We first looked for incorrect domain boundary prediction or errors of our prediction method. Many of the domains were unusually long (>500 residues) compared to the average domain in the training set (195 residues), suggesting that they may in fact be multiple domains. For example, there were four neighboring clusters that contained almost exclusively domains from the Cadherin family of proteins. Most of these domains were longer than 500 residues and overlapped multiple repeats of the Cadherin motif based on Pfam annotations. The Cadherin fold is modeled as a single repeat in SCOPe, so this is likely a case where fold classification failed due to improper domain definition. A similar problem was observed for six clusters containing domains from several different classes of ATP/GTP binding proteins, where each domain spanned multiple distinct Pfam annotations that are likely to represent separate folds. Overall, we found that 26 of the clusters were potentially the result of such segmentation errors.

The largest cluster contained 208 domains, most of which were of a reasonable length (289 residues on average). On closer examination, we found that a large fraction of these domains were predicted to have a coiled coil structure. The SCOPe hierarchy places most coiled coil domains in a separate class (class H) that was not included in the training data. Therefore, this cluster can possibly be explained by the absence of the correct fold within our training data, although it is not truly novel. Eight other neighboring clusters were also found to have predominantly coiled coil structure, indicating that these structures can potentially explain a substantial fraction of our unclassified domains.

We also examined the un-clustered domains, which might be isolated examples of novel folds. One domain, the fourth predicted domain of the protein Limbin (residues 775-1067), was found not to overlap any known Pfam, SCOP, or other structural annotation. Although this domain was located in the feature space in proximity to the coiled coil clusters (Fig. 3-4A), it is predicted to be only partially coiled coil (Fig. 3-4B). We performed a more thorough template search for this domain using HHPred [24], RaptorX [25], and SPARKS-X [26] webservers, but did not identify a significant template match. We therefore used the Robetta webserver [27] to create an *de novo* model for this domain, which shows a mostly alpha helix structure (Fig. 3-4C). Limbin is the protein product of the gene *EVC2*, which is involved in the hedgehog signaling pathway and is frequently mutated in Ellis-van Creveld syndrome [28,29]. Interestingly, one of the mutations linked to this disease is found within our domain of interest (Arg870Trp; rs137852928) [28], suggesting that this region is functionally important. Whether this region represents a truly new fold will require additional analysis, but overall these results support the idea that the PESS can be used to identify novel structure groups.

3.2.4 Finding missing hedgehog proteins in *C. elegans*

The Hedgehog (Hh) signaling pathway plays an essential role in embryo development, cell proliferation, and tissue patterning in vertebrates and many invertebrates, including *Drosophila* [30]. Although many Hh-related genes have homologs in *C. elegans*, several key components of the pathway appear to be missing, including Smoothened (smo), Fused (fu), Suppressor of fused (Su(fu)), Cos2 (cos), and Hh itself. We asked whether we might be able to identify distant homologs to these missing genes using structural similarity search with the PESS.

To perform a proteome-scale structural similarity search, we first obtained all proteins in the *C. elegans* proteome, split them into domains, and mapped them to the PESS (see Methods). Next we obtained the sequences of the missing Hh-related genes from *Drosophila*, manually split them into their known functional domains, and mapped these to PESS as well. For each Hh-related protein, we used its domains as "queries" to obtain the closest 500 *C. elegans* domains within the PESS, which should represent the most structurally similar sequences in the *C. elegans* proteome. We then filtered the domain lists for each query protein to identify any *C. elegans* proteins that appeared on all (or most) of the lists—that is, proteins that have structural similarity to all (or most) of the domains of the query.

The closest matches for each of the Hh-related proteins are shown in Table 3-2. We found at least one potential structural match for each of the five query proteins. There are several promising results; for example, several serpentine receptors were found for Smoothened that also have similarity to its N-terminal domain, and several kinesin-like proteins were found for Cos2 that also have distant similarity to its interaction domains. More work will be needed to verify whether these proteins function in the Hh pathway. These results demonstrate an alternative use of the PESS as a direct method for structural querying of whole proteomes, independent of the framework of SCOPe folds used for classification in the previous sections.

3.3 Discussion

Here we have demonstrated the utility of an empirically derived structural feature space composed of threading scores (the PESS) for addressing the problem of fold recognition. The most important characteristics of such a multi-dimensional feature space are the ability to combine characteristics of multiple fold templates for fold recognition and the ability to potentially identify entirely novel folds through interpolation of the feature space. Many types of classifiers can be used in conjunction with this feature space; we showed here that linear SVM achieved good performance on benchmarks where at least 10 training examples were available per fold, and 1NN worked well in the more general case to recognize all known folds. We applied our method to the human proteome, predicted high confidence fold classifications for 20,340 domains, and showed that these predictions can be used to make functional inferences as illustrated by the class of RNA-binding proteins. A distinct advantage of the PESS is that it only requires a single training example per fold when used in conjunction with a 1NN classifier, allowing us to make predictions for all currently known folds in SCOPe. This is critical, since almost half of all SCOPe folds have only one training example in SCOP-20.

Another advantage of the 1NN classifier is that adding new training data does not require re-training the whole classifier, making it simple to update the model as new data become available.

One of the limitations of methods that rely on threading is the large amount of time the threading process takes. Threading against all PDB templates can take hours or even days per domain, depending on the computational resources available. In our method, we save time by only threading against representative templates. Nonetheless, threading is still the major time bottleneck, with a single average-sized (200 residue) domain taking 26 ± 2.5 minutes to thread against the 1,814 templates on one CPU core. To make this more feasible for genome-sized datasets, which typically have thousands or tens of thousands of domains, we have implemented an option for parallel processing of the input sequences. Another possible way to decrease the threading time would be to reduce the number of templates in our library. Preliminary results indicate that, depending on the classifier used, the feature space can be substantially reduced with only a minor impact on classification accuracy. In fact, given our framework, we hypothesize that we can create feature spaces at different scales such that threading can be applied in a hierarchical sequence.

The relationship between the structure of macromolecules to their function is a key annotation principle for computational inference. As the number of solved examples increase, we hypothesize that data-driven feature extraction coupled with machine learning methods as in our method and also in methods like deep learning [31], will have high utility in extending whole genome/proteome annotations.

3.4 Methods

Feature extraction and classification

Features were created for each input sequence by threading the sequence against a library of 1,814 structure templates to produce a vector of 1,814 threading scores. These scores represent the compatibility of the sequence with each template structure. Each score is directly used as a numerical coordinate within the feature space, which we call the Protein Empirical Structure Space (PESS). Threading was done using CNFalign_lite from the RaptorX package v.1.62 [32,33]. This program outputs a raw threading score for each query-template pair that is calculated from the optimal alignment of the query sequence and the template [32,33]. The template library was the default library provided by RaptorX. These 1,814 templates represent a wide range of different structures with low redundancy, but do not necessarily represent all known folds.

Training sequences were threaded against the templates and the resulting scores were normalized by z-standardization. Test sequences were threaded and normalized using the normalization parameters derived from the training sequences.

We constructed fold predictors over the PESS using both a first Nearest Neighbor (1NN) classifier and Support Vector Machine (SVM) classifier. For the 1NN classifier, pairwise Euclidean distances between each training and testing sequence were calculated, and each test sequence was classified into a fold by finding the closest training neighbor and transferring its fold label to the test sequence. For the support vector machine (SVM) classifier, a linear SVM was trained using the one-vs-all multiclass approach with the C parameter (which controls the penalization of misclassification during training) set to 1/N, where N is the number of positive examples in a given fold.

We also constructed a joint SVM+1NN classifier to assist in identification of fold classes with very small number of training examples. First, a linear SVM was trained as described above to recognize only folds that had at least 20 training examples ("large folds"). The remaining sequences in the training set ("small folds") were combined into a single class labeled "other", and this class was not used for classification. A separate 1NN classifier was trained on only the small fold training examples. Classification was then done in two phases: first, all test examples were provided to the SVM, and any test example that received a positive confidence score (based on the signed distance from the hyperplane) was classified into whichever fold gave the highest confidence score; second, the examples that were not classified in the first step were passed to the 1NN model for classification.

All classifiers were implemented in Python using the scikit-learn package [34].

Performance assessment

Prediction accuracy was calculated as the fraction of test examples that were classified into the correct fold. Precision (the number of true positives divided by the sum of the true and false positives) and recall (the number of true positive divided by the sum of the true positives and false negatives) were calculated separately for each fold and averaged across the folds. For both precision and recall, we excluded folds where the denominator was zero for the SCOP benchmark (611 folds excluded for recall calculation; 618 folds excluded for precision calculation).

Benchmark comparison to other methods

We obtained three benchmark datasets (EDD, F94, and F195) from the TAXFOLD paper [12]. Each benchmark contains only domain sequences longer than 30 residues with less than 40% pairwise identity, but each contains a different number of folds: EDD contains 3397 sequences in 27 folds, F95 contains 6364 sequences in 95 folds, and F194 contains 8026 sequences in 194 folds. Performance on each dataset was assessed using 10-fold cross validation, with SVM and 1NN classifiers trained and assessed as described above. We compared our results to the percent accuracies reported in recent publications that used these benchmarks with 10-fold cross validation. Some of these publications used modified versions of the benchmarks. Dehzangi *et al*., Saini *et al*., and Lyons *et al*. all used a version of EDD that had the same 27 folds, but 21 extra domains [15,16,18]. This is only a small fraction of the total number of domains in this dataset, so we do not expect this to have a major impact on the results. A more major modification was made by Wei *et al*., who used the same folds for EDD, F95, and F194, but updated the datasets to have 228, 427, and 499 extra domains, respectively [19]. Based on these numbers of added sequences, we estimate that the maximum performance of Wei *et al*. on the original TAXFOLD datasets would be no more than 98.8%, 89.2%, and 83.1%, respectively. However, since their new dataset still used the same cutoff for pairwise similarity as the original (<40%), it is more likely that their results would be roughly the same for both datasets. Thus the results in Table 3-1 should be comparable.

SCOP datasets and final classifier

We downloaded domains from the SCOPe database v2.06 pre-filtered to less than 20% pairwise identity by the Astral database (http://scop.berkeley.edu/astral/ver=2.06), which contained 7,659 domains covering all 1,221 folds in SCOP classes “a” through “g”. We call this dataset “SCOP-20”. We also downloaded the set pre-filtered to 40% identity and removed any domains that were also present in SCOP-20, resulting in 6,322 sequences in 609 folds. We call this dataset “SCOP-40”. We note that almost all SCOP-20 sequences were in SCOP-40 before this filtering, so the final test set has <40% pairwise identity with the training set. We trained a 1NN classifier as described above using the SCOP-20 dataset as training examples and tested the prediction performance using the SCOP-40 set. This classifier was used for all further fold recognition tasks, including the human proteome dataset.

We created the training and test sets for the <25% identity test as follows. We downloaded SCOPe pre-filtered to 25% pairwise identity from Astral, and then identified the overlapping sequences with SCOP-20. These sequences were used for training (7327 sequences). For sequences that did not overlap with SCOP-20, we used any that overlapped with SCOP-40 as the test set (1124). This ensured that no test example had more than 25% identity with a training example.

To remove redundancy between the SCOP-40 test examples and the 1,814 feature templates, we first obtained the original sequences used to generate the templates, which is included in the template file. We then performed a blastp search of the template sequences using all the SCOP-40 sequences as queries, and removed any SCOP-40 examples that had more than 25% identity over at least 90% of their length with one of the template sequences.

Human protein analysis

Protein domain sequences for 94 species from the Proteome Folding Project [5] were downloaded from the Yeast Resource Center public data repository (http://www.yeastrc.org/pdr/pages/download.jsp). To obtain only human sequences, we filtered for protein identifiers marked as “NCBI NR” and had “[Homo sapiens]” in the description. There were a total of 34,330 human domains with length greater than 30 residues, corresponding to 15,619 human proteins.

We classified the domains using the SCOP-20-trained 1NN model with an additional distance threshold to filter out domains that do not belong in any of the represented folds. We determined the threshold nearest-neighbor distance for classification as follows: for each test sequence in SCOP-40, we calculated the nearest neighbor distance before and after removing all SCOP-20 training sequences that belonged to the same fold as the test sequence. We found that a distance threshold of 17.5 provided a good balance between false positives and false negatives (FPR = 9.27%, FNR

= 9.49%). After classification with 1NN, only the domains with a nearest-neighbor distance below this threshold we considered confident fold predictions.

Human domain sequences were mapped to PDB entries using a blastp search of PDB requiring that at least 75% of the sequence length had at least 90% identity with a PDB sequence to consider it a match. PDB matches were then mapped to SCOPe classifications using the dir.cla.scope.txt (v.2.06) annotation file downloaded from the SCOPe website.

RNA-binding proteins

A list of 1,541 known human RBPs was obtained from a recent review [21]. Gene names of the RBPs were matched up to the human protein GIs using the UniProt ID mapping tool, and 1,093 of the RBPs were matched to one or more domains (3,263 domains total). This review also defined a list of 799 Pfam domains with functions related to RNA binding, which we used to filter the 3,263 RBP domains down to those that were most likely to be RNA-binding. Domains were assigned PfamA annotations using hmmscan (http://hmmer.org/). Both a "full-sequence" E ≤ 0.01 and a "best 1" E ≤ 0.1 was required for assignment. We compared our novel RBP predictions with the novel predictions from the RBPPred paper [23] on the gene level by mapping UniProt IDs to gene names for each list using the ID conversion tool on the UniProt website. Not all UniProt IDs could be mapped to a gene name. The final unique gene lists contained 6,589 genes for RBPPred and 5,668 genes for our method, which we used to compute the overlap.

Novel folds

We extracted all human domains with a nearest neighbor distance ≥30 and performed t-SNE on the PESS projections of these domains using scikit-learn with parameters “perplexity = 10, init = ‘pca’, random_state=123”. Domains were then clustered using DBSCAN from scikit-learn with parameters “eps = 5, min_samples = 5”. Domains and clusters were manually examined for potential boundary prediction errors or previous structural annotations.

C. elegans Hedgehog gene analysis

We downloaded the canonical protein sequences for the *Caenorhabditis elegans* proteome from UniProt. Each protein was split into domains based on DomainFinder Gene3D predictions [[REF]]. If there were regions between, before, or after predicted domains that were longer than 30 aa but did not have a Gene3D prediction, we also included those. If a “filled in” region such as this was longer than 450 aa, we used a sliding window of 300 aa (slide = 150 aa) to break it into smaller pieces. The fold of each domain was predicted using the methods described above. Known Hh-related protein sequences from *Drosophila melanogaster* were downloaded from UniProt, manually split into domains based on literature annotations of functional domains, and mapped to the PESS as above.

Data and Code Availability

Benchmark datasets, training data, and all human fold and RBP predictions are available at http://kim.bio.upenn.edu/software/pess.shtml. The fold classification source code is freely available at the same website or at https://github.com/sarahmid/PESS.

Author Contributions

S.A.M. and J.K. conceived the study and wrote the manuscript. S.A.M. implemented the feature space and classifier, applied it to the human proteome, and interpreted results. J.I. contributed to classifier development and validation.

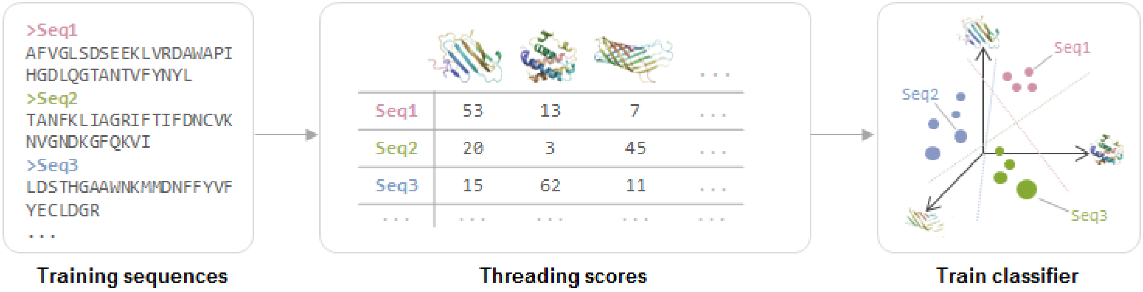

```
>Seq1
AFVGLSDSEEKLVRDAWAPI
HGDLQGTANTVFYNYL
>Seq2
TANFKLIAGRIFTIFDNCVK
NVGNDKGFQKVI
>Seq3
LDSTHGAAWNKMMDNFFYVF
YECLDGR
...
```

				...
Seq1	53	13	7	...
Seq2	20	3	45	...
Seq3	15	62	11	...
...	...	...	...	...

Figure 3-1. Overview of PESS construction.

Training sequences of known fold are threaded against a set of structure templates, and the resulting threading scores act as coordinates within a structural feature space (the PESS). A classifier can then be trained to recognize the subspace occupied by each fold in the PESS. Different colors indicate the fold of each sequence and are shown here only for visualization.

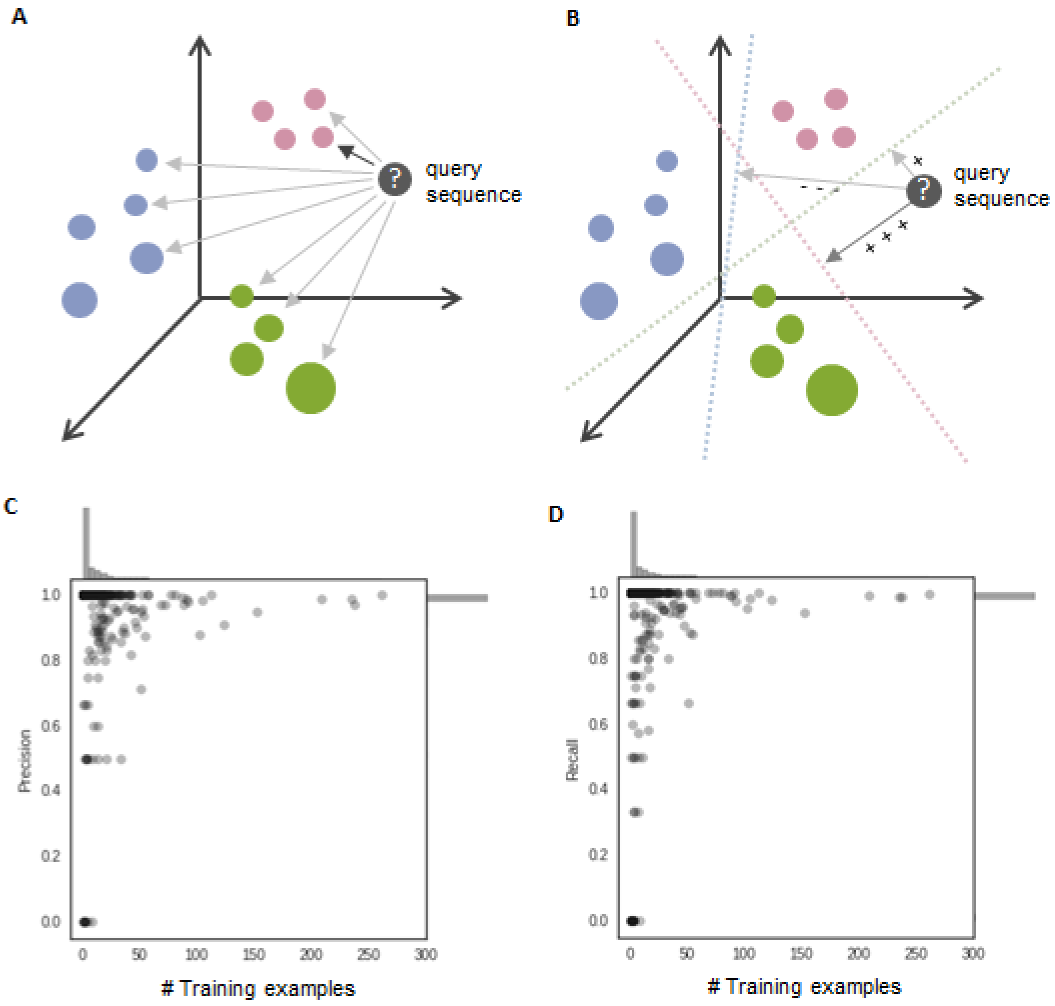

Figure 3-2. Classification and performance using the PESS.

(A&B) Two different methods of classification using the PESS. Colored circles represent training examples within the PESS and are colored by fold. (A) In 1NN classification, the PESS distance between the query (gray circle) and all training examples is computed and the query is assigned to the fold of the nearest training example (dark gray arrow). (B) In 1-vs-all SVM classification, the PESS distance between the query and each of the fold-level hyperplanes (dotted lines) is computed, and the query is assigned to the fold that gives the best score (dark gray arrow), based on signed distance from the fold’s hyperplane. (C) Precision and (D) recall measures were computed for each fold separately after 1NN classification using the PESS and plotted against the number of training examples for each fold. Marginal histograms show the distribution of folds along each axis.

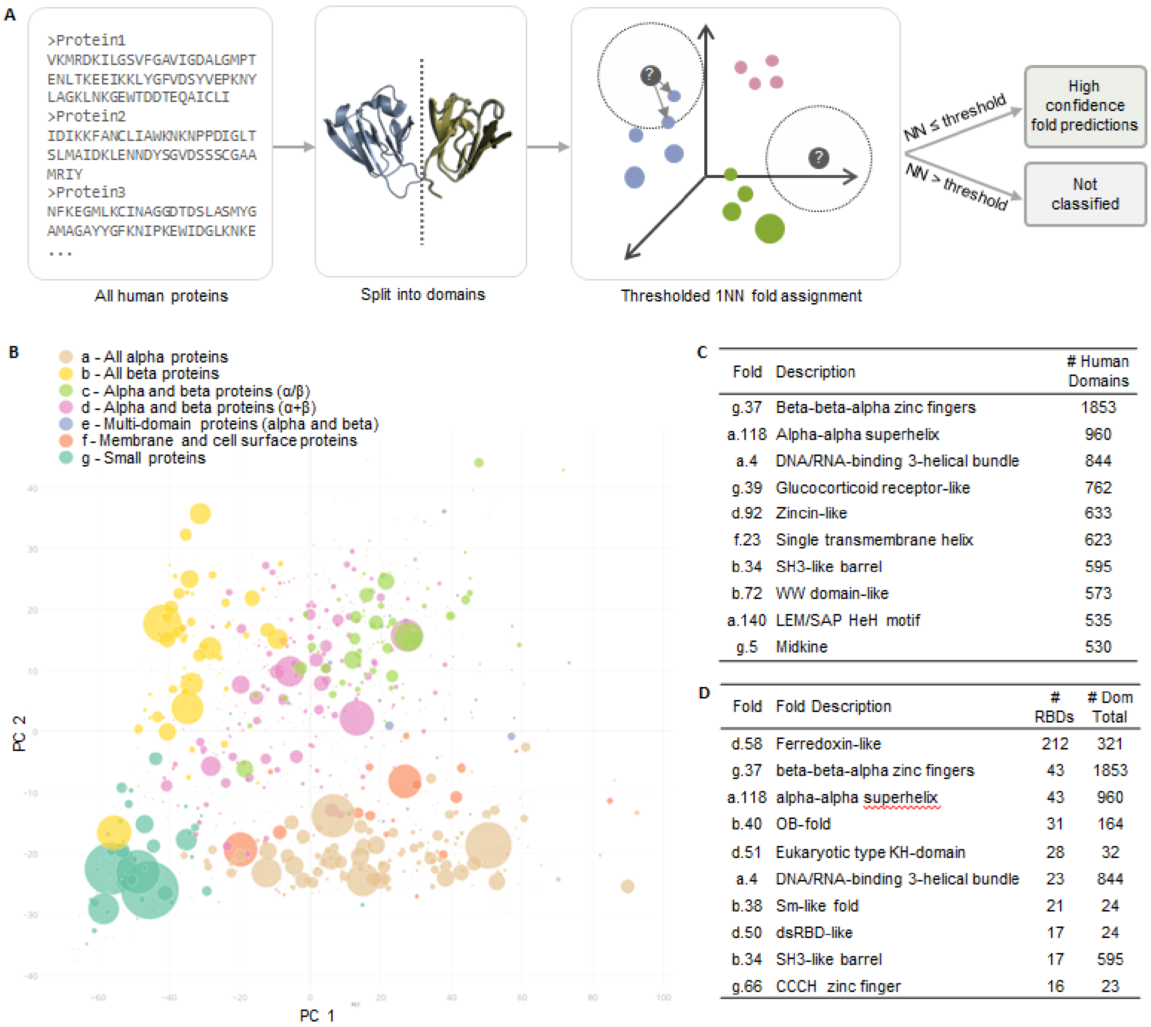

C

Fold	Description	# Human Domains
g.37	Beta-beta-alpha zinc fingers	1853
a.118	Alpha-alpha superhelix	960
a.4	DNA/RNA-binding 3-helical bundle	844
g.39	Glucocorticoid receptor-like	762
d.92	Zincin-like	633
f.23	Single transmembrane helix	623
b.34	SH3-like barrel	595
b.72	WW domain-like	573
a.140	LEM/SAP HeH motif	535
g.5	Midkine	530

D

Fold	Fold Description	# RBDs	# Dom Total
d.58	Ferredoxin-like	212	321
g.37	beta-beta-alpha zinc fingers	43	1853
a.118	alpha-alpha superhelix	43	960
b.40	OB-fold	31	164
d.51	Eukaryotic type KH-domain	28	32
a.4	DNA/RNA-binding 3-helical bundle	23	844
b.38	Sm-like fold	21	24
d.50	dsRBD-like	17	24
b.34	SH3-like barrel	17	595
g.66	CCCH zinc finger	16	23

Figure 3-3. Fold classification of the human proteome.

(A) Overview of classification process. Full length human protein sequences were split at predicted domain boundaries to create one or more separate domain sequences per protein (Drew et al. 2011). Domain sequences were mapped to the PESS and classified by 1NN classification. A threshold was applied to the nearest neighbor distance (dotted circle), whereby only domains with a nearest neighbor closer than the threshold distance were classified. (B) PCA projection of fold centroids within the PESS, scaled by number of human domains predicted to belong to that fold. Centroids were calculated based on the location of each fold’s training examples within the PESS and are colored by SCOP class. (C) Top ten folds by number of human domain predictions. (D) Top ten likely RNA-binding folds, ranked by number of confirmed RNA-binding domains (RBDs). Confirmed RBDs were determined based on matches to a curated list of RNA-binding related Pfam families.

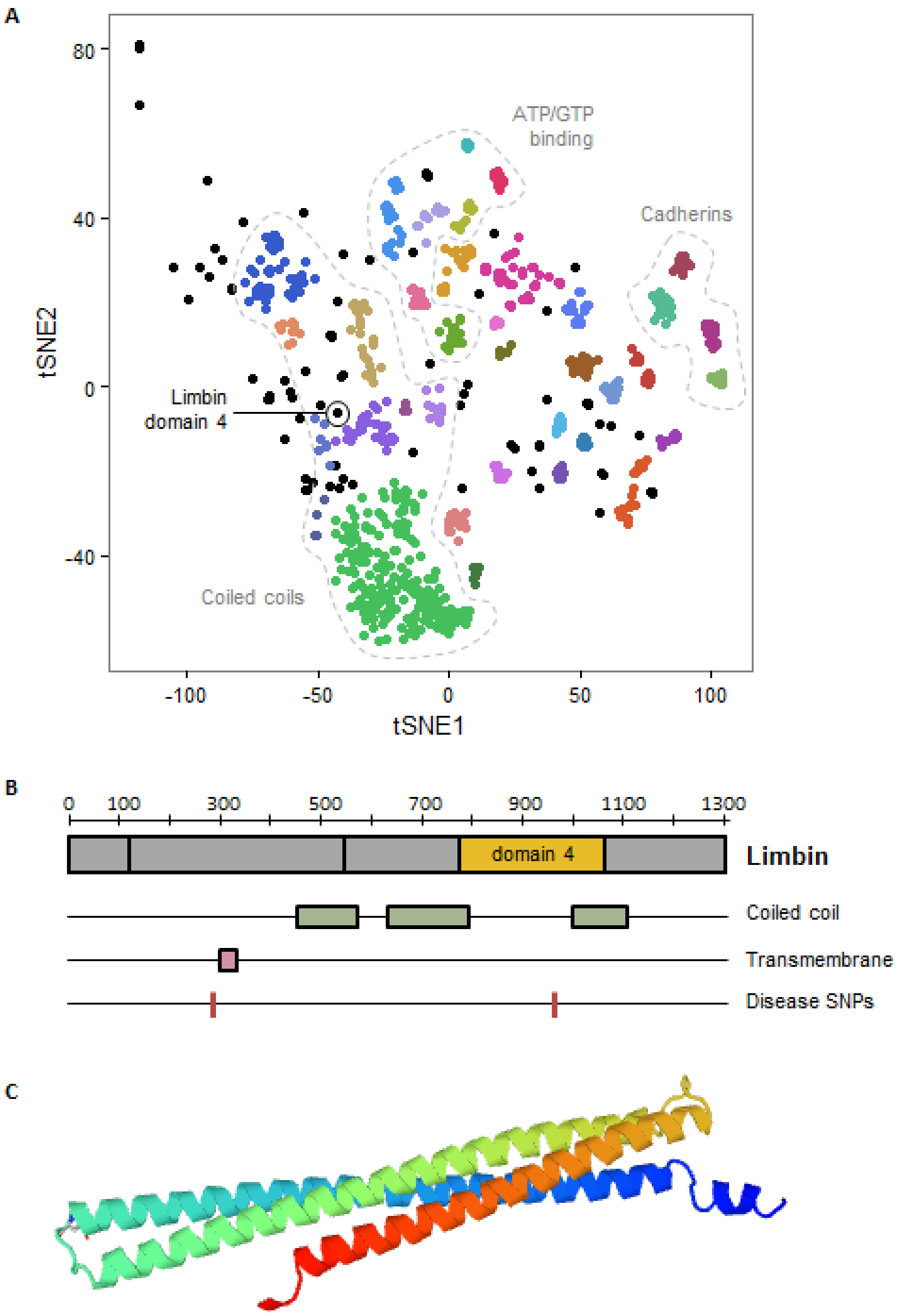

Figure 3-4. Analysis of unclassified human domains.

(A) t-SNE projection of human domains with nearest-neighbor distance ≥ 30. Colors indicate cluster assignment by DBSCAN; unclustered domains are shown in black. Dotted lines show related groups of domains. (B) Overview of the *EVC2* protein product, Limbin, and its known structure elements. The location of the domain with a putative novel fold is shown in yellow. (C) *De novo* structure model for part of the Limbin domain 4 creating using Robetta.

Table 3-1. Overall % accuracy on three benchmarks using 10-fold cross validation.

Method	**EDD**	**F95**	**F194**
Dehzangi *et al.*[a]	88.2	-	-
Saini *et al.*[a]	86.6	-	-
Lyons *et al.*[a]	93.8	-	-
Zakeri *et al.*	88.8 / 96.9[b]	-	-
Yang and Chen	90.0	82.4	79.6
Wei *et al.*[c]	92.6	83.6	78.2
This method – 1NN	90.6	84.6	82.5
This method - SVM	95.7	91.9	90.5

[a] Using a slightly modified EDD set with 21 additional domains (3418 total) (see Methods)

[b] With Interpro functional annotations

[c] Using modified versions of EDD (3625 domains), F95 (6791 domains), and F194 (8525) (see Methods)

Table 3-2. Putative structural matches to missing *C. elegans* Hh-related genes.

Protein	**Domains required to match**	**Closest *C. elegans* matches**
Hedgehog	N-terminal domain (hedge), C-terminal domain (hog)	trpp-8, CELE_T28F3.5, fbxa-142, spt-5, tns-1, C41A3.1, lin-18, nmr-1, CELE_T21C9.6, CELE_F54B3.1, prx-1, sup-17, mtm-6, CELE_F46G10.2, C05D12.3, eef-2, CELE_F57C7.4
Smoothened	N-terminal domain, Frizzled domain, GPCR-like domain	npr-30, srh-173, srw-139, tyra-3, srw-48, srw-124, fshr-1
Fused	Kinase domain, Central domain, Leucine-rich-repeat domain	chs-2
Suppressor of fused	Suppressor of fused-like, Suppressor of fused C-terminal	C41A3.1, plc-1, cec-9, CELE_F27C8.2, aph-2, age-1, CELE_T23E1.1, CELE_F59H6.5, glf-1, CELE_T08A11.1, ddo-3, gcy-25, rde-1, ntp-1, B0511.12, F52H2.6, CELE_Y61A9LA.10, let-19, drsh-1, ZK1067.4, CELE_W03A5.1, CELE_Y16E11A.2, CELE_F22E5.6, CELE_Y43F8B.19, CELE_Y7A5A.1, CELE_T05H10.1
Cos2	Kinesin-like domain, fu-binding domain, smo-binding domain	unc-116, klp-18, klp-20, zen-4, klp-12, arc-1

3.5 References

1 Koonin, E. V *et al.* (2002) The structure of the protein universe and genome evolution. *Nature* 420, 218–223

2 Fox, N.K. *et al.* (2014) SCOPe: Structural Classification of Proteins—extended, integrating SCOP and ASTRAL data and classification of new structures. *Nucleic Acids Res.* 42, D304–D309

3 Kim, S.H. *et al.* (2005) Structural genomics of minimal organisms and protein fold space. *J. Struct. Funct. Genomics* 6, 63–70

4 Malmström, L. *et al.* (2007) Superfamily assignments for the yeast proteome through integration of structure prediction with the gene ontology. *PLoS Biol.* 5, 758–768

5 Drew, K. *et al.* (2011) The Proteome Folding Project: Proteome-scale prediction of structure and function. *Genome Res.* 21, 1981–1994

6 Hildebrand, A. *et al.* (2009) Fast and accurate automatic structure prediction with HHpred. *Proteins Struct. Funct. Bioinforma.* 77, 128–132

7 Huang, Y.J. *et al.* (2014) Assessment of template-based protein structure predictions in CASP10. *Proteins Struct. Funct. Bioinforma.* 82, 43–56

8 Roy, A. *et al.* (2010) I-TASSER: a unified platform for automated protein structure and function prediction. *Nat. Protoc.* 5, 725–38

9 Cheng, J. and Baldi, P. (2006) A machine learning information retrieval approach to protein fold recognition. *Bioinformatics* 22, 1456–1463

10 Jo, T. *et al.* (2015) Improving Protein Fold Recognition by Deep Learning Networks. *Sci. Rep.* 5, 17573

11 Dubchak, I. *et al.* (1999) Recognition of a protein fold in the context of the SCOP classification. *Proteins Struct. Funct. Genet.* 35, 401–407

12 Yang, J.-Y. and Chen, X. (2011) Improving taxonomy-based protein fold recognition by using global and local features. *Proteins* 79, 2053–64

13 Scholkopf, B. and Mika, S. (1999) Input space versus feature space in kernel-based methods. *IEEE Trans. Neural Netw.* 10, 1000–1017

14 Middleton, S.A. and Kim, J. (2014) NoFold: RNA structure clustering without

folding or alignment. *RNA* 20, 1671–1683

15 Dehzangi, A. *et al.* (2014) A segmentation-based method to extract structural and evolutionary features for protein fold recognition. *IEEE/ACM Trans. Comput. Biol. Bioinforma.* 11, 510–519

16 Saini, H. *et al.* (2015) Probabilistic expression of spatially varied amino acid dimers into general form of Chouʼs pseudo amino acid composition for protein fold recognition. *J. Theor. Biol.* 380, 291–298

17 Zakeri, P. *et al.* (2014) Protein fold recognition using geometric kernel data fusion. *Bioinformatics* 30, 1850–1857

18 Lyons, J. *et al.* (2015) Advancing the Accuracy of Protein Fold Recognition by Utilizing Profiles from Hidden Markov Models. *IEEE Trans. Nanobioscience* 14, 761–772

19 Wei, L. *et al.* (2015) Enhanced Protein Fold Prediction Method Through a Novel Feature Extraction Technique. *IEEE Trans. Nanobioscience* 14, 649–659

20 Orengo, C.A. *et al.* (1994) Protein superfamilles and domain superfolds. *Nature* 372, 631–634

21 Gerstberger, S. *et al.* (2014) A census of human RNA-binding proteins. *Nat. Rev. Genet.* 15, 829–845

22 Tanaka, M. *et al.* (2009) A novel RNA-binding protein, Ossa/C9orf10, regulates activity of Src kinases to protect cells from oxidative stress-induced apoptosis. *Mol. Cell. Biol.* 29, 402–413

23 Zhang, X. and Liu, S. (2017) RBPPred: predicting RNA-binding proteins from sequence using SVM. *Bioinformatics* btw730,

24 Soding, J. *et al.* (2005) The HHpred interactive server for protein homology detection and structure prediction. *Nucleic Acids Res.* 33, W244–W248

25 Källberg, M. *et al.* (2012) Template-based protein structure modeling using the RaptorX web server. *Nat. Protoc.* 7, 1511–1522

26 Yang, Y. *et al.* (2011) Improving protein fold recognition and template-based modeling by employing probabilistic-based matching between predicted one-dimensional structural properties of query and corresponding native properties of templates. *Bioinformatics* 27, 2076–2082

27 Bradley, P. *et al.* (2005) Toward High-Resolution de Novo Structure Prediction for Small Proteins. *Science (80-.).* 309, 1868–1871

28 Galdzicka, M. *et al.* (2002) A new gene, EVC2, is mutated in Ellis–van Creveld syndrome. *Mol. Genet. Metab.* 77, 291–295

29 D'Asdia, M.C. *et al.* (2013) Novel and recurrent EVC and EVC2 mutations in Ellis-van Creveld syndrome and Weyers acrofacial dyostosis. *Eur. J. Med. Genet.* 56, 80–87

30 Varjosalo, M. and Taipale, J. (2008) Hedgehog: Functions and mechanisms. *Genes Dev.* 22, 2454–2472

31 LeCun, Y. *et al.* (2015) Deep learning. *Nature* 521, 436–444

32 Ma, J. *et al.* (2012) A conditional neural fields model for protein threading. *Bioinformatics* 28, i59–i66

33 Ma, J. *et al.* (2013) Protein threading using context-specific alignment potential. *Bioinformatics* 29, i257-65

34 Pedregosa, F. *et al.* (2011) Scikit-learn: Machine Learning in Python. *J. Mach. Learn. Res.* 12, 2825–2830

Chapter 4: Structures and plasticity: analysis of dendritically targeted RNAs and the "local proteome"

4.1 Introduction

Neurons require local protein synthesis within the dendrites to produce long-lasting synaptic potentiation [1] (see also section 1.3.3 of this thesis). Importantly, in order for this local synthesis to occur, mRNAs must first be transported to the dendrites. Although RNA localization and local translation have been studied for over 20 years, there are still many aspects of these processes that remain unclear. In this chapter, I will address three open questions, outlined below, with a particular focus on the under-studied roles of RNA secondary structure and protein tertiary structure.

Which RNAs are dendritically localized?

Multiple studies have profiled RNAs that are localized to the dendrites using various methods [2–10]. Despite these efforts, there is still no firm consensus on the set of dendritically localized RNAs. Most recently, three studies used high-throughput RNA sequencing (RNA-seq) to identify dendritically-enriched RNAs in rodent neurons. First, Cajigas *et al*. performed bulk RNA-seq on the neuropil (dendrite-rich) region of rat CA1 hippocampal slices and predicted 2,550 dendritic RNAs [7]. Second, Ainsley *et al*. used epitope-tagged ribosomes that were expressed specifically in neurons (but not other brain cell types) to purify ribosome-bound RNA from mouse CA1 neuropil punches, predicting 1,890 dendritic RNAs [8]. Most recently, Taliaferro *et al*. used a culture system where cells were grown on a porous membrane that allows processes to pass through, but not cell bodies, thus allowing them to collect and sequence processes with relative purity (similar to [5]) [10]. This allowed them to identify 778 dendritic RNAs (and more with isoform-specific localization). Although in theory RNA-seq studies such as these should produce a comprehensive picture of the dendritic transcriptome, each of these studies had experimental limitations that complicate the interpretation of the results. The Cajigas study was limited by the presence of non-neuronal and non-dendritic material in the neuropil, such as glia and interneurons, which make it difficult to pinpoint which RNAs came from neuronal dendrites. In addition, due to the filtering steps the authors used to remove suspected contaminating RNAs (including known nuclear-related genes), many true dendritic RNAs may have been removed. The Ainsley study, which was also performed with tissue slices, alleviated some of these concerns by increasing the specificity of the RNA capture for only neuronal dendrites. However, in gaining this specificity, Ainsley *et al*. may also have lost some sensitivity, since their method only captures ribosome-associated RNAs. Finally, the Taliaferro study—while free from concerns about tissue-related contamination—relied mostly on CAD and N2A cell lines for their results. Although these cell lines are derived from neurons and grow processes when induced to differentiate, their degree of divergence from primary neurons is unclear.

Due to these limitations, there is still ambiguity about which RNAs are present in the dendrites. Studies that are more specific in their capture of dendritic RNA are needed for primary cells. Although study of dendrites *in vivo* would be ideal (perhaps using spatially-precise capture techniques such as that described in [11] or large-scale fluorescent in situ hybridization (FISH)-based approaches [12–14]), even primary cultures would give valuable insight. Furthermore, since most studies have used bulk RNA sequencing of many cells at once, little is known about the variability of dendritic localization across single neurons. Given the heterogeneity already observed in neuronal RNA expression on the whole-cell level [15], it would not be surprising if there is variability of localization. In fact, very early studies have already demonstrated that individual dendrites of the same neuron can have different transcripts [2]. Further study of these questions is warranted.

How are RNAs recognized for localization?

If we take the RNA-seq studies described above at face value, then somewhere between 700 and 2,500 species of RNA are localized to the dendrites. Since the average neuron is estimated to express between 10,000 and 15,000 genes [11,15], it is clear that not all RNAs are localized. How then does the neuron perform this large scale sorting of RNAs that should and should not be dendritically targeted? Most evidence points to the following model: RNAs that are to be localized contain a *cis* motif—called a dendritic targeting element (DTE)—which is recognized by a specific RNA binding protein (RBP). The RBP then mediates association with the transport machinery of the cell and causes localization [16]. There are probably several different DTEs and localization-mediating RBPs. However, given that there are currently only ~1,500 known RBPs in humans [17], of which only a small fraction probably participate in localization, it seems unlikely that each dendritic RNA is localized by a unique combination of DTE and RBP. Instead, multiple RNAs probably share the same or very similar DTEs and are transported by the same RBP. If this is true, then it should be possible to identify DTEs computationally by looking for sequence elements that are shared among multiple localized RNAs, and relatively absent in non-localized RNAs. Surprisingly, however, very few DTEs have so far been found using this method. Most known DTEs were instead identified using trial-and-error experimental methods, and furthermore seem to be specific to just one or a small handful of localized RNAs.

Why have DTEs been so elusive thus far? Two possible explanations stand out. First, most studies have focused exclusively on searching canonical 3’UTRs. Although this is historically where most localization elements have been found, especially in non-neuronal contexts, there is growing evidence that other parts of the mRNA could be involved, such as cytoplasmically retained introns [18]. Recently, a study also identified over 2,000 previously unannotated distal 3’UTR isoforms, which were conserved between mouse and human and were mostly specific or upregulated in neuronal tissues [19]. It is unknown what role these alternative 3’ isoforms play in neurons, but an exciting possibility is that they contain localization signals. Thus far, these sequences have not been included in the search for DTEs. A second possible explanation for the lack of known DTEs is that previous studies have not taken secondary structure sufficiently into account. Many of the known DTEs have an important structural component or appear to be completely structural in nature, but due to a lack of efficient algorithms for *de novo* structural motif discovery, this has not yet been systematically explored. The combination of a more complete database of localized RNA isoforms with structure-aware motif finding has great promise for identifying missing localization signals.

What role do locally translated proteins play in long-term potentiation?

The presumed purpose of localizing so many RNAs to the dendrites—which requires energy expenditure on the part of the cell—is so that these RNAs can be locally translated in response to synaptic activation. A corollary of this is that the proteins produced during local translation (the "local proteome") should play an important role in the processes following synaptic activation, particularly those that lead to long-lasting synaptic plasticity. This is supported by studies showing that inhibiting protein synthesis in the dendrites blocks late-phase long term potentiation (L-LTP) [1], and has been shown more specifically to be true for a small handful of individual locally translated proteins, such as CaMKIIα [20].

So far, however, very little is actually known about the specific role of each locally translated protein. Gene ontology (GO) analysis can provide a useful overview of functions enriched in a group, but the annotation is sometimes vague or incomplete for individual proteins and can be susceptible to various biases [21]. As demonstrated in Chapter 3, protein structure prediction can help fill holes left by other types of annotation and lead to new functional insights. More specifically, there are several reasons to think that structure analysis might be particularly useful in the context of understanding the local proteome. Firstly, the post-synaptic density (PSD) and surrounding dendritic spine are highly structured formations that depend on a scaffold of interacting proteins for their function [22–24]. Central to these interactions are protein domains, which usually require a specific three-dimensional fold in order to function properly. Secondly, mutations linked to neuropsychiatric diseases have been found to be enriched in synaptic proteins in human and mouse, and several of these mutations appear to disrupt important structures [25,26]. A more complete picture of the structures of locally translated proteins will help both in functional understanding and mutation-impact analysis.

Chapter overview

In this chapter, I use a combination of experimental and computational techniques to shed new light on the three questions outlined above. To address the first question—which RNAs are localized to the dendrites?—I dissect individual neurons in primary culture to obtain somatic and dendritic subcellular compartments with high specificity. RNA-sequencing then allows for identification of poly-adenylated transcripts in each compartment. This sequencing is done on the single-cell level to enable direct comparison of the soma and dendrites from the same original cell, and allows for assessment of heterogeneity of RNA expression and localization across cells. I use this dataset to identify dendritically enriched RNAs on both the gene and isoform levels, including the recently identified set of neuron-enriched distal 3' UTR isoforms [19]. To address the second question—where are all the common DTEs?—I make use of this carefully defined set of localized sequences to perform a comprehensive search for RNA motifs that might be involved in localization. Using the method described in Chapter 2 for *de novo* identification of RNA structure motifs, I identify several secondary structures enriched in the localized sequences compared to non-localized background, including two SINE-derived motifs. Finally, to address the third question—what role do locally translated proteins play in LTP?—I expand on existing gene-level annotations using domain-level protein structure information. I use the method described in Chapter 3 to predict the structural folds of all potential locally-translated proteins (as predicted by the localization of the RNA) and highlight several new pieces of information the structure predictions provide, including links to disease. Altogether, these results provide new insights into RNA localization and locally translated proteins in neurons and demonstrate the utility of including structure information in functional analysis of macromolecules.

4.2 Results and Discussion

4.2.1 Gene-level localization

To compare the RNAs present in dendrites and somas of individual neurons, we manually separated the neurites (dendrites/axon) and soma of primary mouse hippocampal neurons using a micropipette and performed RNA-sequencing on each subcellular fraction such that we obtained neurite and soma transcriptome of the same cell (Fig. 4-1). We note that the axon is generally small at this culture stage (~5% the volume of the dendrites) and thus is not expected to make up a large fraction of the neurite samples. Somas generally contained a wider variety of transcripts than their corresponding neurites, with an average of 9,206 and 5,827 genes expressed in each compartment respectively (Fig. 4-2A). As expected, the neurite-expressed genes were largely a subset of the soma-expressed genes of the same cell (Fig. 4-2B). Genes that show expression only in the neurites may represent strongly localized RNAs, which we will investigate further below. All soma and neurite samples expressed housekeeping genes and neuronal marker genes at high levels, especially pyramidal markers, with little expression of other brain cell type markers (Fig. 4-3C).

To identify potentially localized RNAs, we used DESeq2 [27] to perform a differential expression analysis using a paired design, where soma and neurites of the same original cell were directly compared. DESeq2 reported 3,811 genes significantly more highly expressed in somas and 387 genes significantly higher in neurites (FDR corrected $p \leq 0.05$) (Fig. 4-3A). Given their relatively higher expression in neurites compared to soma, these 387 genes are likely to be actively localized, and we therefore refer to them as localized genes (Table 4-1). Fifty six of these localized genes overlapped with a curated set of previously annotated dendritic RNAs from tissue and FISH (see "'Known dendritic' gene list" in Methods) (Fig. 4-3B) ($p = 4.2e-15$; odds ratio = 3.8; Fisher's exact test). The localized RNAs were also strongly enriched for GO terms related to translation and mitochondria, consistent with previous reports [8–10], whereas the somatic RNAs were enriched for functions related to the nucleus, including RNA splicing and chromatin organization (Fig. 4-3C).

Differential expression analysis identifies genes that have a higher expression in one condition compared to another. However, in the case of RNA localization, we do not necessarily expect all localized RNAs to have higher expression in the neurites than the soma. This may be particularly important when expression is profiled on the single cell level, since factors such as bursting transcription and variable rates of localization can lead to high variability in the relative amounts of RNA in each compartment at the time of collection. Therefore, we additionally identified RNAs that were *consistently* present in the neurites across the profiled cells, since these RNAs are likely to have important neurite function even if they are not concentrated there relative to the soma. There were 1,863 RNAs observed in at least 90% of the neurite samples (Table 4-2). These RNAs overlapped substantially with the curated list of dendritic RNAs (Fig. 4-4A) (472 overlapping; p<2.2e-16; odds ratio=9.5; Fisher's exact test), and included well-characterized localizers such as *Actb, Bdnf, Calm1*, *Dlg4*, *Grin1*, and *Map2*. Theses RNAs also covered many of the same ontology functions as the gene-level localizer set, such as mitochondria and translation, but additionally were strongly enriched for a large number of synaptic and localization-related functions (Fig. 4-4B). Overall, these results suggest that on the single cell level, RNAs with important dendrite functions are often not localized to the point of having higher expression in the dendrites relative to the soma, but are nonetheless consistently present in the dendrites at a lower level.

4.2.2 Differential localization of 3'UTR isoforms

Neurons express a large number of distal 3'UTR isoforms that are conserved between human and mouse [19]. The purpose of these alternative 3'UTRs in neurons is not well understood, but one possibility is that they play a role in subcellular localization. Under this model, one of the alternative 3'UTR sequences contains a localization signal, causing only the transcript copies that contain that UTR to be localized. This could allow the neuron to control the extent of localization of certain genes using co-transcriptional mechanisms that modulate the ratio of 3’UTR isoforms produced, such as alternative splicing or alternative cleavage and polyadenylation. A few specific examples of differentially localized 3’UTR isoforms have already been characterized [28], such as Bdnf [29,30]. The Taliaferro *et al.* study, mentioned in the introduction to this chapter, surveyed this phenomenon on a larger scale in brain-derived cell lines and cortical neurons and identified hundreds of cases of differential localization of alternative 3'UTR isoforms [10]. However, almost all of the results reported in this study were based on the cell lines rather than the primary cortical neurons, and the list of differentially expressed isoforms in the primary neurons was not made available (only the cell line-based list was provided). Furthermore, although correlations between the cell lines for alternative 3’UTR usage was reasonable ($R_{Spearman}$ = 0.74), the correlation between the cell lines and the primary neurons was much lower ($R_{Spearman}$ = 0.35), suggesting that there may be substantial differences in isoform usage in primary neurons that is not reflected in the provided cell line results. Given the potential importance of alternative 3’UTR usage in dendritic localization, we sought to better define genes that have 3’-isoform-specific neurite localization in primary neurons and provide a more extensive analysis of the characteristics of these isoforms than previously described.

As a result of the single cell RNA amplification process, the majority of our sequencing reads map within 500nt of a 3' end (Fig. 4-5A), and we thus have high coverage of these regions for identifying expressed 3’UTR isoforms. As exemplified in Figure 4-5B, reads show a clear peak marking the 3’ ends of transcripts, allowing us to quantify 3’ isoforms separately as long as they are sufficiently distant. We quantified the expression of individual 3' isoforms based on the last 500nt of each isoform, merging any 3' ends that were closer than 500nt into a single feature. We first observed that individual cells widely expressed multiple 3' isoforms per gene, with somas showing slightly more alternative expression than neurites on average (1.26 and 1.13 expressed 3'UTR isoforms per gene, respectively). When multiple isoforms were expressed, one isoform tended to be dominant, making up ~85% of the gene reads on average in both compartments.

To compare differential isoform expression between soma and neurite, we limited the considered 3'UTR isoforms to only the top two most highly expressed isoforms per gene, which accounted for the vast majority of reads in most genes. The top two isoforms were labeled "proximal" (the more 5' isoform) or "distal" (the more 3' isoform), and isoform preference for each gene in each sample was summarized as the fraction of reads mapping to the distal isoform (distal reads divided by distal plus proximal reads), which we refer to as the distal fraction (DF). We focused our analysis only on multi-3'UTR genes that had at least 10 total reads in both the soma and neurites of at least five cells, which resulted in 3,638 considered genes. We note that alternative 3’UTRs can be generated by two distinct mechanisms: alternative splicing, which generates alternative last exons (ALEs), or alternative cleavage and polyadenylation, which generates tandem UTRs (Fig. 4-5C). Therefore, we split our set of multi-3'UTR genes into ALE and tandem groups based on the relationship between the designated proximal and distal 3'UTR for that gene. ALEs made up the majority of the considered multi-3'UTR genes (3,108 ALE versus 530 tandem).

To identify 3'UTR isoforms that are differentially localized in neurites, we looked for genes that had consistent patterns of isoform preference across our cells. That is, we looked for cases where the change in distal fraction (ΔDF; defined as $DF_{neurite} - DF_{soma}$ and calculated separately for each soma-neurite pair) was in a consistent direction (+/-) across many cells (Fig. 4-5D). Using a Wilcoxon signed-rank test ($p<0.1$), we identified 298 genes that met this criterion (Table 4-3). For clarity, we will refer to these 298 genes as the "*isoform-level localizers*", and refer to the other localized genes identified in the previous section as the "*gene-level localizers*" and the "*consistent neurite*" sets. Most of the isoform-level localizers were ALE genes (249 ALE, 49 tandem), but neither type was significantly enriched in this group. Unlike the gene-level localizers and consistent neurite sets, the isoform-level localizers were not significantly enriched for particular GO functional categories, but they did overlap substantially with the curated list of previously-observed dendritic RNAs (69 overlapping; $p<2.2e-16$; odds ratio=6.8; Fisher's exact test) (Fig. 4-5E). Only four of the isoform-level localizers overlapped with the gene-level localizers (*mt-Rnr2, Rpl31, Rpl21,* and *Map2*), indicating that gene-level and isoform-level localized genes are distinct sets. Approximately half of both the gene and isoform sets overlapped with the consistently localized set (Fig. 4-5F). The lack of overlap between the gene-level and isoform-level localizers might reflect differences in the methods used to identify the two sets—for example, it is possible for a gene to have highly different isoform ratios in the soma and neurites and yet still have similar total gene-level counts in both compartments; in such a case, gene-level analysis would be unlikely to identify this gene as differentially localized, but isoform-level analysis could detect it. There might also be biological reasons for the low overlap between these two sets. Localization on the gene versus the isoform level represents a choice between wholesale versus partial localization of the total transcript pool for a given gene. Since partial localization of only certain isoforms requires additional steps of regulation during splicing and cleavage and polyadenylation, it might be that this mechanism is only utilized for genes where such partial localization is highly advantageous to the cell, as would be the case for genes with important roles in both the soma and dendrites. The fact that the isoform-level localizers were not enriched for any GO terms suggests that the proteins that fall into this category are functionally diverse, but despite the lack of enrichment, many of the individual GO annotations for these genes reflect functions that are likely to be important for both the soma and the dendrites—e.g. “ATP binding”, “endoplasmic reticulum”, and “protein transport”. More work will need to be done to understand the mechanisms and purpose underlying isoform-level localization.

What are the characteristics of isoform preference in soma and neurites? First, we looked to see if the proximal or distal isoform was more likely to be localized to the neurites. For each gene, the neurite-preferred isoform was determined based on the average ΔDF across cells, which is positive when the neurites prefer the distal isoform and negative when they prefer the proximal isoform (as illustrated in Fig. 4-5D). Among the 298 pairs of differentially localized isoforms, neurites preferred the distal isoform in 64% of cases, which was independent of ALE/tandem status. This preference diverged significantly from expectation based on the full set of 3,638 multi-3'UTR genes, where neurites preferred the distal isoform in only 44% of cases (p=3.7e-13; odds ratio=2.4; Fisher's exact test). Next, we examined the cell-to-cell variability of isoform preferences, particularly focusing on the differences in DF variability between somas and neurites. For each gene, the variance of DF was calculated separately for soma and neurite samples. Among the 298 genes with differentially localized isoforms, neurites were more variable than soma in only 39.9% of cases. Again, this preference diverged significantly from expectation based on the full set of multi-3'UTR genes, where neurites were more variable than somas in 70.6% of cases (p<2.2e-16; odds ratio=3.6; Fisher's exact test). Figure 4-6 provides three representative examples of genes with these isoform patterns, showing the consistent preference for the distal isoform in the neurites compared to soma for multiple individual cells, and the lower variability of DF in the neurites compared to the somas.

Based on these findings, we hypothesized that the isoform-level localizers might predominantly belong to a particular regulatory pattern that we call "selective neurites" (Fig. 4-7). In this pattern, a given gene has multiple expressed 3'UTR isoforms, both of which are present in the soma at variable ratios (which may be influenced by factors such as the amounts of particular splicing, polyadenylation, or localization factors in the cell at the time of sampling, or how recently transcription of that gene last occurred). In the neurites, on the other hand, there is strong selection for only one of those isoforms, e.g. through preferential localization, which causes an enrichment of the favored isoform in the neurites in a consistent manner across cells. In support of this notion, we found that 47 of the isoform-level localizers showed the pattern just described, whereas only 18 showed the opposite pattern (where the soma is more selective). Furthermore, 39 of the 47 were cases where the distal isoform was the one selected for in neurites, making this by far the most preferred pattern and consistent with the idea that localization motifs are gain-of-function for localized RNA.

Finally, we looked to see how many of the neurite-preferred isoforms were among the ~2,000 new, distal 3'UTRs annotated recently by Miura *et al*. [19]. Thirty eight of the neurite-preferred isoforms overlapped this list, 12 of which were specific to hippocampal neurons in that study [19]. Two examples from this set of 38 are included in Figure 4-6 (middle and bottom). We are in the process of validating several of these differential localization events experimentally using FISH. Overall, these results support the idea that neurons utilize alternative 3'UTRs to localize a subset of RNAs to the neurites.

4.2.3 Dendritic targeting motifs

Having defined the set of RNA sequences that are localized to the dendritic compartment, including alternative and under-annotated 3'UTR isoforms, we can use this information to perform a comprehensive search for potential DTEs. We expect that a DTE should be a motif, either linear or structural in nature (or possibly both), that occurs more frequently in the localized sequences than the non-localized sequences. We searched each set of localized RNAs separately (gene-level, isoform-level, and consistent neurite) to identify any differences between the sets.

Linear motifs

First, we searched for instances of known RBP binding motifs using the HOMER software package [31,32]. RBP motifs were obtained in the form of positional weight matrices from the CISBP-RNA database [33], which contains experimentally determined binding RBP preferences based on RNAcompete [34]. Motifs were tested for enrichment using background datasets consisting of 3'UTRs from non-localized genes that were matched to the length distribution of the foreground set (see "Background datasets for motif enrichment" in Methods).

After multiple test correction, only two RBP motifs were significantly enriched in the gene-level localizers (Rbm46 motif GAUGAU and Srsf3 motif AUCAWCG; adjusted $p < 0.01$, Hypergeometric test), and no motifs were significantly enriched in the isoform-level localizers. The consistent neurite set was significantly enriched for 61 different RBP motifs (adjusted $p < 0.01$); however, each of these motifs was only slightly more common in the localized sequences than the background (odds ratio ≤ 1.5). Overall, the highest odds ratio by far was for Srsf3, mentioned above, which was 2.4 times more common in the gene-level localizers than background and occurred in 59 of the 387 genes in this set. The same Srsf3 motif also had the highest odds ratio in the consistent neurite set (1.5) and occurred in 265 of the 1,863 genes in this set. Srsf3 is a brain-expressed splicing factor, and although no specific role for this RBP in neurons has been described, it was recently shown in mouse P19 cells to promote 3'UTR lengthening through distal polyadenylation site usage and promote nuclear export through recruitment of NXF1 [35]. Therefore, one hypothesis could be that Srsf3 plays a role in the early steps of dendritic localization by promoting inclusion of alternative 3'UTR (theoretically containing DTEs) and by facilitating nuclear export.

We next performed a *de novo* motif analysis using HOMER to see if any previously unidentified motifs were enriched in our sequences. Five to seven motifs were enriched in each set. The top motif in each set was as follows: in the gene-level localizers, the motif UUCGAU (p = 0.0001, odds ratio = 2.9, Hypergeometric test); in the consistent neurite set, the motif CCGCAA (p = 1e-7, odds ratio 1.7); and in the isoform-level localizers, GUGGGU (p = 0.01, odds ratio = 1.2). One motif, CGCR, was found in all three sets, but was only slightly more common in localizers than background (odds ratio < 1.2). Based on these analyses, linear motifs—with the possible exception of the Srsf3 motif—do not appear to fill the role of the "common" DTEs that we hoped to find in the dendritically targeted genes.

Structural motifs

As discussed in sections 1.3.4 and 4.1, there is a growing awareness of the importance of RNA structure in the process of dendritic localization. Until recently, there were no publically available tools for finding novel RNA secondary structure motifs that could handle large numbers of sequences, and thus there have been no large-scale surveys of potential novel RNA structure DTEs, despite several mentions in the literature of how important such a survey would be [28,36,37]. Here, following up on the work described in Chapter 2, Section 2.2.4, we perform a *de novo* prediction of RNA structures enriched in dendritically localized 3'UTRs.

Since G-quaduplexes have been implicated previously in dendritic localization [38], we first searched our localized sequences for regions that could potentially form this structure. Identifying putative G-quaduplexes does not require special software, since they can be recognized as a linear sequence of four repeated units of (most commonly) three or more consecutive G's, with each repeat separated by two to seven nucleotides of any kind. Using a regular expression representing this pattern, we searched for potential G-quadruplexes in the 3'UTRs of each localized gene as well as a background set of 3'UTRs belonging to non-localized genes (length-matched to the localized 3'UTRs; same as previous section). G-quaduplexes were 2.0 times more common in the gene-level localized RNAs (p = 0.003, Fisher's exact test), 1.9 times more common in the consistent neurite RNAs (p = 5.0e-12, Fisher's exact test), and 1.7 times more common in the isoform-level localizers (not significant; p = 0.14, Fisher's exact test) than the non-localized background. Overall, 448 localized genes had at least one G-quadruplex. These results support a potential role for G-quaduplexes in dendritic RNA, but the fact that these structures occur frequently in non-localized sequences as well suggests that there are probably other unknown factors that determine the specificity of localization machinery for localized RNAs. Since there are some reports of FMRP binding G-quaduplexes, it may be that these motifs play a role in translational repression of RNAs during dendritic transport [39]. However, these reports are mixed [40] and will require further study.

Next, we applied our tool NoFold (Chapter 2) to identify novel structural motifs in these sequences. A total of 554 motifs were found that occurred in three or more localized sequences. Of these, 85 were significantly enriched compared to non-localized background sequences ($p < 0.01$, Fisher's exact test), making them possible candidates for DTEs. Two motifs stood out as occurring in a large number of sequences (over 20 unique genes each). Though more conserved on the structure level, the instances of these motifs had enough sequence similarity to suggest a common origin, e.g. a transposon. Using RepeatMasker [41], we identified these motifs as instances of the B1 and B2 SINE families, respectively, which are ~175nt retrotransposons that form long hairpin structures.

To verify that these SINEs are enriched in the localized sequences, we created covariance models (CMs) for B1 and B2 using their canonical sequences from RepeatMasker and predicted secondary structure from RNAfold [42]. Both elements were trimmed down to the structurally stable part of their secondary structure prior to CM creation: for B1, a small amount of unstructured sequence was trimmed from each end of the single stable hairpin; for B2, only the first hairpin was kept (first ~70nt) because the second predicted hairpin is less stable and may actually be partially single-stranded according to structure probing data [43]. Since CMs model both primary and secondary structure, they can identify instances of a structural sequence that is divergent on the sequence level, as long as the structure is conserved. We used the B1 and B2 CMs to scan all the localized and non-localized sequences (length-matched; see Methods) and filtered out low-similarity matches based on bitscores. Structurally consistent B1 sequences were found 2.5 times more often in gene-level localizers ($p = 0.00047$, Fisher's exact test), 1.8 times more often in consistent neurite RNAs ($p = 7.6e-7$, Fisher's exact test), and 1.9 times more often in isoform-level localizers (not significant; $p = 0.33$, Fisher's exact test) as compared to non-localized sequences. Structurally consistent B2 sequences were found 2.5, 1.9, and 5.7 times more often in the gene-level, consistent neurite, and isoform-level localizers respectively ($p < 0.001$, Fisher's exact test). Overall, 255 and 165 localized genes (out of 2,225 total) contained a structurally-consistent B1 or B2 match, respectively. These results verify that B1 and B2 SINE-related sequences are widespread and over-represented in localized RNAs, suggesting a possible role as DTEs. Notably, while gene-level localized RNAs had high frequencies of both B1 and B2 elements, isoform-level localized RNAs had a strong preference for only the B2 element. An interesting possibility is that each of these elements represents a different localization pathway, which could allow the neuron to separately regulate the localization of functionally-coherent groups of RNAs—i.e. a "post-transcriptional operon" [44]. We also found that 58 localized genes contained both B1 and B2 elements, indicating that some genes could be localized by both pathways.

How might B1 and B2 drive localization? Since these elements are predicted to have stable secondary structure, one possibility is that they are bound by RBPs that recognize double-stranded RNA (dsRBPs). One of the most well characterized dsRBPs in neurons is Staufen, which additionally has been implicated in dendritic localization in the past. However, using the results of a recent survey of Staufen2-bound RNAs in rat hippocampal neurons [45], we found no significant enrichment of Staufen2 targets among the B1 or B2-containing RNAs, suggesting that they are localized by some other RBP or mechanism. Previously, another hairpin-forming SINE element (the ID element; derived from the dendritically-localized BC1 RNA) has been shown to cause dendritic localization in rat neurons [18,46]. In this case, two sub-motifs within the structure were shown to be particularly important for localization: a single nucleotide bulge (U) was required for nuclear export, and a GA kink-turn (GA-KT) motif was needed for localization to the distal dendrites [46,47]. It was found that the RBP hnRNP-A2, a likely dendritic localization mediator, bound to the BC1/ID element GA-KT motif [46,47] and to GA-KT motifs more generally [48]. Both B1 and B2 have regions where a GA-KT motif might be possible (Fig. 4-8). B2 additionally has a U-bulge, similar to the BC1/ID element (Fig. 4-8B). The A-G/G-A nucleotides that make up the putative GA-KT motifs are generally well conserved across the instances of B1 and B2 in the localized genes, despite high sequence variability in many other regions of the structure, suggesting that this region could indeed be important (Fig. 4-9). However, it is worth noting that this region is also conserved in the non-localized instances of B1 and B2, and thus may not be sufficient to induce localization. Future work will include experimental validation of the B1 and B2 elements as DTEs via expression constructs, which will allow us to test the importance of various sub-motifs for localization.

4.2.4 Functional analysis of the “local proteome” using structure information

To gain a better understanding of the structures and functions provided by locally translated proteins in the dendrites (the “local proteome”), we performed a domain-level tertiary structure prediction on the protein products of 1,930 localized mRNAs (combining the gene-level localizers, isoform-level localizers, and consistent neurite lists and excluding non-coding RNAs). A single “canonical” protein sequence was chosen to represent each localized RNA based on UniProt [49] annotations. Full length proteins were split into one or more domains (see Methods) and each domain was classified into a SCOP structural fold using our PESS pipeline, as described in Chapter 3. Of the 6,822 input domains, 4,319 (63%) had a “high confidence” structure prediction (nearest neighbor distance less than 17.5), and an additional 2,428 (36%) had a “medium confidence” structure prediction (nearest neighbor distance between 17.5 and 30), for a total of 98.9% of domains with a prediction. Previously, some of these domains were structurally annotated by Gene3D, which uses hidden Markov models (HMMs) to detect matches to CATH superfamilies [50]. We were able to predict the fold of 2,005 additional domains that were not previously annotated by Gene3D (high confidence threshold; 3,550 new predictions using the medium confidence threshold), demonstrating the increased sensitivity of using three-dimensional structure information to make fold predictions compared to linear models such as HMMs.

The most common folds in the local proteome were similar to what was observed in the overall human proteome in Chapter 3, with superfolds such as Beta-beta-alpha zinc fingers and Alpha-alpha superhelices being most common (Fig. 4-10). However, the local proteome had a notably higher frequency of Single transmembrane helix, Immunoglobulin-like, and Ferredoxin-like folds (Fig. 4-10). To better assess the local dendritic proteome in the context of neuronally-expressed proteins as a whole, we repeated the structure prediction process described above for all genes expressed in at least half of the RNA-seq samples (including soma samples) to obtain a mouse "whole-neuron proteome" structure set. The top folds of the whole-neuron proteome were very similar to the local dendritic proteome (Fig. 4-10). In addition, using the whole-neuron proteome as a background, we found that the local dendritic proteome was highly enriched for diverse folds (Figure 4-11A), including several related to cytoskeletal structure such as Spectrin repeats, actin-binding Profilin domains, and Tubulin nt-binding domains. Overall, 503 different folds were represented by at least one domain in the local dendritic proteome, covering almost the entire spectrum of folds expressed in the neuron as a whole (609 folds) (Figure 4-11B). This suggests that rather than being highly specialized, the local dendritic proteome encodes for a diversity of functions on par with the whole cell. This generally held true even when the local proteins were filtered to only those previously identified in other studies (based on the curated set of dendritic RNAs used in section 4.2.1), although the coverage of the structure space was more sparse (Fig. 4-11C).

To highlight some of the insight that can be gained through structure analysis, we selected several folds with important neuronal functions and assessed their representation within the locally translated set, which we describe below.

Synaptic functions

The PDZ fold is one of the most well-characterized protein structures involved in the synapse because of the crucial role it plays in protein-protein interactions between the intracellular scaffolding of the spine and membrane-bound receptors as well as cell adhesion molecules [22]. There were 21 proteins in the local proteome set that contained at least one PDZ fold, with many containing more than one (Table 4-4). All 21 of these proteins were previously annotated as containing a PDZ domain by Gene3D, indicating that this fold has already been well characterized across proteins. Similarly, all eight of the predicted guanylate kinase (GK) domains and all 32 of the predicted SH3 domains—both of which frequently co-occur with PDZ domains at the synapse [24]—were previously annotated (Table 4-4). These results demonstrate the specificity of our method, and also highlight the potential role of local translation as a source for these important scaffolding proteins.

Many other folds had a mixture of both known and novel predictions. For example, we predicted 24 proteins to have the Pleckstrin homology (PH) domain, which is involved in membrane targeting through recognition of phosphatidylinositol. Twenty two of these proteins were already annotated as having a PH domain by Gene3D. The remaining two proteins were Nischarin (Nisch) and Sphingosin kinase 2 (Sphk2), which are both annotated as phosphatidylinositol-binding but had no annotated domain or structure. Thus, by using structure annotation, we were able to provide a specific domain annotation and location for a known function of these proteins. Another novel prediction was made for Capicua (Cic), a transcriptional repressor that interacts with Ataxin-1 and plays a role in central nervous system development. We predicted this protein to have a previously-unannotated Tudor domain near its N-terminal. Tudor domains may play a role in stress granule formation through binding of methylated RGG motifs [51] and more generally are found in RNPs. This suggests potential new roles for Capicua beyond its known transcription-related functions. We highlight additional known and novel predictions for membrane-bending Bin-Amphiphysin-Rvs (BAR) domains and actin-binding Calponin homology (CH) domains in Table 4-4.

Membrane-bound

Membrane-bound proteins play a variety of crucial roles at the synapse, including signal transduction, cell adhesion and anchoring, neurotransmitter reception, cation influx/efflux, and scaffolding. There were 274 proteins in our local proteome set with at least one high-confidence TM domain prediction (Table 4-5), and 111 additional proteins with a medium-confidence prediction. Many of these were already known, such as those predicted to have the gated ion channel fold, e.g. Gria1/2, Grin1/2b, Kcnh7, and Scn2a1. There were also several unexpected results, especially for the single transmembrane helix fold. This fold encompasses a variety of simple hydrophobic helices, and was predicted with high confidence in 187 proteins, many of which were not known to be membrane-bound proteins. Further investigation revealed that for 39 of these proteins, the predicted TM domain occurred at the very beginning of the protein and corresponded to a signal peptide sequence (as predicted by SignalP [52]). Signal peptides often have similar characteristics as TM domains, which may explain why these domains were predicted to have this fold. Since signal peptides are usually cleaved off during processing, it is important to note that some of these proteins may not be membrane-bound in their mature form.

To better characterize the purpose of locally translated TM-containing proteins, we surveyed other structural domains predicted for those proteins. The most common co-occurring folds included immunoglobulin-like beta-sandwiches (40 occurrences), which encompasses many cell adhesion structures such as cadherin; SH3-like barrels (29 occurrences), which includes many protein-protein interaction structures; and protein kinase-like structures (11 occurrences). Overall, these results support the idea that there are numerous locally-translated membrane proteins, which are likely translated on-demand during L-LTP to help stabilize the growing synapse, anchor intracellular scaffolds, and increase signal transduction through the synapse.

RNA binding

RBPs play crucial roles in localizing RNAs to the dendrites and in regulating their translation. But how many RBPs locally translated themselves? We surveyed the local proteome for predictions of folds that we previously identified as being associated with RBD function (see Chapter 3) and found 1,254 proteins with high confidence matches to one of these folds. Since some of these folds are not completely specific to RNA-binding function, we narrowed our focus to a set of 10 folds or superfamilies with a higher specificity for RNA-binding. There were 138 proteins with one or more domains matching these structures with high confidence (Table 4-6) and 77 with medium confidence, demonstrating that a wide variety of RBPs may indeed be produced by local translation. Among this set were many well-known RBPs with neuronal functions and/or relationships to neuropsychiatric disorders, such as Atxn2, Stau1/2, Elavl2/3, Mbnl2, and Cpeb2.

In addition, several of the predicted RBPs either were not previously known to be RBPs, or were known to bind RNA but did not yet have an annotated RBD. Two examples of the latter category were Dync1h1 (Cytoplasmic dynein 1 heavy chain 1), for which we predicted a Poly(A) binding protein (PABP) domain-like structure between residues 2,042 and 2,174; and Trub2 (Probable tRNA pseudouridine synthase 2), which we predicted to have a OB-nucleotide binding domain between residues 40 and 86, adjacent to the known catalytic domain. Looking into the medium-confidence predictions, we also found completely novel RBP predictions such as Mga (MAX gene-associated protein), a transcription factor that we predicted to have a dsRBD-like fold (residues 563-862) downstream of the DNA-binding domain; and Akap11 (A-kinase anchor protein 11), a kinase-regulating protein that we predict to have a type I KH-domain fold at the C-terminal (residues 1,501-1,894).

What might be the role of locally translated RBPs in establishing or maintaining synaptic potentiation? Dync1h1, mentioned above, is involved in retrograde transport in dendrites, so one possibility is that the translation of this protein in response to activation promotes transport of poly(A) RNA and other cargos back to the soma. These cargos, which might include transcription factors (TFs), could then in turn promote new transcription, which is also a requirement for L-LTP [53]. Related to this, TF mRNAs have also been found to be dendritically localized in other studies [8,54], and are hypothesized to be translated in response to activation and then transported back to the soma to promote L-LTP-related transcription. We also find several known TFs among our localized RNAs, and additionally identified a handful of TF with a potential dual function as an RBP (e.g. Mga, Fubp1). Another possible role of locally translated RBPs is transient promotion of cytoplasmic splicing [55], as several of the predicted RBPs are splicing factors (e.g. Rbfox1/2, Elva12/3, Mbnl2, Fus). One hypothesis could be that the expression of these splicing-related RBPs during a “pioneer” round of local translation promotes splicing-out of cytoplasmically-retained introns in other local mRNAs to allow their translation. RBPs involved in RNA modification are also locally expressed, including *Adarb1* (ADAR1) and *Trub2*. These RBPs could play a role in regulation of translation and RNA stability during L-LTP. ADAR1 is also known to modify several receptors and channel proteins that are important at the synapse, including glutamate receptor subunits. This editing has been shown to modulate the conductance properties of these channels and can affect LTP [56,57].

Using structure to understand disease

Knowledge of protein structure can greatly aid in understanding the relationship between mutations and disease. For example, structure information can improve predictions of which mutations in a protein will be deleterious, helping researchers prioritize mutations for experimental follow-up. In the cases where a disease-causing mutation has already been identified, structure analysis can provide insight into the possible mechanism of action of the mutation, ranging from high-level information (e.g. finding that the mutation occurs in a likely RNA-binding domain) to fine-grained information (e.g. finding that the mutation disrupts a specific residue in a catalytic site). Given that our structural annotations for the local dendritic proteome covered many domains that previously did not have a structure prediction, there are likely many new insights that can be gained about disease by linking these structure predictions with existing mutation information. Here, we provide a first-pass analysis to identify cases where our new predictions are most likely to lead to new information about neurological disorders related to learning and memory, particularly those with potential relevance to humans.

Since we made over 3,500 new structure predictions for domains of the local dendritic proteome (i.e. those without a previous Gene3D prediction), we first filtered this set to those most likely to provide immediate insights. Using Mammalian Phenotype Ontology annotations [58], we filtered the ~3,500 domains to only those occurring in proteins annotated as being associated with abnormal synapse-, dendrite-, or memory-related phenotypes. To further prioritize this list, we additionally filtered to just the domains that contained a pathogenic or likely-pathogenic non-synonymous variant in humans (using ClinVar annotations; see Methods). Together, these filtering steps resulted in 94 domains in 52 proteins that have new structure predictions and potential relevance to neurological disorders and human disease (Table 4-7). We note that since there are sometimes differences between human and mouse proteins (ranging from small insertions or deletions of amino acids to complete loss or gain of domains), the position of a mutation in a human protein does not necessarily correspond to the same amino acid position in mouse, and thus the human mutation information should not be directly mapped onto a predicted mouse structure on the amino acid level. Nonetheless, since protein structure is generally highly conserved across evolution, it is reasonable to expect that on the whole-domain level, most structure predictions made in mouse will carry over to the corresponding protein domain in humans. Therefore, we expect that the mouse structure predictions listed in Table 4-7 can be used as a starting point for understanding the high-level functional consequences of human mutations. More generally, it should also be possible to use many of the new structures to predict the impact of mutations that are not yet known to be deleterious, e.g. by providing this information to tools such as PolyPhen [59] that can utilize structure information when available.

4.3 Conclusions

In summary, we have demonstrated here the application of subcellular RNA-profiling and structure-based computational analysis towards the goal of understanding the “who”, “how”, and “why” of dendritic RNA localization. We identified a total of 2,225 unique genes that were targeted to the neurites, including 298 genes for which only a subset of the expressed transcripts were localized, depending on their 3’UTR isoform. Many of these differentially localized 3’ isoforms were among the set of recently identified distal 3’UTRs expressed in neurons [19]. Using *de novo* RNA structure motif analysis, we identified several secondary structures enriched in the 3’UTRs of the localized RNAs, including two hairpin structures derived from B1 and B2 SINE elements. Finally, we applied a sensitive protein fold prediction algorithm to make structural and functional predictions for the set of proteins that are putatively translated locally at the synapse. These results bring us closer to understanding the regulation of RNA targeting to the dendrites and the roles that localized RNAs play in synaptic plasticity.

One limitation of this study is that it only surveys neurons at the basal state, rather than after synaptic stimulation. Several studies have shown that RNA localization changes after stimulation [60–63]; therefore, the set of neurite RNAs identified here may still be only a subset of the RNAs needed for LTP. There also may be important differences between neurons in culture and *in vivo* that would be missed in our analysis. We observed significant overlap between our localized set and a set of known localized RNAs derived partly from tissue-based studies conducted after fear conditioning (Fig. 4-3B, 4-4A, 4-5E; also see Methods), suggesting a reasonable amount of concordance between basal primary cultures and post-stimulation tissue samples. Nonetheless, an important future direction will be to repeat the sub-cellular sequencing described here after stimulation. It will be particularly interesting to see if groups of RNAs that share a DTE undergo coordinated changes in localization post-activation, and conversely, if coordinated RNAs share any new DTEs. We further explore the implications and future directions of this work in the next chapter.

4.4 Methods

Neuron culture and collection

Hippocampal neurons from embryonic day 18 (E18) mice (C57BL/6) were cultured as described in [64] for 15 days. Isolated single neurons were selected for collection. A micropipette with a closed, tapered end was used to sever neurites from the cell body. A micropipette was used to aspirate the soma, which was deposited into a tube containing first strand synthesis buffer and RNase inhibitor and placed on ice. A separate micropipette was then used to aspirate the neurites, which were deposited into a separate tube as above. Samples were transferred to -80ºC within 30 minutes and stored there until first strand synthesis. Sixteen neurons (32 total samples) were collected from multiple cultures across multiple days.

Single cell RNA amplification and sequencing

ERCC spike-in control RNA was diluted 1:4,000,000 and 0.9uL was added to each tube. Poly-adenylated RNA was amplified using two or three rounds of the aRNA *in vitro* transcription-based amplification method, as described in [65]. The quality and quantity of the amplified RNA was verified using a Bioanalyzer RNA assay. Strand-specific sequencing libraries were prepared using the Illumina TruSeq Stranded kit according to the manufacturer's instructions, except that the initial poly-A capture step was skipped because the aRNA amplification procedure already selects for poly-adenylated RNA. Samples were sequenced on a HiSeq (100bp paired-end) or NextSeq (75bp paired-end) to an average depth of 25 million reads. Reads were trimmed for adapter and poly-A sequence using in-house software and then mapped to the mouse genome (mm10) using STAR [66]. Uniquely mapped reads were used for feature quantification using VERSE [67]. The features used for each analysis are described below.

Gene and 3'UTR definitions

Three sources of gene annotations were combined to obtain a comprehensive definition of known 3' ends: Ensembl genes (downloaded from UCSC, Dec 2015); UCSC genes (downloaded from UCSC, Dec 2015); and the set of ~2,000 new 3'UTRs determined by Miura et al. [19]. The 3'UTR regions of these annotations were used for quantification of reads, as will be described in more detail in the sections describing the gene-level and isoform-level analyses.

Cell type marker genes

Gene markers of pyramidal neurons and cardiomyocytes, as well as housekeeping genes, were obtained from [15]. Markers of other mouse brain cell types were obtained from [68].

"Known dendritic" gene list

A list of 1,925 previously observed dendritic genes was compiled from three sources: *in vivo* ribosome-associated RNAs from mouse hippocampal neuropil punches (shown to be reasonably specific to pyramidal dendrites) [8]; FISH experiments in cultured primary mouse hippocampal neurons (C. Francis, personal communication); and from general knowledge accumulated from the literature. The combined list was filtered to remove any genes that were not included in the input set of genes for quantification (as defined in “Gene and 3’UTR definitions”, above).

Gene-level expression and localization

A single 3’UTR feature was created for each gene by taking the union of all 3’UTR regions for that gene (see Gene and 3’UTR definitions, above). Read counts were calculated for each gene based on how many reads mapped to this 3’UTR region. Quantification was done using VERSE with options “-s 1 -z 3 --nonemptyModified”. For differential expression analysis, we used only the genes that had at least one read in at least half (16) of the samples. Read counts were normalized based on size factors using the protocol built into DESeq2. Differentially expressed genes between the neurites and soma were identified using DESeq2 with a paired experimental design, which allowed us to directly compare the expression between the soma and neurite compartments of each individual neuron. A FDR corrected $p \leq 0.05$ was used to identify significantly differentially expressed genes. The consistent neurite genes were identified separately based on having at least 1 read in at least 90% (i.e. 15 out of 16) of the neurite samples.

GO functional enrichment of gene-level localizers and consistent neurite genes was calculated using the GOrilla webserver [69]. For gene-level localizers, the background set for GO analysis was all genes with at least one read in half the samples; for the consistent neurite genes, the background was all genes with at least one read in at least 15 samples (i.e. the input sets for each analysis).

Isoform-level expression and localization

To quantify individual 3’ isoforms of genes, we used the last 500nt of each 3’ end for that gene as the isoform quantification feature. Any 3’ ends that were less than 500nt apart were merged together into a single quantification feature. Thus, the final set of 3’ isoform quantification features is non-overlapping. Isoform read counts were calculated by VERSE using the same parameters as above. Genes with only one expressed 3’ isoform were removed from further analysis to focus on alternative expression of 3’ isoforms.

To identify the top two 3’ isoforms for each gene, the following procedure was used. For each gene in each sample, the fraction of reads mapping to each isoform was calculated (that is, the number of reads mapping to that isoform divided by the total reads for all isoforms of the gene). The fractions for each isoform were then summed up across samples (unless a sample had fewer than 10 reads total for that gene, in which case it was skipped) and the two isoform with the highest total per gene were considered the top two isoforms for that gene. The purpose of this process was to give each sample equal weight in the final decision of the top 3’UTR, while also excluding samples with too few reads to give a reliable estimate of the isoform fractions. This process was repeated for each gene with at least two expressed isoforms in the dataset. Then for each gene, whichever of the top two isoforms was more 5’ (as defined by the locations of their 500nt quantification features) was designated the “proximal” isoform, and whichever was more 3’ was designated the “distal” isoform. Finally, for each gene in each sample, we calculated the distal fraction (DF) as the fraction of reads mapping to the distal isoform divided by the total reads mapping to the distal and proximal isoforms.

We defined the proximal and distal isoforms as being, relative to each other, generated by alternative splicing (i.e. they are ALEs) or alternative cleavage and polyadenylation (i.e. they are Tandem UTRs) by the following criterion: if the full length 3'UTRs of a pair of isoforms were directly adjacent or overlapping, they were called tandem; otherwise, they were called ALEs.

The differential localization of isoforms was determined based on the change in distal fraction between soma and neurites of the same original neuron. A non-parametric paired test of differences (Wilcoxon signed-rank test) was used to identify genes with consistent changes in distal fraction across samples. Only genes with at least five pairs of samples (where a "pair" means the soma and neurites from the same original neuron) where each member of the pair had at least 10 combined reads for the two isoforms were tested (3,638 genes), to ensure there was enough read- and sample-support to reliably identify these events.

GO enrichment was done on the neurite-enriched isoforms as described in the previous section, using the input set of 3,638 genes as background.

Background datasets for motif enrichment

We generated a pool of "non-localized" background sequences based on the list of genes that were significantly higher expressed in the soma from the gene-level DESeq2 analysis described above. We filtered this set to remove any overlap with one of the other localized lists (i.e. the consistent neurite list and the isoform-level list) and any overlap with previously annotated dendritically localized genes (same list of curated “known” dendritic genes described above) in order to make this list as specific to non-localized genes as possible. Since motif frequency in a sequence can be related to sequence length, a background set should be matched as closely as possible to the length distribution of the foreground set when doing motif analysis. With this in mind, we created a length-matched background set for each of the three localized gene lists as follows: (1) for each localized gene in the set, scan the pool of non-localized genes in order of their somatic specificity (starting with the most soma-specific, as indicated by its DESeq2 test statistic); (2) select the first non-localized gene encountered with a 3’UTR length within 100nt of the localized gene’s 3’UTR length; (3) add the selected non-localized gene to the background set and remove it from the pool; (4) if no background gene can be found that meets the 100nt criteria, select whichever gene in the pool that has the most similar 3’UTR length to the localized gene’s 3’UTR. Using this protocol resulted in background sets with highly similar length characteristics to the foreground set.

RNA motif analysis

Linear motifs were identified using the HOMER motif-finding suite [31]. *De novo* enriched motif searches were done using the script “findMotifs.pl” and set to look for either short motifs (4 or 6nt) or long motifs (8, 10, or 12nt). Enrichment of known RBP binding motifs was analyzed using the same script with option “-known” in combination with a custom set of positional weight matrices specifying binding preferences that was downloaded from CISBP-RNA (version 0.6) [33]. A log-odds threshold for RBP motif matching was set for each motif separately based on the number of informative positions in the motif such that longer, more specific motifs had a higher log-odds threshold for calling a match. The background sets used for enrichment testing were the length-matched non-localized sets described above.

G-quadruplexes were identified by regular expression search using the “re” module in Python. The search pattern was '([gG]{3,}\w{1,7}){3,}[gG]{3,}', which requires three consecutive matches to the pattern “three or more G’s followed by 1-7 of any nucleotide” and then ending with a fourth set of three or more G’s. The background set was the same as described in the previous section.

De novo identification of enriched RNA secondary structures was performed using NoFold [70]. Sliding windows of 100nt (slide = 75nt) across the localized sequences were used for input. Background datasets were the same as described in the previous section and also converted to sliding windows with the same parameters.

Matches to the B1 and B2 elements were found by creating a CM for each element based on its canonical sequence(s) downloaded from RepeatMasker [41] and its predicted MFE structure from RNAfold [42]. The sequences and structures used to create the CM are as follows:

B1 sequence:

GAGGCAGGCGGATTTCTGAGTTCGAGGCCAGCCTGGTCTACAGAGTGA
GTTCCAGGACAGCCAGGGCTACACAGAGAAACCCTGTCTC

B1 structure:

((((((((....(((((((((((..(((...(((((.((........))..)))))...))).)))))...))))))...))))))))

B2 sequence:

GCTGGTGAGATGGCTCAGTGGGTAAGAGCACCCGACTGCTCTTCCGAA
GGTCAGGAGTTCAAATCCCAGC

B2 structure:

(((((.((..((((((....((.(((((((......))))))))).........))).)))..)))))))

Bitscore cutoffs for high-quality matches were set to 50 for B1 and 35 for B2 based on the length of the model. Enrichment was computed using Fisher’s exact test based on the number of high quality matches in the localized set compared to the non-localized background (same background as above). Only one match was counted per gene for the purposes of enrichment testing.

Protein structure analysis

For each predicted neurite RNA (gene-level localizers, consistent neurite, and isoform-level localizers), we obtained the canonical protein sequence, if any, from UniProt [49]. The canonical isoform is defined by UniProt to usually be the one that is most inclusive of exons/domains. We note that the protein sequence chosen does not necessarily correspond to the exact RNA isoform in the case of the isoform-level localizers. We refer to this protein set as the “local proteome”. We also obtained the canonical protein sequences for the full set of expressed genes in soma and neurite samples (at least 1 read in at least 15 samples) to use as a background for comparison with the local proteome.

Each protein was split into domains based on DomainFinder Gene3D predictions [50,71]. If there were regions between, before, or after predicted domains that were longer than 30 amino acids (aa) but did not have a Gene3D prediction, we also included those. If a “filled in” region such as this was longer than 450 aa, we used a sliding window of 300 aa (slide = 150 aa) to break it into smaller pieces, since domains are rarely larger than this. The fold of each domain was predicted using the method described in Chapter 3. A threshold of ≤ 17.5 was used to designate “high confidence” predictions, and a more lenient threshold of ≤ 30 was used to designate “medium confidence” predictions.

Mammalian Phenotype Ontology (MP) annotations for mouse genes were downloaded from MGI [58]. MP terms related to synapse, dendrite, and memory phenotypes were identified by filtering the MP terms to those containing the following keywords: "synapse", "synaptic", "learning", "memory", "dendrite", "dendritic", and "potentiation". Human mutations were downloaded from ClinVar [72] and filtered to non-synonymous single-nucleotide variants marked as “pathogenic” or “likely pathogenic”. These mutations were transferred to mouse protein domains based on their amino acid position in the human protein (note: human and mouse amino acid positions are not expected match up exactly in all cases, so this should not be taken as a precise mapping of human mutations onto mouse structures, but rather as an indication of potential disease relevance for the predicted structure on the domain level). The mapping between human and mouse orthologous proteins was obtained from the International Mouse Phenotyping Consortium website (http://www.mousephenotype.org/).

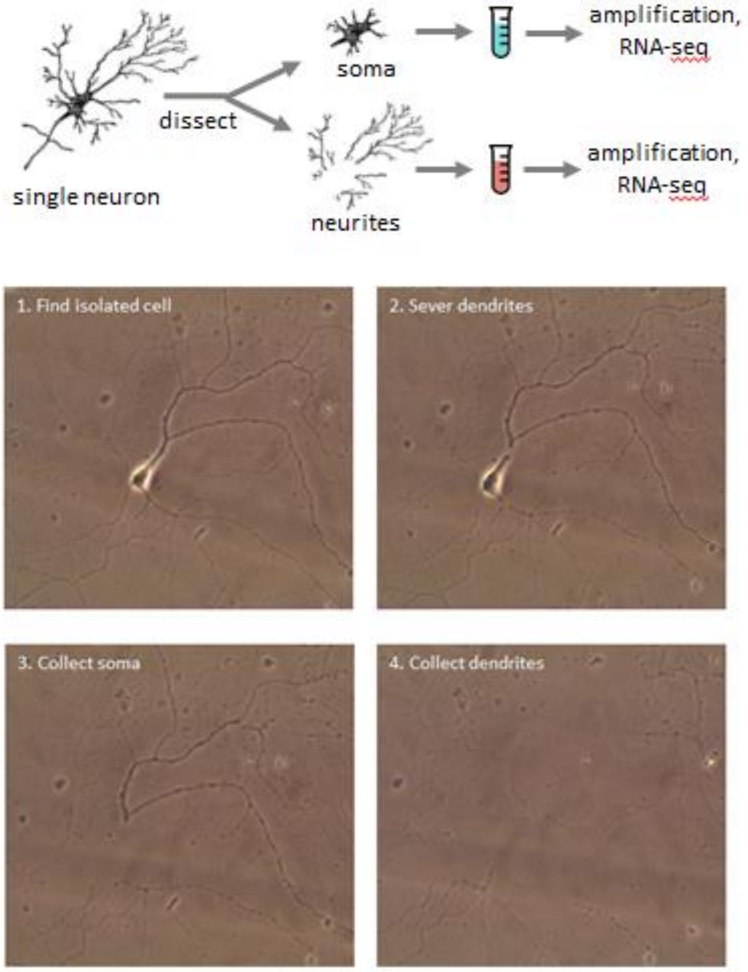

Figure 4-1. Sub-single cell profiling of soma and neurite RNA.

Isolated single neurons are dissected to separate the soma and neurites, which are collected into separate tubes for RNA amplification and RNA-sequencing.

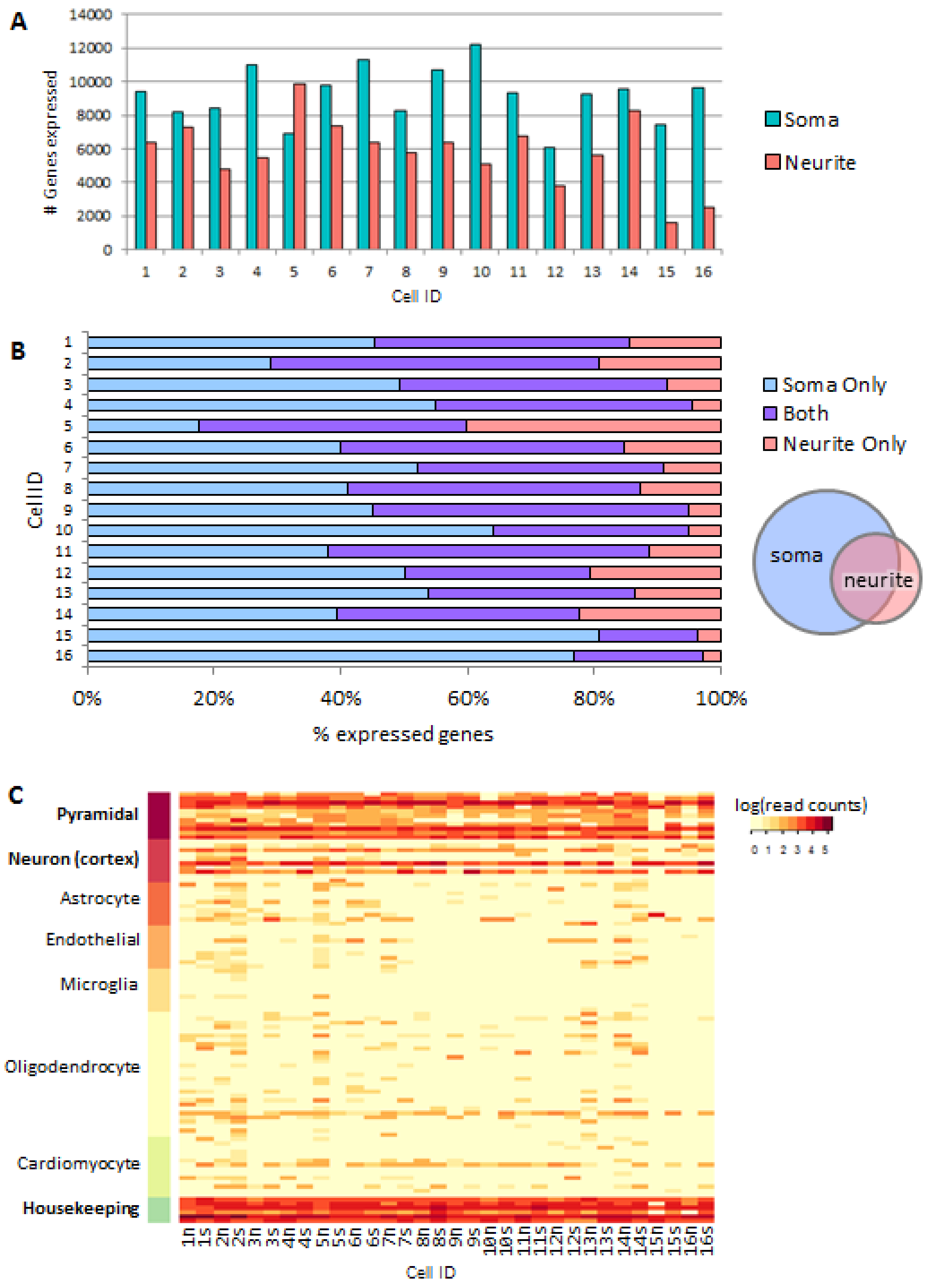

Figure 4-2. Overview of gene expression in individual soma and neurite samples.

(A) Number of genes expressed per sample with at least 10 reads. (B) Overlap of expressed genes (≥10 reads) between soma and neurites from the same original cell. (C) Marker gene expression for several brain cell types. Samples (columns) are indicated by their cell number and “s” for somas and “n” for neurites. As expected, pyramidal neuron markers were highly expressed. Cardiomyocte markers are included as a cell type very unlikely to be present in our cultures and/or confused for a neuron, in order to demonstrate that low/medium expression of other cell type markers is normal.

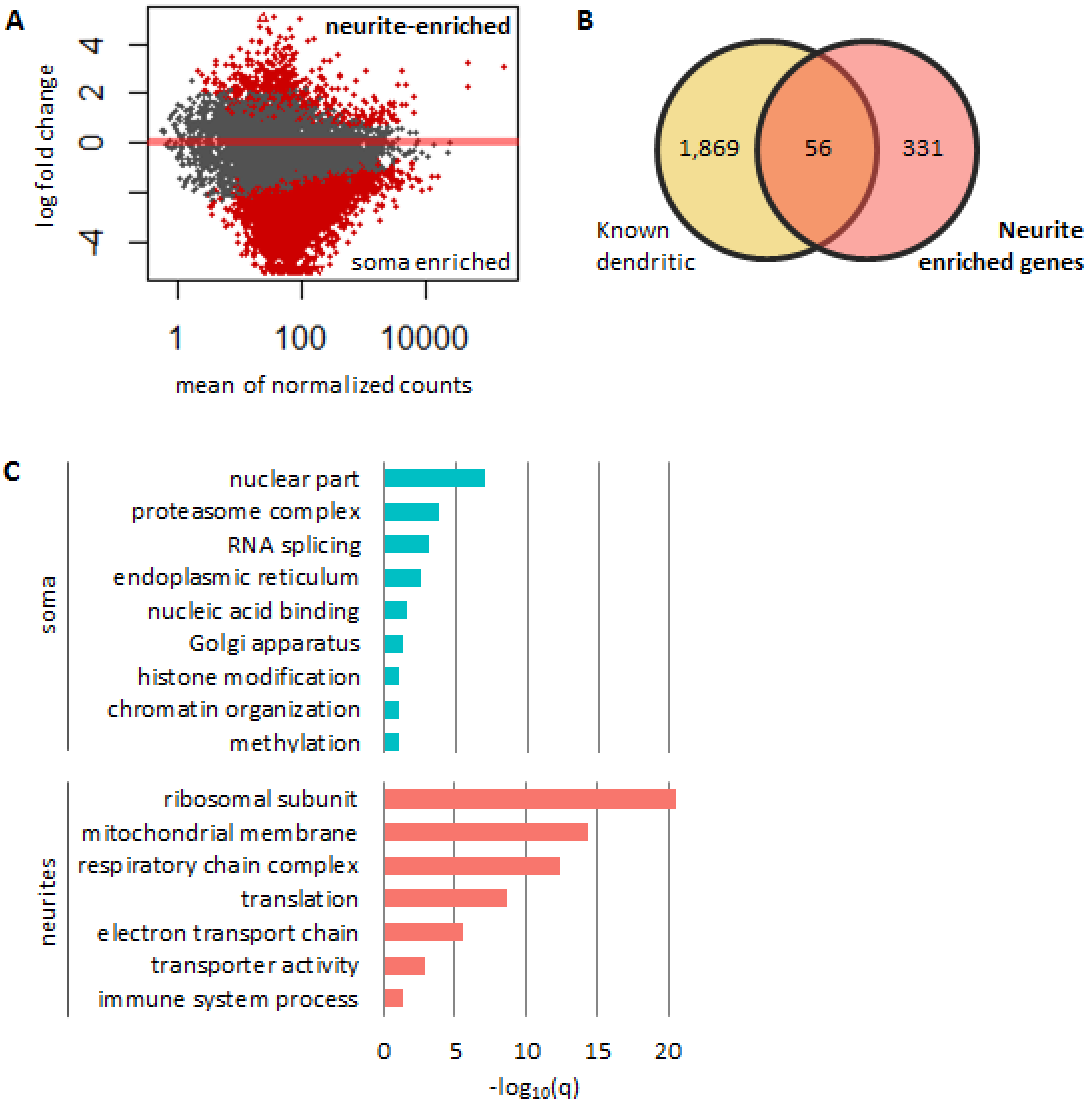

Figure 4-3. Differentially expressed genes between soma and neurites.

(A) Mean gene normalized counts vs log fold change between neurites and soma. Significantly differentially expressed genes are shown in red. (B) Overlap between neurite-enriched genes and previously annotated dendritic genes. (C) Selected GO terms enriched in the soma- and neurite-enriched gene lists.

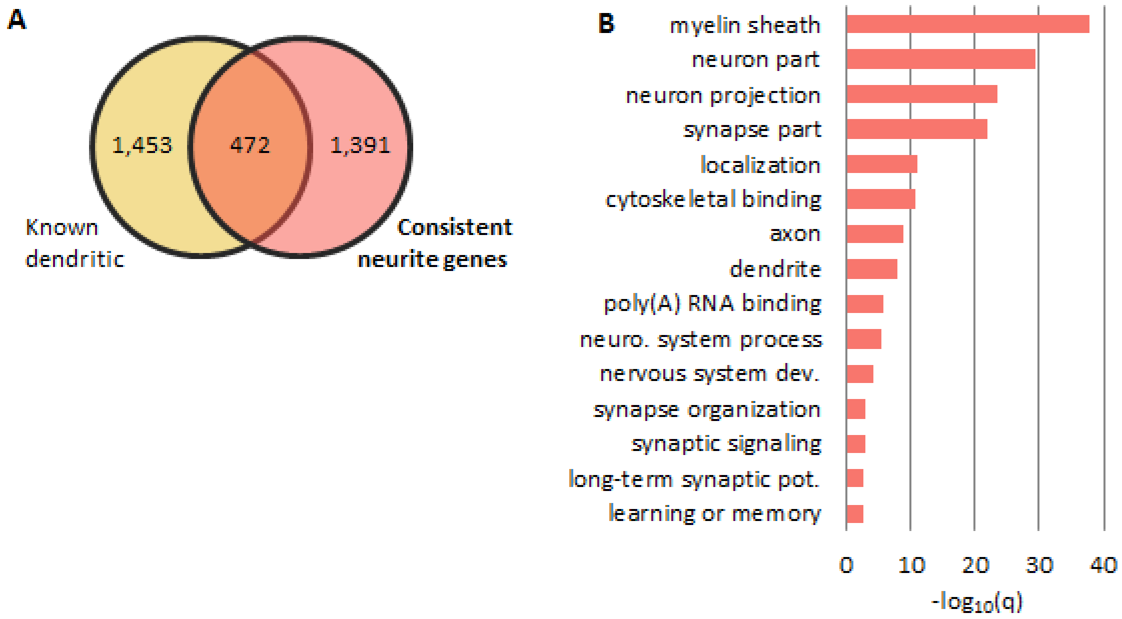

Figure 4-4. Consistently observed genes in the neurites.

(A) Overlap between consistent-neurite genes and the known dendritic genes. (B) Selected GO terms enriched among the consistent-neurite genes.

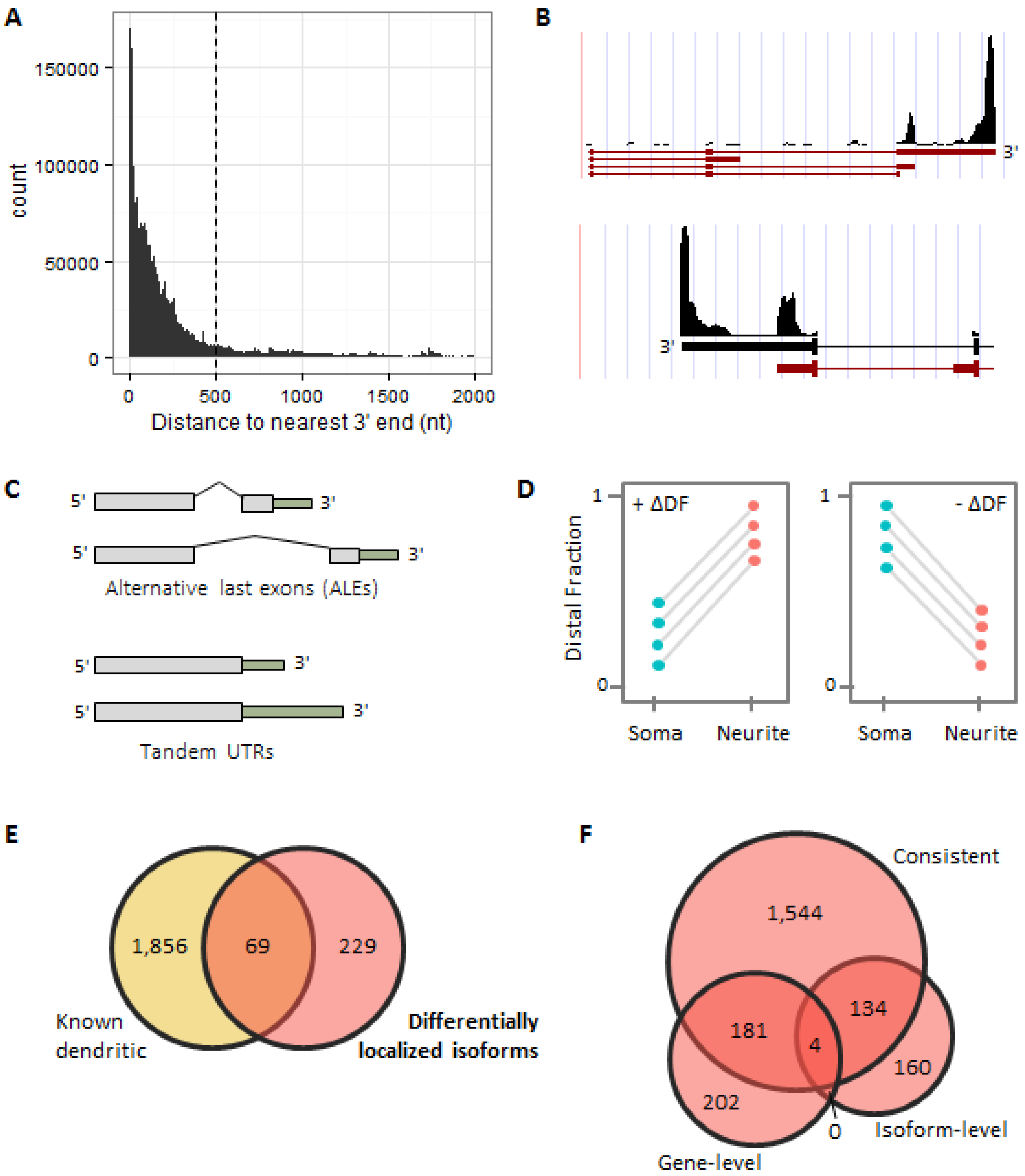

Figure 4-5. Alternative 3'UTR isoform usage in neurons.

(A) Distribution of distance from read ends to the nearest gene 3' end. Most reads are within 500nt of the nearest end (dotted line). (B) Genome browser plots showing read pileups over two genes. Reads show clear peaks marking the 3’ ends. (C) Definition of ALEs and Tandem UTRs. (D) Theoretical examples of genes with consistent changes in distal fraction (ΔDF) across cells, shown as paired plots. Somas and neurites from the same original cell are shown connected by a line. Consistently positive (left) or negative (right) ΔDF indicates differentially localized isoforms between the two compartments. (E) Overlap of differentially localized isoforms with the list of previously annotated dendritic genes. (F) Overlap between the three sets of neurite-localized genes (gene-level, consistent, and isoform-level).

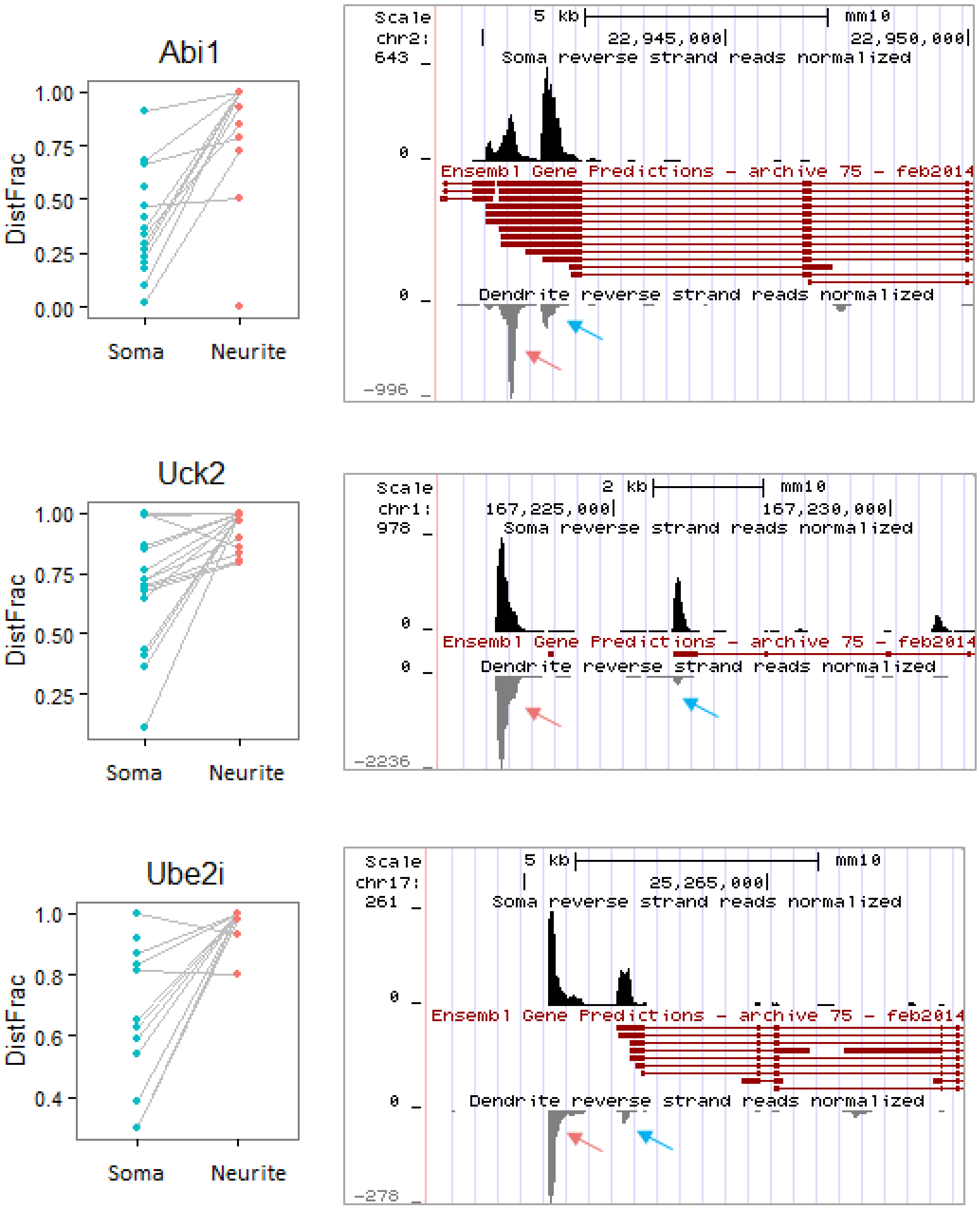

Figure 4-6. Examples of genes with significantly differentially localized 3' isoforms. Paired plots on the left show the DF for each soma-neurite pair (connected by gray lines). The genome browser plots on the right show the read pile-ups for somas (top track; black

peaks) compared to neurites (bottom track; gray peaks; reversed orientation) relative to the annotated gene models from Ensembl (middle track; red). The neurite-preferred 3’ isoform is indicated by a pink arrow, and the non-preferred isoform is indicated by a blue arrow. Note that for Uck2 and Ube2i, the neurite-preferred 3’ isoform is a new isoform from [19] and thus is not part of the Ensembl gene models. All genes shown are on the reverse strand and thus only reverse-strand reads are displayed.

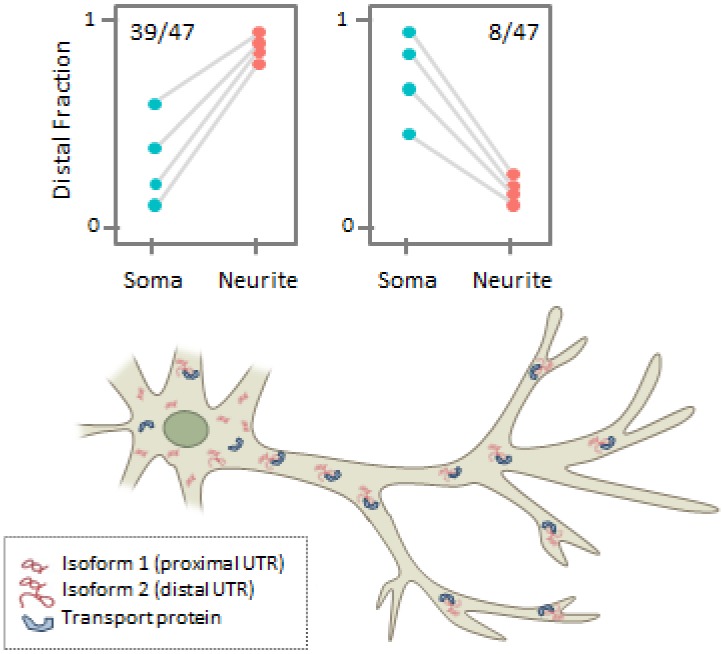

Figure 4-7. The "selective neurite" regulatory pattern.

A large number of differentially localized isoforms showed a pattern where the soma expressed both isoforms at varying levels, but the neurites are selective for only one isoform (top plots). This might be due to e.g. preferentially active transport of the distal isoform (bottom image). The number of genes showing each pattern is shown at the top of the distal fraction plots (out of the 47 showing the selective neurite pattern).

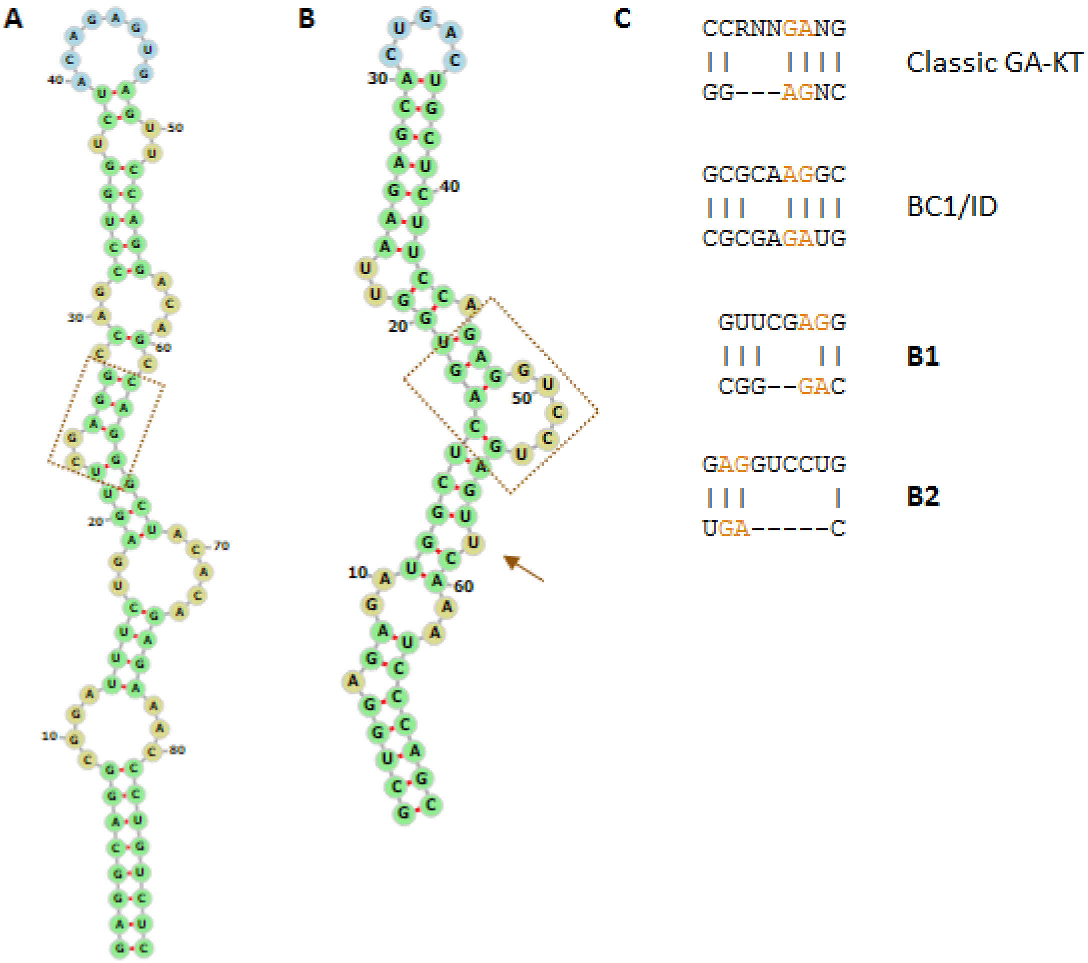

Figure 4-8. Potential GA-KT motifs formed by B1 and B2 SINE hairpins in localized genes.

(A) Consensus structure for the B1 hairpin from a multiple alignment of matches among the localized genes. Structure was modified to show pairing of G-A/A-G at the putative GA-KT motif (dashed box). (B) Same as (A), but for the B2 hairpin. Arrow indicates the U-bulge, similar to the nuclear export signal found in the BC1 hairpin [46,47]. (C)

Comparison of the B1 and B2 putative GA-KT elements with the classic GA-KT and the one found in the BC1/ID element [46,47]. Structure images generated using Forna [73].

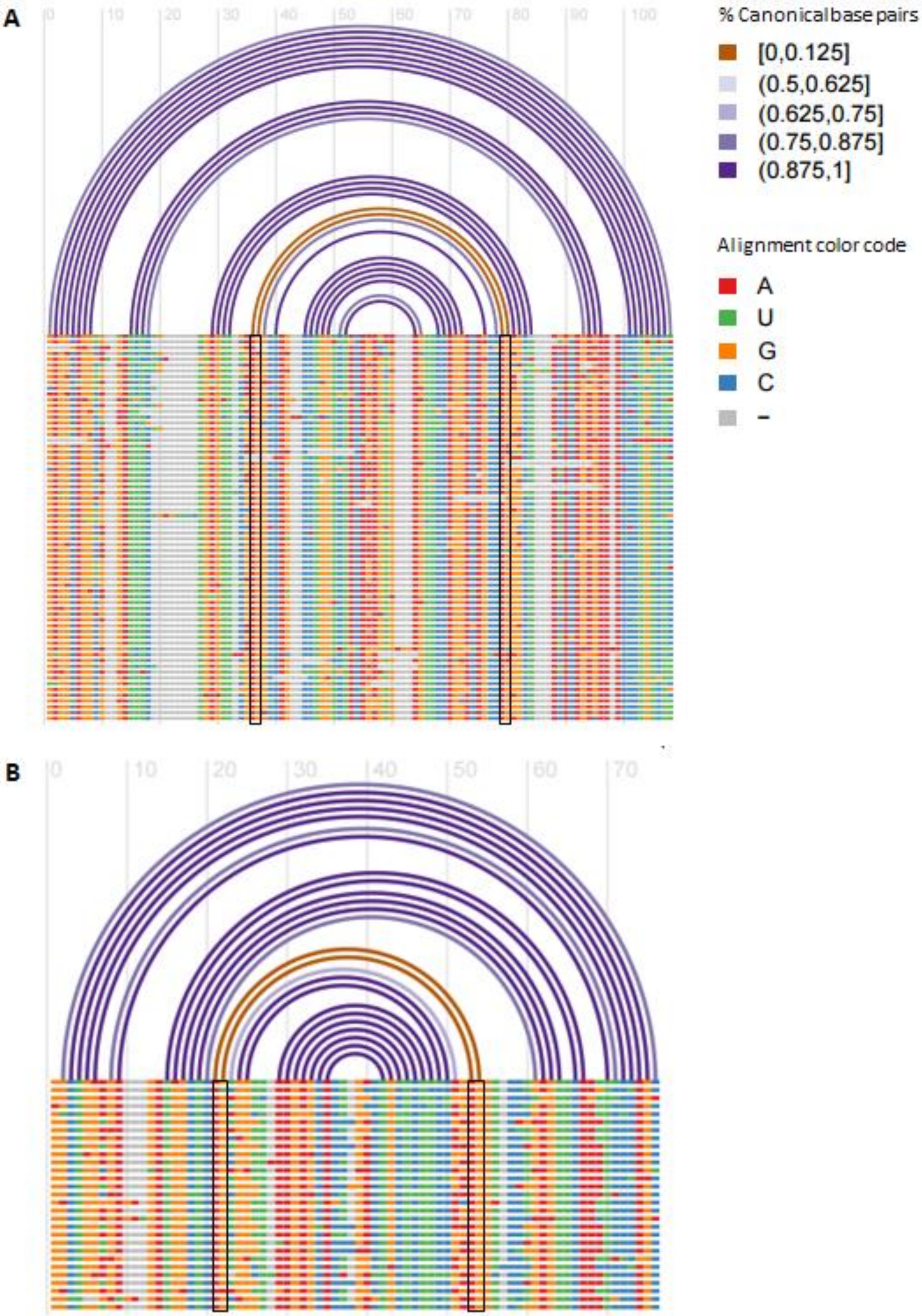
A
0
10
20
30
40
50
60
70
80
90
100
% Canonical base pairs
[0,0.125]
(0.5,0.625]
(0.625,0.75]
(0.75,0.875]
(0.875,1]
Alignment color code
A
U
G
C
–
B
0
10
20
30
40
50
60
70

Figure 4-9. Conserved structure and G-A/A-G pairs in B1 and B2 hairpins in localized genes.

(A) Multiple alignment of instances of the B1 SINE hairpin found in localized genes. All matches from the gene-level list are shown. Arches show predicted paired bases and are colored by percent compatible canonical base pairs. G-A/A-G base pairs are non-canonical and thus the arches for that pair are shown in brown. Boxes show the G-A/A-G positions in the alignment. (B) Same as (A), but for the B2 hairpin. Plots generated using R-chie [74].

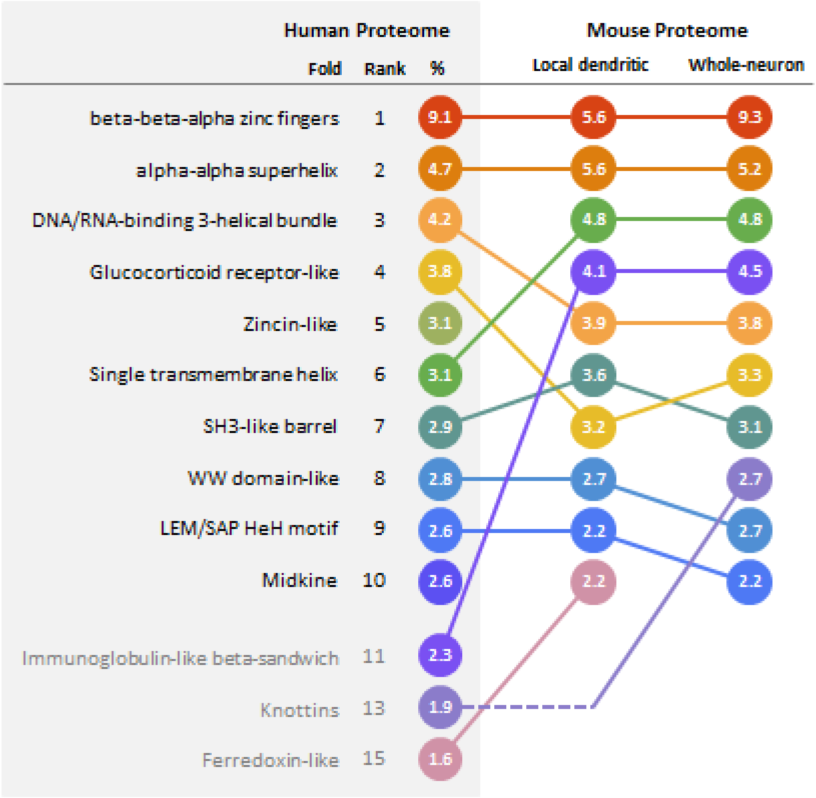

Figure 4-10. Comparison of the most common structural folds represented in different proteome sets.

Folds labeled on the left correspond to the top folds in the human proteome, sorted by rank. The change in rank of each fold from the human proteome to the mouse local proteome (and from the local proteome to the whole-neuron proteome) is indicated by the shifted order of the colored circles, connected by lines. Numbers in circles represent the percent of domains predicted to have that fold in each proteome set. Only high-confidence predictions were used to calculate rank and percentages.

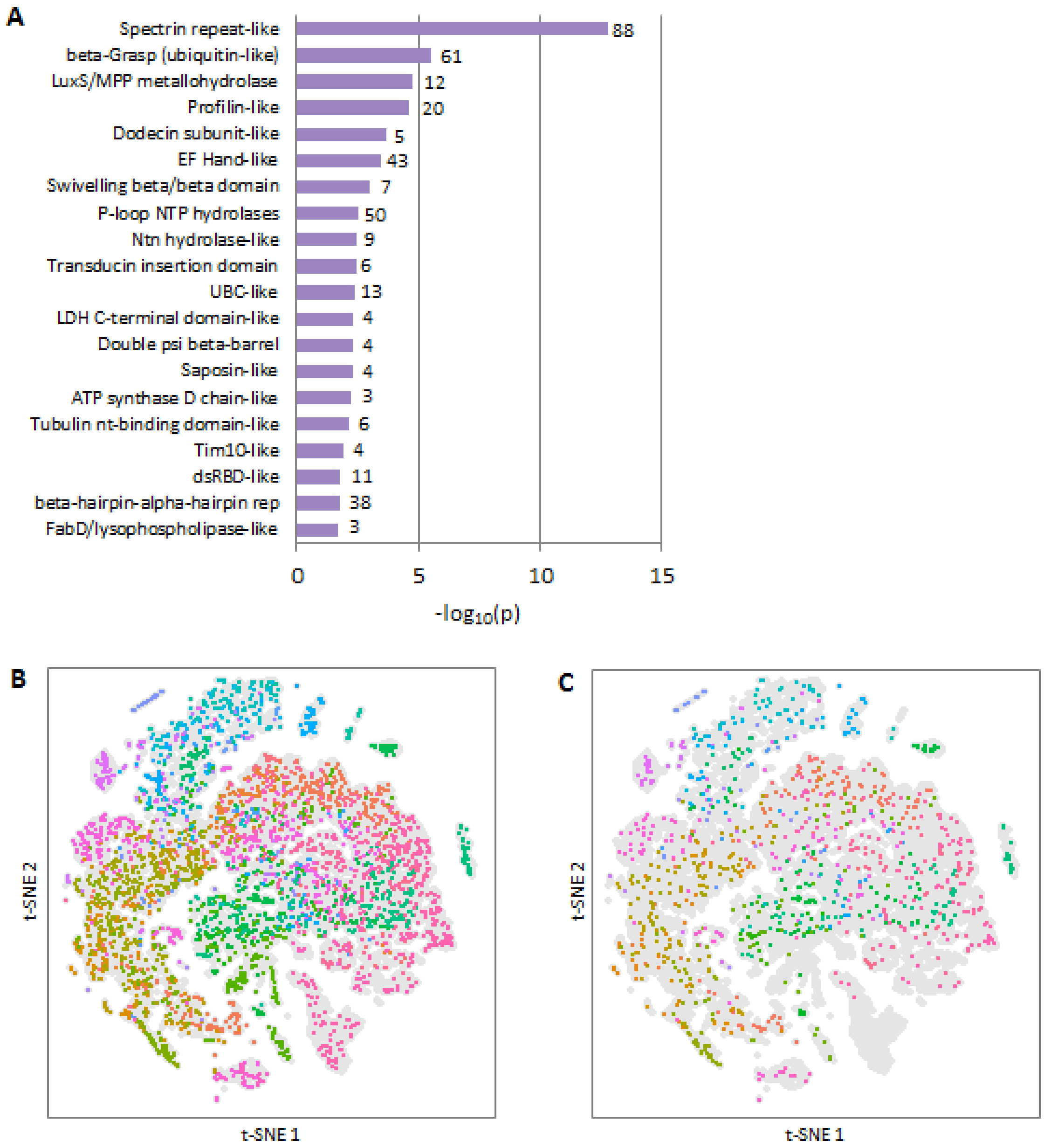

Figure 4-10. Protein structures of the locally-translated proteome.

(A) SCOP folds enriched in the locally translated proteins compared to the neuron-expressed proteins as a whole. The number of predicted domains in the local proteome for each fold is shown to the right of the bar. (B) Two-dimensional representation of the protein structure space occupied by neuronally-expressed protein domains. All neuronally-expressed protein domains are shown in gray in the background, and locally-translated protein domains are shown in the forefront colored by predicted fold (note that multiple folds may have similar colors due to the large number of folds). Locally translated proteins cover most of the structure space spanned by the whole-neuron set. Projection generated by t-Distributed Stochastic Neighbor Embedding (tSNE) of the PESS coordinates of each input domain. (C) Same as (B), but overlaying only the local proteins that overlap the curated list of previously identified dendritic genes.

Table 4-1. Neurite-localized genes based on differential expression.

2010016I18Rik
2010107E04Rik
2010109I03Rik
2810459M11Rik
4833422C13Rik
4930451C15Rik
5031426D15Rik
5830416I19Rik
8430431K14Rik
9330159N05Rik
A430106G13Rik
A630089N07Rik
Acnat2
Aco2
Acsm1
Adamts18
Adap2
Agtrap
AK007420
AK016170
AK020987
AK037411
AK037687
AK042206
AK048887
AK051864
AK053962
AK079994
AK133261
AK134546
AK137566
AK142573
AK142864
AK147589
AK153988
AK154552
AK156971
AK162832
AK163755
AK164124
AK164323
AK169555
AK171391
AK190531
AK206180
Ankef1
Aox3
Apbb1ip
Aqp4
Arhgap31
Atad2
Atp5e
Atp5j2
Atp5k
Atp5l
Atpif1
B430010I23Rik
BC002163
BC051077
BC069931
Bdnf
Bola2
Brsk1
C130026I21Rik
Casp4
Ccdc141
Ccnd1
Ccnd2
Ccni
Cd84
Cdk15
Chrdl1
Col27a1
Colec12
Cox4i1
Cox5b
Cox6a1
Cox6b1
Cox6c
Cox7a2
Cox7b
Cox7c
Cox8a
Ctdspl2
Cyp26b1
Dcdc2a
Ddc
Ddx58
Dock8
DQ072386
Dtx3l
Dusp18
E330033B04Rik
Ebf1
Egf
Ern1
Esr1
Etv4
Exo1
Exph5
Fam101b
Foxp2
Fth1
Ftl1
Gabra4
Gbp7
Gli3
Gltpd2
Gm10012
Gm10033
Gm10059
Gm10073
Gm10076
Gm10221
Gm10222
Gm10263
Gm10275
Gm10443
Gm10485
Gm10621
Gm10689
Gm10712
Gm11249
Gm11273
Gm11343
Gm11407
Gm11408
Gm11410
Gm11477
Gm11478
Gm11512
Gm11531
Gm11808
Gm11942
Gm11956
Gm11960
Gm12013
Gm12020
Gm12034
Gm12155
Gm12295
Gm12338
Gm12517
Gm12618
Gm12778
Gm12903
Gm12936
Gm12976
Gm13192
Gm13215
Gm13339
Gm13340
Gm13341
Gm13421
Gm13433
Gm13488
Gm13722
Gm13826
Gm13857
Gm14303
Gm14450
Gm14539
Gm14586
Gm14667
Gm15393
Gm15462
Gm15536
Gm16238
Gm16416
Gm16418
Gm16432
Gm17529
Gm17821
Gm2000
Gm20469
Gm20541
Gm22567
Gm23134
Gm23368
Gm24105
Gm24514
Gm26461
Gm26870
Gm26909
Gm2830
Gm3550
Gm4853
Gm4986
Gm5963
Gm6265
Gm6378
Gm6525
Gm7331
Gm7618
Gm7866
Gm8019
Gm8129
Gm8292
Gm8317
Gm8649
Gm8730
Gm9006
Gm9843
Gm9901
Gpc6
Gpr35
Grcc10
Gstm1
GU332589
Hic2
Invs
Itga1
Itga4
Itpr2
Jund
Kcng3
Kcnq5
Kctd4
Kif1a
Kif5c
Lcn2
Liph
Lypd1
Malt1
Map1a
Map2
Mapk8ip1
Mavs
Mcf2l
Meis2
Mgst3
Mir682
Mis18bp1
Mre11a
Mrpl33
mt-Rnr1
mt-Rnr2
mt-Td
mt-Te
mt-Tg
mt-Th
mt-Ti
mt-Tk
mt-Tl2
mt-Tm
mt-Tp
mt-Tq
mt-Ts1
mt-Tt
mt-Tw
Myeov2
Ndnf
Ndufa1
Ndufa12
Ndufa2
Ndufa4
Ndufa7
Ndufb11
Ndufb8
Ndufb9
Ndufv3
Necab1
Nhsl2
Nnat
Nrgn
Nsmf
Oaf
Oprd1
Otc
Pate2
Pcdh15
Pde1c
Pde2a
Pdgfrl
Phpt1
Plin3
Pole
Prlr
Prrg1
Prrx1
Psme2b
Ptpn14
Ptprb
Pvalb
Rasgrp4
Rasl10b
Rbm47
Rmi2
Romo1
Rorb
RP23-2C22.3
Rpl12
Rpl12-ps1
Rpl13a
Rpl19
Rpl21
Rpl21-ps12
Rpl21-ps8
Rpl23a
Rpl26
Rpl29
Rpl31
Rpl31-ps8
Rpl32
Rpl34
Rpl35
Rpl36a
Rpl37
Rpl37a
Rpl38
Rpl38-ps2
Rpl39
Rpl39-ps
Rpl41
Rplp0
Rplp1
Rplp2
Rps10-ps2
Rps11
Rps12
Rps12-ps5
Rps12-ps9
Rps16-ps2
Rps17
Rps19
Rps20
Rps21
Rps23
Rps23-ps
Rps24
Rps24-ps3
Rps25
Rps25-ps1
Rps26
Rps26-ps1
Rps28
Rps29
Rps5
Rpsa
Rpsa-ps10
Sepw1
Serhl
Serpina3k
Serpine2
Shank3
Slamf7
Slc17a7
Slc17a9
Slc22a15
Slc23a1
Slc28a3
Slc7a11
Slco1a1
Slfn8
Snhg10
Snhg6
Sp110
Sparc
Srl
Sspn
Syt15
Tcte1
Tfap2b
Tirap
Tmem242
Tnfrsf19
Tomm7
Top2a
Tor4a
Tpmt
Trim56
Trp63
Tulp1
Uba52
Ugt1a6a
Uqcr10
Uqcr11
Uqcrh
Uqcrq
Usmg5
Vangl1
Vav3
Wdr31
Ybx1
Zbtb20
Zfhx3
Zscan20

Table 4-2. Consistently observed genes in the neurites.

0610012G03Rik
1110001J03Rik
1110002L01Rik
1110008F13Rik
1110008P14Rik
1110065P20Rik
1700020I14Rik
1700025G04Rik
1810043H04Rik
2010003O02Rik
2010107E04Rik
2210016L21Rik
2410006H16Rik
2410015M20Rik
2610017I09Rik
2610507B11Rik
2700029M09Rik
2700094K13Rik
2900011O08Rik
2900097C17Rik
4932438A13Rik
5330434G04Rik
5730455P16Rik
6030419C18Rik
6430548M08Rik
A030009H04Rik
A830010M20Rik
A830039N20Rik
Aak1
Aar2
Aars
Aasdhppt
AB347151
Abat
Abca3
Abca5
Abce1
Abhd17a
Abhd6
Abhd8
Abi2
Abr
AC149090.1
Acadsb
Acat2
Aco2
Acot7
Acp1
Acsl4
Acsl6
Acss2
Actb
Cacng2
Cadm1
Cadps
Calm1
Calm2
Calm3
Caly
Camk2b
Camk2d
Camk2g
Camk2n2
Camkk2
Camsap1
Camta1
Cand1
Canx
Capns1
Capzb
Casc4
Caskin1
Cbx5
Cbx6
Cby1
Ccdc104
Ccdc124
Ccdc127
Ccdc50
Ccdc88a
Ccnc
Ccnd2
Ccni
Ccny
Ccpg1
Ccser2
Cct2
Cct3
Cct8
Cdadc1
Cdc37
Cdc37l1
Cdc42
Cdc42bpa
Cdc42se2
Cdipt
Cdk14
Cdk16
Cdk4
Cdk5
Cdk5r1
Cdk5r2
Cdkn1b
Cdr1
Elk1
Elmo1
Elovl6
Elp5
Emc10
Enah
Enc1
Eno1
Eno2
Enpp5
Ensa
Eny2
Epb4.1l1
Epb4.1l3
Epha5
Epha6
Epm2aip1
Epn1
Eps15
Erbb4
Erc1
Erlec1
Etnk1
Evl
Ewsr1
Exoc5
Exoc6b
Exoc8
F830016B08Rik
Fabp3
Fam115a
Fam120a
Fam13c
Fam155a
Fam168a
Fam168b
Fam174a
Fam195b
Fam19a5
Fam210b
Fam219a
Fam49a
Fam63b
Fam73a
Fam73b
Fam84a
Fam96b
Fasn
Fau
Faxc
Fbxl16
Fbxo21
Gnal
Gnao1
Gnaq
Gnas
Gnb1
Gnb2l1
Gng2
Gng3
Gnl1
Gorasp2
Got1
Got2
Gpi1
Gpm6a
Gpm6b
Gpr162
Gprasp1
Gpx1
Gpx4
Grb10
Grcc10
Gria1
Gria2
Grin1
Grin2b
Grin3a
Grina
Grip1
Grk6
Grlf1
Grm5
Grpel1
Gsk3b
Gstm5
GU332589
Guk1
H2afz
Habp4
Hadhb
Hapln1
Hars
Haus2
Hcfc1r1
Hcn1
Hdac5
Hdac9
Hdgf
Hdgfrp3
Hdhd2
Herc1
Herc2
Higd1a
Mrpl43
Mrpl51
Mrpl52
Mrpl9
Mrps14
Mrps18a
Msi2
Mt1
Mt3
Mtch2
Mtdh
Mtf1
Mtif2
Mtmr9
mt-Rnr1
mt-Rnr2
Mtss1l
mt-Td
mt-Te
mt-Th
mt-Ti
mt-Tm
mt-Tp
mt-Tq
mt-Tt
mt-Tw
Mvb12b
Myeov2
Myl12b
Myl6
Myo5a
Myt1l
Naa60
Nap1l5
Napa
Napb
Nav1
Nav2
Nav3
Ncald
Ncam1
Ncaph2
Ncl
Ncoa2
Ncor1
Ncs1
Ndfip1
Ndn
Ndrg3
Ndrg4
Ndufa1
Ndufa10
Ppp2r2c
Ppp2r5b
Ppp3ca
Ppp6c
Pptc7
Prdx1
Prdx2
Prdx3
Prdx5
Prelid1
Prkaa2
Prkaca
Prkar1a
Prkar1b
Prkca
Prmt5
Prpf19
Prpf38b
Prrc2b
Prrc2c
Psap
Psd
Psma3
Psma7
Psmb1
Psmb4
Psmb7
Psmc3
Psmc5
Psmd11
Psmd2
Psmd3
Psmd4
Psmd8
Ptchd4
Ptdss2
Pten
Ptges3
Ptma
Ptms
Ptp4a2
Ptpn4
Ptpn5
Ptprd
Ptprs
Pum2
Pura
Purb
Purg
Pvalb
Pvrl3
Pxmp4
Sdhb
Sdhc
Sdhd
Sec11c
Sec23a
Sec23b
Sec24a
Sec62
Sel1l
Selk
Selm
Selt
Senp2
Sept11
Sept3
Sept5
Sept7
Sepw1
Serbp1
Serf2
Serinc1
Serinc3
Serp2
Set
Setd7
Sez6l2
Sfi1
Sfxn1
Sfxn3
Sgta
Sh3bgrl3
Sh3bp5l
Sh3gl2
Sh3glb2
Shank2
Shank3
Shc3
Shfm1
Sike1
Sipa1l1
Ski
Skp1a
Slc1a1
Slc1a2
Slc22a17
Slc25a12
Slc25a22
Slc25a23
Slc25a3
Slc25a4
Slc25a5
Slc25a51
Tusc3
Txn1
Txndc15
Txndc16
Txnl1
Txnl4a
Uba52
Ubash3b
Ubb
Ubc
Ube2d2a
Ube2d3
Ube2e2
Ube2h
Ube2l3
Ube2m
Ube2n
Ube2ql1
Ube2r2
Ube2z
Ube3a
Ubfd1
Ubl3
Ubl4
Ubl5
Ubqln1
Ubqln2
Ubr3
Ubxn2a
Uchl1
Uck2
Ufc1
Ufm1
Uhmk1
Uhrf1bp1l
Uhrf2
Ulk2
Ulk4
Unc5c
Uqcc2
Uqcr10
Uqcr11
Uqcrb
Uqcrc1
Uqcrc2
Uqcrfs1
Uqcrh
Uqcrq
Usf2
Usmg5
Usp22
Usp32

Actg1
Actr1a
Acyp2
Adam22
Adarb1
Adcy5
Add1
Add2
Adipor2
Adrbk2
Aes
Aff4
Agap1
Agap3
Agtpbp1
Ahcyl1
Ahcyl2
AI413582
AI593442
Aig1
Aip
AK007420
AK021280
AK035770
AK078656
Ak1
AK157302
AK164124
AK181773
AK182655
AK186242
AK190531
AK196308
AK201505
AK207499
AK208404
AK217941
Akap11
Akap6
Akr1a1
Aktip
AL591209.1
Aldh5a1
Aldoa
Alkbh6
Alyref
Amd2
Amph
Anapc11
Anapc16
Anapc5
Angel2
Ank1
Ank2
Ank3
Ankfy1
Anp32a
Celf2
Celf4
Cend1
Cenpb
Cep97
Cerk
Cfl1
Cfl2
Chchd10
Chchd2
Chchd6
Chd3
Chd4
Chl1
Chn1
Chp1
Chpt1
Chst2
Chtop
Churc1
Cic
Cisd1
Cited2
Ckb
Ckmt1
Clasp1
Clcn3
Clec2l
Clip3
Clip4
Clpb
Clpp
Clstn1
Clta
Cltb
Cmip
Cmpk1
Cnbp
Cnih2
Cnot4
Cntn1
Coa3
Col4a4
Comt
Copa
Cope
Cops6
Coq10a
Coro1c
Coro2b
Cox14
Cox17
Cox4i1
Cox5a
Cox5b
Cox6a1
Cox6a2
Fbxo9
Fbxw11
Fbxw2
Fdps
Fem1b
Fez1
Fgf12
Fgf13
Fgf9
Fh1
Fign
Fkbp1a
Flrt2
Foxg1
Foxn3
Foxp1
Frmpd4
Fscn1
Fth1
Ftl1
Fto
Fubp1
Fus
Fut9
G3bp2
Gabarap
Gabarapl1
Gabarapl2
Gabbr1
Gabrb2
Gabrb3
Gabrg2
Gad1
Gad2
Gan
Gap43
Gapdh
Garnl3
Gas5
Gatad1
Gatsl2
Gbas
Gclm
Gcsh
Gda
Gdap1
Gdi1
Gfod1
Gfpt1
Ggps1
Ghitm
Gid8
Glo1
Glrb
Gls
Gm10012
Gm10039
Higd2a
Hint1
Hip1
Hjurp
Hk1
Hmbox1
Hmgb1
Hmgcs1
Hn1
Hnrnpa1
Hnrnpa2b1
Hnrnpa3
Hnrnpab
Hnrnpk
Hnrnpu
Homer1
Hras
Hsbp1
Hsd17b12
Hsp90aa1
Hsp90ab1
Hspa4
Hspa4l
Hspa5
Hspa8
Hspd1
Hspe1
Huwe1
Hypk
Id2
Ide
Idh3a
Idh3b
Idh3g
Ids
Ier3ip1
Ifngr2
Igfbp2
Immt
Impa1
Impact
Ina
Inpp4a
Inpp5f
Ip6k1
Ipo5
Ipo7
Ipp
Ireb2
Irf2bpl
Isca1
Itsn1
Jmjd8
Jph4
Jund
Kansl1
Kbtbd2
Ndufa11
Ndufa12
Ndufa13
Ndufa2
Ndufa3
Ndufa4
Ndufa5
Ndufa6
Ndufa7
Ndufa8
Ndufab1
Ndufaf7
Ndufb10
Ndufb11
Ndufb2
Ndufb3
Ndufb4
Ndufb5
Ndufb6
Ndufb7
Ndufb8
Ndufb9
Ndufc1
Ndufc2
Ndufs1
Ndufs2
Ndufs4
Ndufs5
Ndufs6
Ndufs7
Ndufs8
Ndufv1
Ndufv2
Ndufv3
Necab2
Nedd4
Nedd8
Nefh
Nefl
Nefm
Nek7
Nell2
Nemf
Nenf
Nfe2l1
Nfia
Nfib
Nfix
Nfkb2
Ngfrap1
Nipsnap1
Nisch
Nkiras1
Nlgn1
Nlgn2
Nmd3
Nme1
Rab1
Rab10
Rab11b
Rab11fip4
Rab12
Rab28
Rab2a
Rab39b
Rab3a
Rab3b
Rab3c
Rab5b
Rab5c
Rab6a
Rab6b
Rabac1
Rabgap1l
Rac1
Rad21
Rad23a
Ranbp1
Rangap1
Rapgef4
Rasl10b
Rbfox1
Rbfox2
Rbm14
Rbms3
Rbx1
Rc3h1
Rc3h2
Reep5
Rell2
Reln
Rer1
Rfc5
Rfng
Rfx7
Rgs7bp
Rhbdd2
Rheb
Rhot1
Rims1
Rmnd5a
Rnasek
Rnd2
Rnf10
Rnf130
Rnf14
Rnf157
Rnf165
Rnf187
Rnf208
Rnf44
Rnf5
Rnf7
Robo2
Slc2a13
Slc30a9
Slc32a1
Slc35f1
Slc38a1
Slc3a2
Slc48a1
Slc4a1ap
Slc6a1
Slc8a1
Slfn8
Slirp
Slitrk5
Smap1
Smarca2
Smdt1
Smek2
Smim13
Smim14
Snap25
Snap47
Snca
Sncb
Snf8
Snhg11
Snhg6
Snrpn
Snx12
Snx27
Socs2
Sod1
Soga3
Sorbs2
Sos2
Sox2ot
Sparcl1
Spats2l
Sphk2
Spin1
Spock2
Spred2
Sprn
Spryd7
Sptan1
Sptbn1
Sptbn2
Sqstm1
Srcin1
Srebf2
Srgap3
Srp14
Srp72
Srr
Ssh2
Ssr1
St13
St8sia3
Usp34
Usp50
Vamp2
Vapa
Vapb
Vcp
Vdac1
Vdac2
Vegfb
Vgf
Vps26b
Vps35
Vps37a
Vsnl1
Vstm2a
Wac
Wasf3
Wbp11
Wbp2
Wdfy1
Wdfy3
Wdr13
Wdr18
Wdr45b
Wdr89
Whsc1
Whsc1l1
Wipi2
Wsb2
Xiap
Xpo7
Xpr1
Ybx1
Ykt6
Yod1
Ypel3
Ywhab
Ywhae
Ywhag
Ywhah
Ywhaq
Ywhaz
Zbtb20
Zbtb4
Zbtb7a
Zc3h15
Zc3h7b
Zcchc17
Zcchc18
Zcrb1
Zeb2
Zfand5
Zfp260
Zfp60
Zfp931
Zfr
Zmat3

Ap1s1
Ap1s2
Ap2b1
Ap2m1
Ap2s1
Ap3m1
Ap3s1
Ap3s2
Ap4s1
Apba1
Apbb1
Apc
Aplp1
Aplp2
Apopt1
App
Appl1
Araf
Arap2
Arcn1
Arel1
Arf1
Arf3
Arf4
Arf5
Arfip2
Arhgdia
Arhgef4
Arhgef9
Arl2bp
Arl3
Arl4c
Arl5a
Arl5b
Arl6ip1
Arl8a
Armc1
Armcx1
Armcx2
Arnt2
Arpc1b
Arpc2
Arpc5
Arpc5l
Arrb1
Arx
Asns
Asph
Asxl2
Atf2
Atf5
Atg12
Atn1
Atox1
Atp13a2
Atp1a3
Atp1b1
Cox6b1
Cox6c
Cox7a2
Cox7a2l
Cox7b
Cox7c
Cox8a
Cpe
Cpeb2
Cplx1
Cpsf6
Crbn
Crk
Crlf2
Crmp1
Crtac1
Cs
Csdc2
Csde1
Csf2ra
Csnk1d
Csnk1g1
Csnk2a1
Csrnp3
Cst3
Ctage5
Ctbp1
Ctdspl2
Ctnnb1
Ctnnbip1
Ctsb
Cuedc2
Cux1
Cxx1a
Cxx1b
Cxx1c
Cyb5b
Cycs
Cyfip2
Cyhr1
D17Wsu104e
D17Wsu92e
D3Bwg0562e
D3Ertd254e
D5Ertd579e
D8Ertd738e
Dab1
Dact3
Dbi
Dcaf10
Dcaf7
Dcdc2a
Dclk1
Dctn2
Dctn3
Dcun1d5
Dda1
Gm10053
Gm10073
Gm10076
Gm10086
Gm10123
Gm10136
Gm10169
Gm10175
Gm10186
Gm10221
Gm10222
Gm10240
Gm10250
Gm10263
Gm10275
Gm10288
Gm10443
Gm10689
Gm11223
Gm11249
Gm11273
Gm11343
Gm11361
Gm11407
Gm11410
Gm11477
Gm11478
Gm11512
Gm11633
Gm11808
Gm11942
Gm11966
Gm12141
Gm12191
Gm12254
Gm12337
Gm12338
Gm12350
Gm12481
Gm12497
Gm12715
Gm12903
Gm12918
Gm12976
Gm13186
Gm13192
Gm13339
Gm13340
Gm13341
Gm13456
Gm13488
Gm13680
Gm13826
Gm14088
Gm14165
Gm14303
Gm14305
Kbtbd3
Kcmf1
Kcna1
Kcna2
Kcng3
Kcnh7
Kcnq1ot1
Kctd16
Kctd17
Kdm2a
Kif1a
Kif1b
Kif21a
Kif21b
Kif3a
Kif3c
Kif5a
Kif5b
Kif5c
Klc1
Klc2
Klf13
Klf7
Klf9
Klhdc10
Kmt2e
Kpna6
Kras
Krtcap2
Lamp1
Lamp2
Lamtor1
Lamtor4
Large
Larp1
Lars2
Lbh
Ldha
Ldhb
Letm1
Lgr5
Lhfpl4
Lhx6
Lias
Limk1
Lin7a
Lman2
Lmo4
Lpgat1
Lphn1
Lrrc4b
Lrrc4c
Lsamp
Lsm12
Lsmd1
Luc7l2
Lynx1
Nme2
Nme7
Nmnat2
Nmt2
Nnat
Nop10
Nop58
Nos1ap
Npc2
Npepps
Npm1
Nrxn1
Nrxn2
Nrxn3
Nsf
Nsg1
Nsg2
Nsmf
Nt5dc3
Ntan1
Ntrk2
Ntrk3
Nucks1
Nudc
Nudcd3
Nudt19
Nudt21
Nudt3
Nudt4
Nufip2
Nus1
Nxf1
Nyap2
Oat
Oaz1
Oaz2
Ociad2
Ogdh
Ogfrl1
Olfm1
Opa1
Opa3
Osbpl2
Oscp1
Otc
Otub1
Oxct1
Oxr1
Pabpc1
Pabpn1
Pacsin1
Pafah1b1
Paip2
Pak7
Palm
Pam
Papola
Rogdi
Romo1
Rora
RP23-199B2.4
Rpgrip1
Rpl10
Rpl10a
Rpl10a-ps1
Rpl10-ps3
Rpl11
Rpl12
Rpl13
Rpl13a
Rpl14
Rpl15
Rpl17
Rpl17-ps5
Rpl18
Rpl18a
Rpl18-ps1
Rpl18-ps2
Rpl19
Rpl19-ps11
Rpl21
Rpl21-ps8
Rpl22
Rpl22l1
Rpl23
Rpl23a
RPL24
Rpl26
Rpl27
Rpl27a
Rpl28
Rpl28-ps1
Rpl29
Rpl3
Rpl30
Rpl30-ps10
Rpl31
Rpl31-ps8
Rpl32
Rpl34
Rpl34-ps1
Rpl35
Rpl35a
Rpl35a-ps2
Rpl36
Rpl36a
Rpl36a-ps1
Rpl37
Rpl37a
Rpl38
Rpl38-ps1
Rpl38-ps2
Rpl39
Rpl39-ps
Stam
Stau2
Stk11
Stk25
Stmn1
Stmn2
Stmn3
Stox2
Stx1b
Stxbp1
Sub1
Sult4a1
Sumo1
Supt4a
Suv420h1
Sv2a
Svop
Swi5
Sybu
Syn1
Syn2
Syncrip
Syngr1
Synj1
Synj2bp
Syt1
Syt11
Taf10
Taf13
Tanc2
Taok1
Taok3
Tatdn1
Tax1bp1
Tbc1d24
Tbca
Tbcb
Tceb1
Tceb2
Tcf12
Tcf4
Tcte1
Tef
Tex2
Tfg
Tfrc
Thra
Thy1
Timm10
Timm10b
Timm13
Timm17a
Timm17b
Timm8b
Tlcd1
Tma7
Tma7-ps
Zmynd11
Znrf1
Zwint
Zyg11b

Atp2a2
Atp5a1
Atp5b
Atp5c1
Atp5d
Atp5e
Atp5f1
Atp5g1
Atp5g2
Atp5g3
Atp5h
Atp5j
Atp5j2
Atp5k
Atp5l
Atp5l2
Atp5o
Atp6ap1
Atp6ap2
Atp6v0a1
Atp6v0d1
Atp6v0e2
Atp6v1a
Atp6v1b2
Atp6v1c1
Atp6v1d
Atp6v1e1
Atp6v1f
Atp6v1g1
Atp6v1g2
Atp9a
Atpif1
Atxn1
Atxn10
Atxn2
Atxn7l3b
AU019823
Auh
AY036118
B230219D22Rik
B3gat1
B3gat2
B4galt6
Baalc
Bag1
Basp1
BC002163
BC005537
BC021618
BC029214
BC029722
BC031181
BC069931
Bcar1
Bcas2
Bcat1
Bcl11a

Ddah1
Ddx1
Ddx3x
Ddx5
Deaf1
Deb1
Def8
Degs2
Dennd5a
Dennd5b
Desi1
Dgcr6
Dgkg
Dhx15
Dhx9
Diras1
Disp2
Dlc1
Dld
Dlg2
Dlg4
Dlgap1
Dlgap2
Dlgap4
Dlst
Dlx1os
Dlx6os1
Dmd
Dnaaf2
Dnajb14
Dnajb6
Dnajc27
Dnajc5
Dnajc6
Dner
Dnmt3a
Dock8
Dos
Dpp3
Dpp8
DQ690118
Drap1
Drg1
Dtna
Dtx3
Dusp8
Dvl1
Dvl3
Dync1h1
Dync1li2
Dynll1
Dynll2
Dynlrb1
Dynlt1a
Dynlt1-ps1
Dynlt3
Dzank1

Gm14326
Gm14399
Gm14450
Gm14539
Gm14586
Gm14633
Gm14794
Gm15421
Gm15427
Gm15459
Gm15487
Gm15500
Gm15501
Gm15536
Gm15772
Gm15920
Gm16418
Gm1673
Gm17257
Gm17383
Gm1821
Gm2000
Gm23134
Gm2382
Gm24105
Gm26384
Gm26461
Gm26582
Gm26631
Gm26870
Gm26909
Gm26924
Gm2830
Gm2962
Gm3244
Gm3362
Gm3550
Gm4117
Gm4149
Gm4459
Gm4707
Gm4735
Gm4853
Gm5121
Gm5384
Gm5436
Gm5506
Gm5514
Gm5526
Gm5566
Gm5601
Gm5805
Gm5844
Gm5963
Gm6136
Gm6180
Gm6222

Lyrm9
Macf1
Maf
Mafg
Maged1
Magee1
Magi1
Map1a
Map1b
Map1lc3a
Map1lc3b
Map2
Map2k2
Map2k4
Map3k10
Map3k12
Map4
Map7d1
Mapk1
Mapk10
Mapk3
Mapk6
Mapk8ip1
Mapk8ip3
Mapk9
Mapre1
Mapre2
Mapt
March5
Marcks
Mau2
Mbd5
Mbnl2
Mboat7
Mcf2l
Mctp1
Mdga2
Mdh1
Mdh2
Me3
Mea1
Mecp2
Med13
Mef2c
Meg3
Megf11
Mff
Mfn2
Mga
Mgll
Mgrn1
Mgst3
Mia3
Mical2
Mid1
Mien1
Mif

Parp6
Parva
Pbx1
Pcbp2
Pcdh17
Pcif1
Pcmt1
Pcmtd1
Pcsk1n
Pdcd5
Pdcd6
Pde11a
Pde4a
Pde4d
Pdgfa
Pdha1
Pdhx
Pdpk1
Pdxk
Pea15a
Pebp1
Peg3
Pfdn1
Pfdn2
Pfdn5
Pfkm
Pfkp
Pfn1
Pfn2
Pgam1
Pgam1-ps2
Pggt1b
Pgk1
Pgk1-rs7
Pgp
Phactr1
Phactr3
Phb
Phpt1
Phyhipl
Phykpl
Pi4ka
Pigq
Pik3ca
Pip4k2b
Pip5k1a
Pip5k1c
Pitpna
Pitpnc1
Pja2
Pkp4
Plekhb2
Plin3
Plxdc2
Pmpca
Pmvk
Pnkd

Rpl3-ps1
Rpl4
Rpl41
Rpl5
Rpl6
Rpl7
Rpl7a
Rpl8
Rpl9
Rpl9-ps6
Rplp0
Rplp1
Rplp2
Rprd2
Rps10
Rps10-ps2
Rps11
Rps11-ps1
Rps12
Rps12-ps9
Rps13
Rps13-ps1
Rps13-ps2
Rps14
Rps15
Rps15a
Rps15a-ps6
Rps16
Rps16-ps2
Rps17
Rps18
Rps19
Rps19-ps6
Rps2
Rps20
Rps21
Rps23
Rps23-ps
Rps24
Rps24-ps3
Rps25
Rps25-ps1
Rps26
Rps26-ps1
Rps27a
Rps28
Rps29
Rps3
Rps3a1
Rps4x
Rps5
Rps6
Rps6kb1
Rps6-ps4
Rps7
Rps8
Rps9

Tmem130
Tmem132b
Tmem135
Tmem14c
Tmem151b
Tmem167
Tmem170b
Tmem178b
Tmem179
Tmem184c
Tmem234
Tmem242
Tmem245
Tmem256
Tmem258
Tmem259
Tmem29
Tmem30a
Tmem41b
Tmem50b
Tmem55a
Tmem55b
Tmem59l
Tmem66
Tmod2
Tmsb10
Tmsb4x
Tmx4
Tnks2
Tnpo1
Tnrc6a
Tom1l2
Tomm20
Tomm40l
Tomm5
Tomm6
Tomm7
Top1
Tox4
Tpi1
Tpm1
Tppp
Tpt1
Tpt1-ps3
Trak1
Trappc13
Trappc2l
Trerf1
Trim2
Trim32
Trim35
Trim37
Trim44
Trim8
Trim9
Trip4
Trnp1

Bcl11b	E330033B04Rik	Gm6265	Minos1	Pnpla8	Rpsa	Trove2
Bcl2l2	Edf1	Gm6378	Mir703	Poldip2	Rpsa-ps10	Trp53bp1
Bdh1	Eef1a1	Gm6444	Mit1/Lb9	Polr1d	Rpusd4	Trp53inp2
Bdnf	Eef1a2	Gm6472	Mkln1	Polr2g	Rraga	Trpc4ap
Becn1	Eef1b2	Gm6807	Mkrn1	Polr2l	Rtcb	Trpm3
Bend6	Eef1g	Gm6822	Mlf2	Polr2m	Rtn1	Trub2
Bex1	Eef2	Gm6977	Mllt11	Polr3h	Rtn2	Tsc22d1
Bex2	Efcab2	Gm7312	Mmd	Pomp	Rtn3	Tsc22d2
Bicd1	Efhd2	Gm7331	Mmp16	Ppargc1a	Rtn4	Tsn
Bnip3l	Ehd3	Gm7536	Mmp24	Ppargc1b	Rufy3	Tsnax
Bola2	Eid1	Gm8129	Morf4l2	Ppdpf	Rundc3a	Tspan13
Braf	Eif1	Gm8292	Mpc1	Ppia	Rusc1	Tspan3
Brd2	Eif1b	Gm8430	Mpc1-ps	Ppig	Rwdd4a	Tspan7
Brd4	Eif3f	Gm8566	Mpc2	Ppip5k1	Sap18	Tspyl4
Brd7	Eif3h	Gm8623	Mpnd	Ppm1e	Sar1a	Ttbk2
Bre	Eif3i	Gm8730	Mpp3	Ppm1h	Sbk1	Ttc3
Bri3bp	Eif3k	Gm9385	Mpv17l	Ppme1	Sc4mol	Ttc7b
Brk1	Eif4a1	Gm9703	Mrfap1	Ppp1cb	Scamp5	Ttc9b
Brox	Eif4a2	Gm9769	Mrp63	Ppp1r12a	Scd2	Ttl
Brsk1	Eif4e	Gm9790	Mrpl10	Ppp1r1a	Scn1b	Ttll7
Btbd1	Eif4e2	Gm9800	Mrpl17	Ppp1r1c	Scn2a1	Tuba1a
Btf3	Eif4g2	Gm9843	Mrpl27	Ppp1r2	Scn2b	Tubb2a
Bzw1	Eif4g3	Gm9846	Mrpl30	Ppp1r7	Scn8a	Tubb2b
Bzw2	Eif4h	Gmfb	Mrpl33	Ppp1r9b	Scoc	Tubb3
C530008M17Rik	Eif5a	Gna12	Mrpl34	Ppp2ca	Scrt1	Tubb4a
Cabp1	Elavl2	Gnai1	Mrpl36	Ppp2cb	Sdha	Tubb5
Cacnb4	Elavl3	Gnai2	Mrpl42	Ppp2r1a	Sdhaf2	Tulp4

Table 4-3. Genes with differentially localized 3’UTR isoforms.

2410004B18Rik
2700029M09Rik
6430548M08Rik
A530058N18Rik
A830018L16Rik
Aak1
Abhd16a
Abi1
AC149090.1
Acly
Acss2
Actg1
Actr2
Ahcyl2
Amdhd2
Amfr
Amph
Ank2
Ankfy1
Anp32e
Ap2a2
Ap2m1
Ap3b2
Apbb2
Arfgap1
Arid1a
Arid2
Arl1
Arl16
Asnsd1
Atp5a1
Atp5f1
Atp5g1
Atp5h
Atp6v1b2
Atxn7l3b
Bach1
BC003331
BC005537
Bcas2
Bcl11a
Bdh1
Bex1
Bloc1s1
Blzf1
Bsg
Btf3
Cacfd1
Calm3
Camk2b
Capzb
Cbx5
Ccdc47
Ccl27a
Ccndbp1
Cd99l2
Cdc123
Cdc42
Cdh13
Cetn2
Chka
Chmp3
Cnbp
Cnot6l
Cog7
Commd7
Copg1
Cops6
Csnk1d
Csnk2b
Cul1
Cxxc4
Cyb5
Cycs
D4Wsu53e
Dctn3
Dctn5
Dhdds
Dhx30
Dos
Drg1
Dync1i2
Dynll2
E2f6
Ehmt2
Eif2ak1
Emc4
Emc7
Enah
Esf1
Evi5l
Fam171a1
Fam229b
Fam81a
Farsa
Fbxo31
Fbxo44
Fgd4
Flot2
Fscn1
Galntl6
Glud1
Gm14204
Gm15459
Gnai1
Gnao1
Gnb1
Gps1
H2afy
Haghl
Hdac5
Hint3
Hnrnpm
Hnrnpu
Hsd17b12
Hsp90aa1
Hspa8
Ift57
Inpp4a
Inpp5e
Itpa
Jtb
Kalrn
Kcnq2
Kpna1
Lamtor2
Ldha
Lrrc4c
Lsm3
Lyrm5
Lysmd4
Maged2
Map1lc3b
Map2
Map2k4
Map4
Mapk8ip2
Mast1
Megf11
Mettl2
Mfap3l
Minos1
Mkln1
Mllt11
Mlx
Mocs2
Mpc1
Mpv17l
Mrpl10
Mrpl13
Mrpl21
Mrpl52
Mrps23
Mrps33
Mrps35
Mrps7
Mtch1
mt-Rnr2
Myl12b
Nav2
Ncam1
Ncbp2
Ndrg4
Ndufa10
Ndufa9
Nsg2
Nudc
Nudt21
Nudt3
Nxf1
Nxph1
Ociad1
Ociad2
Ogdh
Olfm1
Opcml
Oxct1
Paf1
Paip2
Pank1
Papolg
Pccb
Pcdh7
Pcgf5
Pcmt1
Pcmtd1
Pcna
Pdpk1
Pdrg1
Peg3
Pgk1
Pigk
Pitpnm1
Pja2
Plcb1
Pmpcb
Polr2m
Ppdpf
Ppid
Ppm1h
Ppp3cb
Prkacb
Prkar1a
Prpf38b
Psma6
Psmb2
Psmc4
Psmd14
Ptprd
Purg
Rab11a
Rab11fip2
Rab21
Rab3a
Rab4b
Rabgap1l
Rac1
Rad23a
Ranbp1
Rasa1
Rbm17
Rbm25
Rbms3
Rer1
Rheb
Rpl15
Rpl21
Rpl27a
Rpl31
Rpl5
Rps15a
Rtfdc1
Rufy3
Sap30l
Schip1
Scoc
Sdha
Sec14l1
Sec24a
Selk
Sept11
Sept2
Shisa5
Skp1a
Slc1a1
Slc25a11
Slc25a3
Slc25a5
Slc25a51
Slc4a3
Slmo1
Snap91
Snrpa1
Snrpb
Snx27
Spag9
Srp72
Srrm1
Stau1
Stk39
Suclg1
Sv2a
Syt11
Taf10
Taf11
Tbc1d14
Tbcel
Tfg
Timm10b
Tm7sf2
Tmem126a
Tmem59
Tpm3
Tsnax
Ttc14
Tusc3
Uba1
Ube2e3
Ube2i
Ube2j2
Ube4b
Ubfd1
Ublcp1
Uck2
Uhrf2
Unc5c
Uqcrc2
Vamp2
Vapb
Vma21
Vps45
Wasf3
Wdr45b
Wipi2
Wsb2
Yif1b
Ywhae
Znrf1

Table 4-4. Local proteome: predicted structures commonly found in synaptic proteins.

SCOP	Structure name	Predicted proteins
b.36	PDZ domains	Apba1, Dlg2, Dlg4, Dvl1, Dvl3, Frmpd4, Gorasp2^, Grip1, Limk1, Lin7a, Magi1, Mast1, Mpp3, Ppp1r9b, Ptpn4, Rims1, Shank2, Shank3, Sipa1l1, Snx27, Synj2bp
c.37.1.1	Nucleotide and nucleoside kinases [includes GK]	Cacnb4, Cmpk1^, Dlg2, Dlg4, Hnrnpu^, Mpp3^, Ndufa10, Stxbp1^
b.34.2	SH3 domains	Abi1, Abi2, Amph, Arhgef4, Arhgef9, Bcar1, Cacnb4, Caskin1, Crk, Dlg2, Dlg4, Itsn1, Kalrn, Map3k10, Mapk8ip1, Mapk8ip2, Mcf2l, Mia3, Mpp3, Pacsin1, Rasa1, Rusc1, Sh3gl2, Sh3glb2, Shank2, Shank3, Sorbs2, Sptan1, Srgap3, Stam, Ubash3b, Vav3
b.55.1.1	PH domains	Abr, Adap2, Apbb1ip, Arap2, Arhgef4, Arhgef9, Cadps, Cdc42bpa^, Elmo1, Exoc8, Fgd4, Kalrn, Kif1a, Kif1b, Mcf2l, Nisch*^, Pdpk1, Psd, Rasa1, Sos2, Sphk2*^, Sptbn1, Sptbn2, Vav3
b.34.9.1	Tudor domains	A830010M20Rik*, Cic*, Slc25a12*, Trp53bp1
a.238	BAR domains	Amph, Appl1, Arfip2, Cog7*^, Dync1h1^, Exoc6b*^, Macf1*^, Mtss1l^, Pacsin1*^, Sh3gl2, Smarca2*^
a.40	CH domains	Camsap1, Ccdc88a*, Dmd, Macf1, Mapre1, Mapre2, Mical2, Nav2, Nav3, Parva, Parva^, Sptbn1, Sptbn2, Stxbp1^, Vav3

* new annotation (compared to Gene3D)

^ medium-confidence prediction (nearest neighbor distance ≤ 30); all others are high confidence (nearest neighbor distance ≤ 17.5)

Table 4-5. Local proteome: predicted transmembrane structures.

SCOP	Structure name	Predicted proteins
f.1	Toxins' membrane translocation domains	Bcl2l2, Wdfy3*
f.3	Light-harvesting complex subunits	Bnip3l*, Ntrk3*
f.13	Class A G protein-coupled receptor (GPCR)-like	Atp6v0a1*, Gabbr1*, Gpr162, Lgr5, Oprd1, Svop
f.14	Gated ion channels	D3Bwg0562e, Gabrb3, Gria1, Gria2, Grin1, Grin2b, Hcn1, Kcnh7, Kcnq5, Ndfip1*, Scn2a1, Scn8a
f.17	Transmembrane helix hairpin	Acsl6*, Ankfy1*, Atp5g1, Atp5g2, Atp5g3, Atp6v0e2*, Atp9a*, Cadm1*, Canx*, Cd84*, Chrdl1*, Emc4*, Epha6*, Ern1*, Gbp7*, Gm15487, Higd1a*, Higd2a*, Kcna1, Kcna2, Kcng3, Kcnq5, Krtcap2*, Lman2*, Lpgat1*, Mdga2*, Ppp2r5b*, Ptprd*, Rnf5*, Romo1*, Sec62*, Slc3a2*, Slitrk5*, Tmem14c*, Tmem167*, Tmem256*, Tmem258*, Ube2j2*, Ugt1a6a*, Vma21*, Vps35*
f.19	Aquaporin-like	Aqp4, Palm
f.21	Heme-binding four-helical bundle	Agtrap*, Kcnq2, Sdhc, Sdhd, Slc22a15, Slc4a3*, Tmem170b*, Tmem50b*
f.23	Single transmembrane helix	AI413582*, AY036118*, Abhd6*, Acsl4*, Ahcyl1, Anapc5*, Aplp2*, Arel1*, Armcx1*, Armcx2*, Atp1a3*, Atp1b1, Atp2a2*, Atp5j2*, B3gat1*, B3gat2*, Bcl2l2*, Bdnf*, Bsg*, Caly*, Ccpg1*, Cd84*, Cd99l2*, Cdadc1*, Cdh13*, Celf2*, Celf4*, Cend1*, Chd3*, Chd4*, Chp1, Chst2*, Clec2l*, Clip3*, Cnot6l*, Cntn1*, Comt*, Coro1c*, Cox4i1, Cox6a1, Cox6a2, Cox6c, Cox7a2, Cox7a2l, Cox7b, Cox7c, Cox8a, Crlf2*, Crtac1*, Csf2ra*, Cyb5*, Cyb5b*, Dlc1*, Dner*, Egf*, Elavl2*, Elmo1*, Enpp5*, Epha5*, Epha6*, Erbb4, Exo1*, Fam115a, Fam155a*, Fam174a*, Flrt2*, Foxp2*, Gabrb2*, Gabrg2*, Gdap1*, Gli3*, Gltpd2*, Gria1*, Gria2*, Grin3a*, Herc1*, Herc2*, Hsd17b12*, Hspa5*, Huwe1*, Ids*, Ier3ip1*, Itga1, Itga4*, Kcna1, Kcna2, Kcng3, Kcnq2*, Kcnq5, Klf9*, Lman2*, Lrrc4b*, Lrrc4c*, Lsamp*, Lypd1*, Macf1*, Mavs*, Mdga2*, Megf11, Mfap3l*, Mia3*, Mkrn1*, Mpc1*, Mpc2*, Mrpl9*, Myo5a, Ndufa1*, Ndufa4*, Ndufa9*, Ndufb2*, Ndufb3*, Ndufb8*, Ndufc1*, Ndufc2*, Nenf*, Nlgn1*, Nlgn2*, Nrxn1*, Nrxn2*, Nrxn3*, Ntrk2*, Ntrk3*, Opcml*, Pam*, Pcmtd1*, Pdgfrl*, Pigk*, Pitpnm1*, Plin3*, Pnkd*, Ppm1h*, Ppp2r5b*, Psd*, Ptprb*, Ptprs*, Pum2*, Pvrl3*, Rbm47, Rhot1*, Rnf130*, Robo2*, Rps2*, Rtn2*, Scn2a1*, Sec11c*, Sel1l*, Selt*, Serp2*, Serpina3k*, Sez6l2*, Slc22a15*, Slc25a12, Slc25a23*, Slc30a9*, Slc4a3, Slco1a1*, Slitrk5*, Smdt1*, Smim13*, Sparc*, Sparcl1*, Spock2*, Srl*, Synj2bp*, Syt15*, Tef*, Tmx4*, Tnrc6a*, Tomm20*, Tomm6*, Tor4a*, Tsc22d2*, Tusc3*, Txndc15*, Ubqln2*, Ugt1a6a*, Ulk2*, Unc5c*, Uqcr10, Uqcr11, Uqcrfs1, Uqcrq, Usmg5*, Usp34*, Wdfy3*, Xpo7*, Zeb2*
f.27	14 kDa protein of cytochrome	Uqcrb

	bc1 complex (Ubiquinol-cytochrome c reductase)	
f.28	Non-heme 11 kDa protein of cytochrome bc1 complex (Ubiquinol-cytochrome c reductase)	Uqcrh
f.32	a domain/subunit of cytochrome bc1 complex (Ubiquinol-cytochrome c reductase)	Grin3a*
f.35	Multidrug efflux transporter AcrB transmembrane domain	Disp2, Ptchd4
f.42	Mitochondrial carrier	Gda, Slc25a11, Slc25a12, Slc25a22, Slc25a23, Slc25a3, Slc25a4, Slc25a5, Slc25a51
f.45	Mitochondrial ATP synthase coupling factor 6	Atp5j*
f.49	Proton glutamate symport protein	Slc1a1, Slc1a2
f.51	Rhomboid-like	Slc17a9, Slc22a15, Slc22a17, Svop
f.53	ATP synthase D chain-like	Atp5h*, Gm10250*, Sptbn2
f.56	MAPEG domain-like	Abca5*, Cnih2*, Kcng3, Mgst3, Rabac1*, Sc4mol*, Timm17a*, Timm17b*
f.57	MgtE membrane domain-like	Disp2, Slc28a3*
f.58	MetI-like	Abca5*, Atp9a*, Mboat7*, Mmd*, Slc17a7, Slc23a1*, Slc28a3*, Slc2a13, Slc7a11*, Sv2a, Tlcd1*
f.59	Cation efflux protein transmembrane domain-like	Slc30a9

* new annotation (compared to Gene3D)
All predictions shown are high confidence (nearest neighbor distance ≤ 17.5)

Table 4-6. Local proteome: predicted RNA-binding structures.

Fold	Desc	Predicted proteins
a.144	PABP domain-like	Dync1h1*, Pabpc1
a.217	Surp module (SWAP domain)	Zc3h7b*
b.38	Sm-like fold	Atxn2, Lsm3, Lsmd1, Snrpb, Snrpn
b.40.4	OB-fold; Nucleic acid binding	Ccdc141, Cmip, Csdc2, Csde1, Dlst, Dnaaf2*, Eif5a, Gm10263, Pdgfrl, Polr2g, Polr3h, Rapgef4, Rpl6, Rps11, Rps23, Rps28, Trub2*, Ttc14, Ybx1, Zcchc17
d.265	Pseudouridine synthase	Rpusd4, Trub2
d.41	alpha/beta-Hammerhead	Aox3, Mocs2, Rpl10
d.50	dsRBD-like	Adarb1, Dhx9, Rps2, Stau1, Stau2
d.51	Eukaryotic type KH-domain (KH-domain type I)	Fubp1, Hnrnpk, Pcbp2
d.58.7	Canonical RNA binding domain (RBD) [RRM]	Alyref, Celf2, Celf4, Cnot4, Cpeb2, Cpsf6, Eif4h, Elavl2, Elavl3, Ewsr1, Fus, G3bp2, Hnrnpa1, Hnrnpa2b1, Hnrnpa3, Hnrnpab, Hnrnpm, Msi2, Ncbp2, Ncl, Nxf1, Pabpc1, Pabpn1, Ppargc1a, Ppargc1b, Rbfox1, Rbfox2, Rbm14, Rbm17, Rbm25, Rbm47, Rbms3, Slirp, Syncrip, Tnrc6a, Uhmk1, Zcrb1
g.66	CCCH zinc finger	Mbnl2, Mkrn1, Rc3h1, Rc3h2, Zc3h15, Zc3h7b

* new annotation (compared to Gene3D)
All predictions shown are high confidence (nearest neighbor distance ≤ 17.5)

Table 4-7. New structure predictions for domains with pathogenic variants in humans and memory/synapse-related phenotypes.

Gene	Domain	Fold Prediction	Phenotypes
App	712-770	[g.41] - Rubredoxin-like	abnormal learning/memory/conditioning;abnormal long term object recognition memory;abnormal long term potentiation;abnormal long term spatial reference memory;abnormal spatial learning;abnormal spatial reference memory;abnormal spatial working memory;abnormal synapse morphology;reduced long term potentiation
App^	452-671	[a.151] - Glutamyl tRNA-reductase dimerization domain	
Arx	396-564	[g.88] - Intrinsically disordered proteins	abnormal associative learning;abnormal spatial learning
Arx^	1-326	[a.8] - immunoglobulin/albumin-binding domain-like	
Asns	530-561	[a.118] - alpha-alpha superhelix	abnormal long term object recognition memory;abnormal short term object recognition memory
Atp13a2^	1-194	[d.14] - Ribosomal protein S5 domain 2-like	abnormal spatial learning;decreased memory-marker CD4-positive NK T cell number
Atp1a3	264-330	[f.23] - Single transmembrane helix	abnormal CNS synaptic transmission;abnormal miniature inhibitory postsynaptic currents;abnormal spatial learning
Atp1a3	386-423	[g.24] - TNF receptor-like	
Bdnf	1-134	[f.23] - Single transmembrane helix	abnormal CNS synaptic transmission;abnormal dendrite morphology;abnormal dendritic spine morphology;abnormal excitatory postsynaptic potential;abnormal inhibitory postsynaptic currents;abnormal synaptic plasticity;impaired synaptic plasticity;reduced long term potentiation
Braf	268-486	[g.37] - beta-beta-alpha zinc fingers	abnormal associative learning;abnormal long term object recognition memory;abnormal Purkinje cell dendrite morphology;abnormal spatial learning;reduced long term potentiation
Brd7^	257-651	[a.7] - Spectrin repeat-like	abnormal dendrite morphology;abnormal long term object recognition memory;abnormal short term object recognition memory;impaired spatial learning
Ctnnb1	1-134	[b.108] - Triple-stranded beta-helix	abnormal spatial reference memory;abnormal synaptic vesicle clustering;reduced long term potentiation
Dcdc2a^	223-475	[g.3] - Knottins (small inhibitors, toxins, lectins)	abnormal short term object recognition memory;abnormal spatial learning;abnormal spatial working memory
Dmd	2128-2172	[a.4] - DNA/RNA-binding 3-helical bundle	abnormal neuromuscular synapse morphology
Dmd	3082-3113	[a.4] - DNA/RNA-binding 3-helical bundle	
Dmd	1775-1813	[a.4] - DNA/RNA-binding 3-helical bundle	
Dmd	1377-1436	[a.60] - SAM domain-like	
Dmd	241-341	[b.108] - Triple-stranded beta-helix	
Dmd	671-723	[b.108] - Triple-stranded beta-helix	
Dmd	1968-2000	[b.34] - SH3-like barrel	
Dmd	905-944	[d.198] - Secretion chaperone-like	
Dmd	3286-3490	[g.39] - Glucocorticoid receptor-like (DNA-binding domain)	

Dnajc5^	93-198	[a.74] - Cyclin-like	abnormal neuromuscular synapse morphology;abnormal PNS synaptic transmission
Dnajc6	1-68	[a.118] - alpha-alpha superhelix	abnormal synaptic vesicle number;abnormal synaptic vesicle recycling
Dnajc6^	387-806	[g.39] - Glucocorticoid receptor-like (DNA-binding domain)	
Dnmt3a	419-637	[g.44] - RING/U-box	abnormal neuromuscular synapse morphology;decreased effector memory CD8-positive, alpha-beta T cell number;decreased effector memory CD8-positive, alpha-beta T cell number
Dtna	555-746	[d.198] - Secretion chaperone-like	abnormal neuromuscular synapse morphology
Erbb4	980-1308	[d.92] - Zincin-like	enhanced long term potentiation
Gad1^	1-209	[a.26] - 4-helical cytokines	abnormal excitatory postsynaptic potential;abnormal inhibitory postsynaptic currents
Gdap1	116-188	[a.6] - Putative DNA-binding domain	abnormal neuromuscular synapse morphology
Gdap1	300-358	[f.23] - Single transmembrane helix	
Gdi1	334-447	[c.3] - FAD/NAD(P)-binding domain	abnormal excitatory postsynaptic currents;abnormal excitatory postsynaptic potential;abnormal spatial working memory;abnormal synaptic glutamate release;abnormal synaptic vesicle number;decreased synaptic glutamate release
Gdi1	78-118	[d.16] - FAD-linked reductases, C-terminal domain	
Gnas^	1-300	[g.3] - Knottins (small inhibitors, toxins, lectins)	abnormal spatial learning;abnormal spatial working memory;enhanced long term potentiation
Gnas^	301-600	[g.3] - Knottins (small inhibitors, toxins, lectins)	
Gnas^	151-450	[g.39] - Glucocorticoid receptor-like (DNA-binding domain)	
Grin2b	914-1213	[a.118] - alpha-alpha superhelix	abnormal AMPA-mediated synaptic currents;abnormal associative learning;abnormal CNS synaptic transmission;abnormal dendrite morphology;abnormal dendritic spine morphology;abnormal discrimination learning;abnormal excitatory postsynaptic currents;abnormal excitatory postsynaptic potential;abnormal learning/memory/conditioning;abnormal long term object recognition memory;abnormal miniature excitatory postsynaptic currents;abnormal NMDA-mediated synaptic currents;abnormal object recognition memory;abnormal spatial learning;abnormal spatial reference memory;abnormal spatial working memory;abnormal synapse morphology;abnormal temporal memory;absence of NMDA-mediated synaptic currents;enhanced long term potentiation;fast extinction of fear memory;impaired synaptic plasticity;reduced long term potentiation
Grin2b	1064-1482	[g.39] - Glucocorticoid receptor-like (DNA-binding domain)	
Grin2b^	764-1063	[f.23] - Single transmembrane helix	
Hcn1^	1-147	[a.80] - post-AAA+ oligomerization domain-like	abnormal learning/memory/conditioning;abnormal motor learning;abnormal spatial learning
Ids	425-552	[d.19] - MHC antigen-recognition domain	abnormal spatial working memory
Ids	1-39	[f.23] - Single transmembrane helix	
Kcna1	412-495	[g.39] - Glucocorticoid receptor-like (DNA-binding domain)	abnormal CNS synaptic transmission;abnormal inhibitory postsynaptic currents;abnormal PNS synaptic transmission;abnormal synaptic transmission
Kif1a^	1203-1578	[b.2] - Common fold of diphtheria toxin/transcription factors/cytochrome f	abnormal synaptic vesicle clustering;abnormal synaptic vesicle number
Kif1a^	1053-1352	[b.40] - OB-fold	

Kif1b^	1093-1392	[b.1] - Immunoglobulin-like beta-sandwich	abnormal synaptic vesicle number
Kif1b^	1243-1542	[b.2] - Common fold of diphtheria toxin/transcription factors/cytochrome f	
Kif1b^	1393-1699	[d.3] - Cysteine proteinases	
Kif1b^	643-942	[d.43] - EF-Ts domain-like	
Mapk8ip1^	1-300	[g.3] - Knottins (small inhibitors, toxins, lectins)	abnormal NMDA-mediated synaptic currents
Mapt	301-733	[g.37] - beta-beta-alpha zinc fingers	abnormal dendrite morphology;abnormal long term object recognition memory;abnormal motor learning;abnormal spatial learning;abnormal spatial working memory;enhanced spatial learning;reduced long term potentiation
Mapt^	1-300	[g.3] - Knottins (small inhibitors, toxins, lectins)	
Mbd5^	1-300	[d.169] - C-type lectin-like	abnormal associative learning;abnormal dendrite morphology;abnormal excitatory postsynaptic currents;abnormal excitatory postsynaptic potential;abnormal learning/memory/conditioning;abnormal long term object recognition memory;abnormal miniature excitatory postsynaptic currents;abnormal miniature inhibitory postsynaptic currents;abnormal motor learning;abnormal spatial learning;abnormal synaptic vesicle number;decreased CNS synapse formation;reduced long term potentiation
Mecp2^	196-484	[g.3] - Knottins (small inhibitors, toxins, lectins)	
Mecp2^	1-66	[g.39] - Glucocorticoid receptor-like (DNA-binding domain)	
Mfn2	314-363	[a.6] - Putative DNA-binding domain	abnormal Purkinje cell dendrite morphology
Mfn2	1-84	[a.60] - SAM domain-like	
Mfn2^	430-694	[a.211] - HD-domain/PDEase-like	
Mid1	496-680	[b.29] - Concanavalin A-like lectins/glucanases	abnormal learning/memory/conditioning;abnormal motor learning
Mid1^	216-380	[a.7] - Spectrin repeat-like	
Nfkb2	850-899	[g.39] - Glucocorticoid receptor-like (DNA-binding domain)	abnormal myeloid dendritic cell morphology;abnormal spleen follicular dendritic cell network;decreased dendritic cell number;decreased myeloid dendritic cell number;increased plasmacytoid dendritic cell number
Ntrk2	376-530	[f.23] - Single transmembrane helix	abnormal avoidance learning behavior;abnormal dendrite morphology;abnormal excitatory postsynaptic potential;abnormal learning/memory/conditioning;abnormal long term potentiation;abnormal Purkinje cell dendrite morphology;abnormal spatial learning;abnormal spatial working memory;abnormal synapse morphology;impaired synaptic plasticity;reduced long term potentiation
Otc	1-31	[d.92] - Zincin-like	abnormal dendrite morphology;abnormal spatial learning;abnormal spatial reference memory;abnormal spatial working memory
Pafah1b1	1-100	[a.221] - Lissencephaly-1 protein (Lis-1, PAF-AH alpha) N-terminal domain	abnormal spatial learning
Pnkd	1-116	[f.23] - Single transmembrane helix	abnormal synaptic dopamine release;abnormal synaptic transmission
Psap	394-436	[a.118] - alpha-alpha superhelix	reduced long term potentiation
Psap^	1-58	[g.24] - TNF receptor-like	
Pten	354-403	[g.37] - beta-beta-alpha zinc fingers	abnormal CNS synaptic transmission;abnormal dendrite morphology;abnormal dendritic spine morphology;abnormal excitatory postsynaptic currents;abnormal excitatory postsynaptic potential;abnormal miniature excitatory
Pten	283-313	[g.5] - Midkine	

			postsynaptic currents;abnormal Purkinje cell dendrite morphology;abnormal synapse morphology;abnormal synaptic depression;abnormal synaptic transmission;abnormal synaptic vesicle number;impaired spatial learning
Pura^	1-321	[d.198] - Secretion chaperone-like	decreased CNS synapse formation
Reln	3135-3228	[b.121] - Nucleoplasmin-like/VP (viral coat and capsid)	abnormal short term spatial reference memory
Rims1^	704-1003	[g.3] - Knottins (small inhibitors, toxins, lectins)	abnormal CNS synaptic transmission;abnormal excitatory postsynaptic currents;abnormal excitatory postsynaptic potential;abnormal inhibitory postsynaptic currents;abnormal post-tetanic potentiation;impaired synaptic plasticity;reduced long term potentiation
Robo2	1164-1470	[a.118] - alpha-alpha superhelix	abnormal Purkinje cell dendrite morphology
Robo2	864-1163	[f.23] - Single transmembrane helix	
Robo2^	1014-1313	[g.3] - Knottins (small inhibitors, toxins, lectins)	
Scn8a	1468-1518	[d.372] - YqaI-like	abnormal neuromuscular synapse morphology
Scn8a^	417-750	[d.58] - Ferredoxin-like	
Scn8a^	980-1200	[d.6] - Prion-like	
Shank3	531-568	[b.72] - WW domain-like	abnormal CNS synaptic transmission;abnormal dendritic spine morphology;abnormal excitatory postsynaptic currents;abnormal excitatory postsynaptic potential;abnormal long term object recognition memory;abnormal miniature excitatory postsynaptic currents;abnormal miniature inhibitory postsynaptic currents;abnormal motor learning;abnormal object recognition memory;abnormal spatial learning;abnormal spatial reference memory;abnormal synapse morphology;abnormal synaptic transmission;decreased excitatory postsynaptic current amplitude;decreased post-tetanic potentiation;decreased synaptic depression;impaired learning;impaired spatial learning;impaired synaptic plasticity;reduced long term potentiation;reduced NMDA-mediated synaptic currents
Shank3^	963-1262	[g.39] - Glucocorticoid receptor-like (DNA-binding domain)	
Shank3^	1113-1412	[g.39] - Glucocorticoid receptor-like (DNA-binding domain)	
Slc6a1^	151-599	[f.13] - Class A G protein-coupled receptor (GPCR)-like	abnormal inhibitory postsynaptic currents;abnormal object recognition memory;abnormal spatial working memory
Slc6a1^	1-300	[f.21] - Heme-binding four-helical bundle	
Stxbp1^	324-361	[a.43] - Ribbon-helix-helix	abnormal synaptic transmission
Syn1^	393-706	[g.37] - beta-beta-alpha zinc fingers	abnormal CNS synapse formation;abnormal excitatory postsynaptic potential;abnormal inhibitory postsynaptic currents;abnormal synaptic vesicle clustering;abnormal synaptic vesicle recycling;delayed CNS synapse formation;increased synaptic depression
Synj1^	1-300	[b.50] - Acid proteases	increased synaptic depression
Synj1^	151-513	[c.55] - Ribonuclease H-like motif	
Tcf4^	151-556	[g.3] - Knottins (small inhibitors, toxins, lectins)	abnormal associative learning;impaired spatial learning
Tcf4^	1-300	[g.39] - Glucocorticoid receptor-like (DNA-binding domain)	
Thra	376-492	[a.4] - DNA/RNA-binding 3-helical bundle	abnormal object recognition memory;abnormal Purkinje cell dendrite morphology
Thra	1-51	[g.3] - Knottins (small inhibitors, toxins, lectins)	

Ube3a	721-755	[b.108] - Triple-stranded beta-helix	abnormal dendrite morphology;abnormal learning/memory/conditioning;abnormal long term potentiation;abnormal motor learning;abnormal spatial learning;reduced long term potentiation
Ube3a^	151-499	[a.288] - UraD-like	
Ube3a^	1-300	[d.389] - Menin N-terminal domain-like	

^ medium-confidence prediction (nearest neighbor distance ≤ 30); all others are high confidence (nearest neighbor distance ≤ 17.5)
All are new annotations (compared to Gene3D)

4.5 References

1 Martin, K.C. *et al.* (2000) Local protein synthesis and its role in synapse-specific plasticity. *Curr. Opin. Neurobiol.* 10, 587–592

2 Miyashiro, K. *et al.* (1994) On the nature and differential distribution of mRNAs in hippocampal neurites: implications for neuronal functioning. *Proc. Natl. Acad. Sci. U. S. A.* 91, 10800–4

3 Moccia, R. *et al.* (2003) An unbiased cDNA library prepared from isolated Aplysia sensory neuron processes is enriched for cytoskeletal and translational mRNAs. *J. Neurosci.* 23, 9409–17

4 Zhong, J. *et al.* (2006) Dendritic mRNAs encode diversified functionalities in hippocampal pyramidal neurons. *BMC Neurosci.* 7, 17

5 Poon, M.M. *et al.* (2006) Identification of process-localized mRNAs from cultured rodent hippocampal neurons. *J. Neurosci.* 26, 13390–9

6 Suzuki, T. *et al.* (2007) Characterization of mRNA species that are associated with postsynaptic density fraction by gene chip microarray analysis. *Neurosci. Res.* 57, 61–85

7 Cajigas, I.J. *et al.* (2012) The local transcriptome in the synaptic neuropil revealed by deep sequencing and high-resolution imaging. *Neuron* 74, 453–66

8 Ainsley, J.A. *et al.* (2014) Functionally diverse dendritic mRNAs rapidly associate with ribosomes following a novel experience. *Nat. Commun.* 5, 4510

9 Francis, C. *et al.* (2014) Divergence of RNA localization between rat and mouse neurons reveals the potential for rapid brain evolution. *BMC Genomics* 15, 883

10 Taliaferro, J.M. *et al.* (2016) Distal Alternative Last Exons Localize mRNAs to Neural Projections. *Mol. Cell* 61, 821–833

11 Lovatt, D. *et al.* (2014) Transcriptome in vivo analysis (TIVA) of spatially defined single cells in live tissue. *Nat. Methods* 11, 190–6

12 Lubeck, E. *et al.* (2014) Single-cell in situ RNA profiling by sequential hybridization. *Nat. Methods* 11, 360–1

13 Lee, J.H. *et al.* (2014) Highly Multiplexed Subcellular RNA Sequencing in Situ. *Science* 1360,

14 Chen, K.H. *et al.* (2015) Spatially resolved, highly multiplexed RNA profiling in single cells. *Science* 1363, 1360–1363

15 Dueck, H. *et al.* (2015) Deep sequencing reveals cell-type-specific patterns of single-cell transcriptome variation. *Genome Biol.* 16, 122

16 Bramham, C.R. and Wells, D.G. (2007) Dendritic mRNA: transport, translation and function. *Nat. Rev. Neurosci.* 8, 776–789

17 Gerstberger, S. *et al.* (2014) A census of human RNA-binding proteins. *Nat. Rev. Genet.* 15, 829–845

18 Buckley, P.T. *et al.* (2011) Cytoplasmic intron sequence-retaining transcripts can be dendritically targeted via ID element retrotransposons. *Neuron* 69, 877–84

19 Miura, P. *et al.* (2013) Widespread and extensive lengthening of 3' UTRs in the mammalian brain. *Genome Res.* 23, 812–25

20 Miller, S. *et al.* (2002) Disruption of Dendritic Translation of CaMKIIα Impairs Stabilization of Synaptic Plasticity and Memory Consolidation. *Neuron* 36, 507–519

21 Timmons, J. a. *et al.* (2015) Multiple sources of bias confound functional enrichment analysis of global -omics data. *Genome Biol.* 16, 186

22 Kim, E. and Sheng, M. (2004) PDZ domain proteins of synapses. *Nat. Rev. Neurosci.* 5, 771–781

23 Dalva, M.B. *et al.* (2007) Cell adhesion molecules: signalling functions at the synapse. *Nat. Rev. Neurosci.* 8, 206–220

24 Zheng, C.-Y. *et al.* (2011) MAGUKs, Synaptic Development, and Synaptic Plasticity. *Neurosci.* 17, 493–512

25 Liu-Yesucevitz, L. *et al.* (2011) Local RNA translation at the synapse and in disease. *J. Neurosci.* 31, 16086–93

26 Grant, S.G. (2012) Synaptopathies: diseases of the synaptome. *Curr. Opin. Neurobiol.* 22, 522–529

27 Love, M.I. *et al.* (2014) Moderated estimation of fold change and dispersion for RNA-seq data with DESeq2. *Genome Biol.* 15, 550

28 Miura, P. *et al.* (2014) Alternative polyadenylation in the nervous system: To what lengths will 3' UTR extensions take us? *Bioessays* DOI: 10.1002/bies.201300174

29 An, J.J. *et al.* (2008) Distinct Role of Long 3’ UTR BDNF mRNA in Spine Morphology and Synaptic Plasticity in Hippocampal Neurons. *Cell* 134, 175–187

30 Liao, G.-Y. *et al.* (2012) Dendritically targeted Bdnf mRNA is essential for energy balance and response to leptin. *Nat. Med.* 18, 564–571

31 Brenner, C. (2010) , HOMER: Software for motif discovery and next generation sequencing analysis. . [Online]. Available: http://homer.ucsd.edu

32 Heinz, S. *et al.* (2010) Simple Combinations of Lineage-Determining Transcription Factors Prime cis-Regulatory Elements Required for Macrophage and B Cell Identities. *Mol. Cell* 38, 576–589

33 Ray, D. *et al.* (2013) A compendium of RNA-binding motifs for decoding gene regulation. *Nature* 499, 172–7

34 Ray, D. *et al.* (2009) Rapid and systematic analysis of the RNA recognition specificities of RNA-binding proteins. *Nat. Biotechnol.* 27, 667–670

35 Müller-McNicoll, M. *et al.* (2016) SR proteins are NXF1 adaptors that link alternative RNA processing to mRNA export. *Genes Dev.* 30, 553–566

36 Martin, K.C. and Ephrussi, A. (2009) mRNA Localization: Gene Expression in the Spatial Dimension. *Cell* 136, 719–730

37 Medioni, C. *et al.* (2012) Principles and roles of mRNA localization in animal development. *Development* 139, 3263–3276

38 Subramanian, M. *et al.* (2011) G-quadruplex RNA structure as a signal for neurite mRNA targeting. *EMBO Rep.* 12, 697–704

39 Schofield, J.P.R. *et al.* (2015) G-quadruplexes mediate local translation in neurons. *Biochem. Soc. Trans.* 43, 338–42

40 Darnell, J.C. *et al.* (2011) FMRP stalls ribosomal translocation on mRNAs linked to synaptic function and autism. *Cell* 146, 247–61

41 Smit, A. *et al.* (2013) , RepeatMasker Open-4.0. . [Online]. Available: http://www.repeatmasker.org

42 Gruber, A.R. *et al.* (2008) The Vienna RNA Websuite. *Nucleic Acids Res.* 36, W70–W74

43 Espinoza, C.A. *et al.* (2007) Characterization of the structure, function, and mechanism of B2 RNA, an ncRNA repressor of RNA polymerase II transcription. *RNA* 13, 583–596

44 Tenenbaum, S.A. *et al.* (2011) The post-transcriptional operon. *Methods Mol. Biol.* 703, 237–245

45 Heraud-Farlow, J.E. *et al.* (2013) Staufen2 regulates neuronal target RNAs. *Cell Rep.* 5, 1511–1518

46 Muslimov, I. a. *et al.* (2014) Interactions of noncanonical motifs with hnRNP A2 promote activity-dependent RNA transport in neurons. *J. Cell Biol.* 205, 493–510

47 Muslimov, I.A. *et al.* (2006) Spatial codes in dendritic BC1 RNA. *J. Cell Biol.* 175, 427–439

48 Muslimov, I. a *et al.* (2011) Spatial code recognition in neuronal RNA targeting: role of RNA-hnRNP A2 interactions. *J. Cell Biol.* 194, 441–57

49 The UniProt Consortium (2017) UniProt: the universal protein knowledgebase. *Nucleic Acids Res.* 45, D158–D169

50 Lees, J. *et al.* (2012) Gene3D: A domain-based resource for comparative genomics, functional annotation and protein network analysis. *Nucleic Acids Res.* 40, 465–471

51 Protter, D.S.W. and Parker, R. (2016) Principles and Properties of Stress Granules. *Trends Cell Biol.* 26, 668–679

52 Petersen, T.N. *et al.* (2011) SignalP 4.0: discriminating signal peptides from transmembrane regions. *Nat. Methods* 8, 785–6

53 Nguyen, P. *et al.* (1994) Requirement of a critical period of transcription for induction of a late phase of LTP. *Science (80-.).* 265, 1104–1107

54 Crino, P. *et al.* (1998) Presence and phosphorylation of transcription factors in developing dendrites. *Proc. Natl. Acad. Sci.* 95, 2313–2318

55 Buckley, P.T. *et al.* (2013) Cytoplasmic intron retention, function, splicing, and the sentinel RNA hypothesis. *Wiley Interdiscip. Rev. RNA* DOI: 10.1002/wrna.1203

56 Vissel, B. *et al.* (2001) The Role of RNA Editing of Kainate Receptors in Synaptic Plasticity and Seizures. *Neuron* 29, 217–227

57 Hood, J.L. and Emeson, R.B. (2012) Editing of Neurotransmitter Receptor and Ion Channel RNAs in the Nervous System. *Curr. Top. Microbiol. Immunol.* 353, 61–90

58 Smith, C.L. and Eppig, J.T. (2009) The mammalian phenotype ontology: enabling robust annotation and comparative analysis. *Wiley Interdiscip. Rev. Syst. Biol.*

Med. 1, 390–399

59 Adzhubei, I.A. *et al.* (2010) A method and server for predicting damaging missense mutations. *Nat. Methods* 7, 248–249

60 Tongiorgi, E. *et al.* (1997) Activity-dependent dendritic targeting of BDNF and TrkB mRNAs in hippocampal neurons. *J. Neurosci.* 17, 9492–9505

61 Steward, O. *et al.* (1998) Synaptic activation causes the mRNA for the IEG Arc to localize selectively near activated postsynaptic sites on dendrites. *Neuron* 21, 741–751

62 Eberwine, J. *et al.* (2001) Local translation of classes of mRNAs that are targeted to neuronal dendrites. *Proc. Natl. Acad. Sci.* 98, 7080–7085

63 Yoon, Y.J. *et al.* (2016) Glutamate-induced RNA localization and translation in neurons. *Proc. Natl. Acad. Sci.* 113, E6877–E6886

64 Buchhalter, J.R. and Dichter, M.A. (1991) Electrophysiological comparison of pyramidal and stellate nonpyramidal neurons in dissociated cell culture of rat hippocampus. *Brain Res. Bull.* 26, 333–338

65 Morris, J. *et al.* (2011) Transcriptome analysis of single cells. *J. Vis. Exp.* DOI: 10.3791/2634

66 Dobin, A. *et al.* (2013) STAR: ultrafast universal RNA-seq aligner. *Bioinformatics* 29, 15–21

67 Zhu, Q. *et al.* (2016) VERSE: a versatile and efficient RNA-Seq read counting tool. *bioRxiv* DOI: https://doi.org/10.1101/053306

68 Zhang, Y. *et al.* (2014) An RNA-Sequencing Transcriptome and Splicing Database of Glia, Neurons, and Vascular Cells of the Cerebral Cortex. *J. Neurosci.* 34, 11929–11947

69 Eden, E. *et al.* (2009) GOrilla: a tool for discovery and visualization of enriched GO terms in ranked gene lists. *BMC Bioinformatics* 10, 48

70 Middleton, S.A. and Kim, J. (2014) NoFold: RNA structure clustering without folding or alignment. *RNA* 20, 1671–1683

71 Yeats, C. *et al.* (2010) A fast and automated solution for accurately resolving protein domain architectures. *Bioinformatics* 26, 745–751

72 Landrum, M.J. *et al.* (2016) ClinVar: public archive of interpretations of clinically relevant variants. *Nucleic Acids Res.* 44, D862–D868

73 Kerpedjiev, P. *et al.* (2015) Forna (force-directed RNA): Simple and effective online RNA secondary structure diagrams. *Bioinformatics* 31, 3377–3379

74 Lai, D. *et al.* (2012) R-CHIE: a web server and R package for visualizing RNA secondary structures. *Nucleic Acids Res.* 40, e95–e95

Chapter 5: Conclusions and future directions

The incorporation of structure information into routine bioinformatics analysis has been hindered by a lack of tools that can analyze structure on a large scale. In this thesis, I described two novel methods for characterizing macromolecular structure that utilize the idea of empirical feature spaces to improve accuracy and scalability. I then applied these methods to address long-standing open questions in neuron biology regarding localization and translation in the dendrites, which has significance for our understanding of long-term potentiation and learning and memory. These results include findings that would have been more difficult to obtain without structure analysis, including the identification of B1 and B2-derived hairpin structures in localized 3’UTRs, and new predictions RBPs and RNA binding domains (RBDs) among locally-translated proteins. Altogether, this work demonstrates the utility of structure-based analysis of macromolecules and provides two scalable methods to implement such analyses in standard bioinformatics pipelines. In the discussion below, I highlight some important avenues for follow-up work, including areas where structure-based analysis of RNA and protein could be particularly fruitful.

Role of alternative 3'UTRs in RNA localization

Neurons clearly have special RNA localization needs compared to other cell types. Their unique morphology—long, extended processes that can be many times the length of the soma—combined with an extensive need for local translation means that neurons must transport a wide variety of RNAs long distances from their origination point in the nucleus. In Chapter 4, we found almost 300 genes with alternative 3' isoforms where one isoform was consistently more dendritically localized than the other. There are several reasons why the use of alternative 3'UTRs is an attractive model for how neurons might regulate localization. Firstly, it provides the neuron with a mechanism for localizing only a subset of the transcripts of a given gene. This is potentially critical for any genes where the RNA and/or protein is needed in the soma in addition to the dendrites. Secondly, localizing only a subset of gene isoforms allows neurons to potentially regulate the localization of RNAs using co-transcriptional mechanisms, such as controlling the level of splicing factors that promote inclusion/exclusion of the localized isoform. Finally, alternative 3'UTRs theoretically have the potential to provide an element of tissue-specificity to localization, since cell types that have no need to localize a particular RNA can simply not express the localized isoform. However, in contrast to this idea, we did not observe a high level of tissue-specificity among the neurite-targeted 3' isoforms. Specifically, of the 38 neurite-targeted isoforms we identified that were among the new 3'UTRs annotated by Miura *et al.* [1], only 12 were specific to hippocampal neurons according to the Miura data. The other 26 isoforms were found in at least one of the other mouse tissue types profiling in that study, which included spleen, liver, thymus, lung, and heart [1]. This suggests that regulation of alternative 3’UTR usage may not be the main mechanism of generating tissue-specific localization. Another way that tissue-specific localization might be achieved is through the regulated expression of the *trans* factors needed for localization, e.g. certain RBPs or transport components. Overall, more work is needed to determine how differentially localized 3’ isoforms are regulated in neurons. It will be interesting to see if any other structural motifs can be found in the RNAs that might play a role in regulating splicing patterns, such that a neuron can trigger the inclusion or exclusion of DTE-containing 3’ exons, depending on its localization needs.

RBPs in dendritic localization

Although we focused our attention here on identifying the *cis* elements involved in dendritic localization—i.e. linear and structural DTEs found on the RNA itself—the RBP *trans* factors that bind these elements are likely to be just as important for a full understanding of RNA localization. RBPs appear to be hotspots for mutations associated with neuropsychiatric disorders [2,3], including several with putative roles in localization, suggesting that errors in RNA localization could be major mechanism underlying disease. A more complete understanding of the interactions between localization-mediating RBPs and the DTEs they bind is therefore needed. Several experimental methods are now being used to profile these interactions transcriptome-wide, such as crosslinking immunoprecipitation (CLIP)-based methods to identify the RNAs bound by specific RBPs [4–6], peptide nucleic acid (PNA)-assisted identification of RBPs (PAIR) to identify the RBPs associated with a specific RNAs [7], as well as methods that profile protein-bound RNA more broadly [8]. Although these methods reveal which RNAs are RBP-bound and sometimes even the location of the binding sites, they usually only provide limited information about the motifs recognized by the RBP. Often only a short, degenerate linear motif is identified (e.g. "YGCY" for Mbnl1 [9] and "UCAY" for Nova [10]). More sophisticated tools for determining binding motifs that incorporate both sequence and structure will need to be applied to fully capture the binding preferences of RBPs (this will be discussed further below). In order to make useful predictions about mutations that could disrupt the interaction between localization-mediating RBPs and their targets, we will need more accurate models of the structure of both the RBP binding domain(s) and the RNA binding site. In addition, a more complete definition of which RBPs are involved in localization will help focus such studies.

Neo-functionalization of transposable elements

The results of the RNA structure motif analysis in Chapter 4 suggested that B1 and B2 SINE elements could play a role in localization in mouse neurons. Such neo-functionalizations of transposable elements have been described previously in several other contexts, and are hypothesized to be one of the major sources of new functional genomic elements [11–15]. In particular, as mentioned previously, it had been shown that another type of SINE called the ID element—derived from the dendritically-localized ncRNA BC1—caused localization of RNAs to the dendrites in rat [16–18]. Interestingly, however, this localization was not reproduced in mice [19,20], suggesting that it could be a rat-specific innovation. Supporting this hypothesis is the fact that ID elements have undergone greater expansion in rat compared to mouse, with over 100x more instances in rat [17]. In the same study, it was found that B2 elements did not cause dendritic localization in rat [17]. Localization ability of B1 and B2 elements have not yet been experimentally tested in mouse, but given the divergence of functionality observed for ID elements between rodents, a similar divergence for B1 and/or B2 elements should not be ruled out. The possibility of analogous, yet non-homologous elements performing similar roles in different species has been noted before, both for transposons and non-transposon motifs [14,21]. Therefore, it is worth investigating whether a similar analogous-but-not-homologous relationship exists for ID elements and B1/B2 elements in the context of dendritic localization.

If B1/B2 elements drive dendritic localization in mice and ID elements drive localization in rats, what element might fill this role in humans? Several lines of evidence point to *Alu* elements being a likely candidate. *Alu* elements are primate-specific SINE retrotransposons that make up almost 11% of the human genome [22]. They are originally derived from 7SL RNA, which is part of the signal recognition RNP and plays a role in the processing and localization of proteins with signal peptides. In humans, *Alu* elements show "exonization" activity, where an *Alu* element within an intron becomes an exon via activation of the cryptic splice sites contained in the *Alu* sequence [22]. Relevant to our previous discussion of the role of alternative 3'UTRs in localization, it has also been found that *Alu* elements located downstream of a gene can generate new alternative 3'UTRs by alternative splicing or alternative cleavage and polyadenylation, and furthermore, that these *Alu*-derived 3'UTRs tend to be tissue specific [15]. Most notably of all, a potential role for an *Alu*-derived element in dendritic localization has already been described: BC200, a ncRNA that likely originated from an *Alu* element, shows dendritic localization patterns highly similar to BC1 RNA in rodents [23]. Since no homolog of BC1 has been found in humans, BC200 is often described as the primate "analog" of BC1. *Alu* elements appear to fill analogous roles for other types of rodent SINEs as well, including mouse B2 SINE RNA in repression of Pol II during heat shock [24]. Overall, there appear to be many points of convergence between these different classes of SINE elements in mouse, rat, and human, despite their distinct evolutionary origins and extensive species-specific expansions and insertions. Further exploration of the potential role of *Alu* elements in human dendritic localization will be an important area for future work.

Function of locally translated proteins in L-LTP

A crucial remaining question is what role individual locally translated proteins play in long-lasting synaptic potentiation. Part of the difficulty of answering this question is the need to ensure that any method used to block the translation of an RNA is specific to the RNA in question and only affects RNA in the dendrites—the somatic translation should be left intact. For CaMKIIα, this was accomplished by deleting the region of the 3'UTR that contained the DTE, thus blocking local translation via abolishing localization. With better definition of DTEs, it will become possible to perform this sort of analysis across more RNAs and with greater specificity—i.e. removing only the DTE rather than large regions of the 3'UTR.

Another interesting question is *when* proteins are locally translated. Are certain subsets translated constitutively? How long after synaptic activation does local translation of different RNAs occur? Is there any sequential order to the translation of different RNAs after synaptic activation? Methods that monitor translation in real time with spatial precision will be helpful to answer these questions [25,26]. Real-time translation data has been reported for a handful of specific RNAs so far [27–31], and it will be particularly interesting to see local translation profiled on a larger scale.

Beyond neurons: other applications of structure analysis

Macromolecular structure plays an important role in all tissues and cellular pathways, and thus there is no shortage of areas where large-scale structure-based analysis can shed new light. For mRNAs, any co-regulated group of transcripts likely shares a common motif that is recognized by the regulating RBP, and many of these motifs are likely to have structural characteristics. Structure-aware *de novo* motif finding tools such as NoFold can be applied to these transcripts to identify binding motifs. Examples could include identification of structure motifs in the 3'UTR that increase or decrease mRNA stability, structures that promote exon inclusion or exclusion, or structures that enhance or repress translation.

For proteins, fast and sensitive methods for predicting tertiary structure from amino acid sequence will continue to be of vital importance as the number of protein sequences in databases grows. Although some structural folds are relatively easy to identify using linear information (e.g. HMM-based methods like Gene3D and Pfam), other folds are so diverse on the sequence level that they can sometimes only be identified using higher-order structure information (e.g. threading-based methods). An example of this is the Piwi domain—an RNA endonuclease structure found in the PIWI and Argonaut families of proteins, among others. The Piwi domain has a conserved structure, but the sequences that form this structure are highly diverse [32,33] (see also the CATH entry for this structure: [34]), making it difficult to identify based on sequence alone. Structural feature spaces such as the PESS are well suited for classification tasks such as this. The PESS can also be used as a rapid structure-based query system, as demonstrated with the hedgehog-related proteins in Chapter 3. In this framework, a whole proteome that has already been mapped to the PESS can be quickly queried for the closest structural matches to a domain of interest. Although the initial set up of the whole-proteome database is time consuming (requiring threading all domains in the proteome against the 1,814 templates, as described in Chapter 3), this step only needs to be performed once. Thereafter, all "queries" to the database require only threading of the query, and then a rapid nearest neighbor-based search of the PESS to retrieve the closest matches. We have already created PESS databases for the human and *C. elegans* proteomes, as well as a large portion of the mouse proteome (neuronally-expressed genes), and so queries to these proteomes are already possible.

Remaining challenges for structure prediction

The ability to predict the RNA motifs bound by RBPs with high accuracy is a major area of future improvement. An ideal method would include primary, secondary, and tertiary structure information, since all of these levels can be important for determining the affinity of an RBP for a particular RNA. Furthermore, future methods need to more fully take into account the way in which RBPs bind. Typically, an RBP contains multiple RBDs, each of which bind relatively weakly to their target motifs, and it is the *combination* of multiple bound RBDs that give an RBP its specificity and strengthens the interaction with the RNA [35]. For example, RNA recognition motif (RRM) RBDs typically recognize only 4-8nt, often with some degree of ambiguity of the exact recognition motif [36]. In order to gain greater specificity, most RBPs with RRM domains contain multiple such domains [35]. The implication is that in order to fully characterize the binding preferences of an RBP, one must look for multiple motifs. To make matters even more complicated, it is likely that the space between the motifs on the RNA is also important for recognition. The particular spacing needed will depend on the relative orientation and flexibility of the RBDs within the RBP: if two RBDs have a relatively short linker sequence between them, they may be fairly rigid and require a very specific distance between the two RNA motifs for binding; on the other hand, if two RBDs have a long, flexible linker between them, they could be more tolerant to the spacing between the RNA motifs. RNA structure and flexibility may also need to be taken into account. As a final layer of complexity, there are many cases where structural conformations change during binding. In this type of binding, called “induced fit”, the RNA or RBP (or both) starts off in one conformation—typically a flexible or disordered state—and then changes in structure upon binding [37]. An example of this is the "zipcode" RNA motif and its RBP partner, ZBP1, which are involved in dendritic localization of β-actin RNA. Initially, the region of the β-actin RNA that contains the zipcode sequence exists in an unfolded state, but then takes on more stable secondary structure by looping around ZBP1 [38]. Altogether, the interactions between RNA and RBPs are clearly complex and will require sophisticated tools to predict with accuracy in a reasonable amount of time. In the meantime, methods that aid in predicting secondary structure motifs of RNA and tertiary structural folds of RBPs bring us a step closer to a complete picture.

In terms of protein structure prediction, one of the greatest challenges still remaining is accurate prediction of domain boundaries based on protein sequence. Segmenting a protein into domains is the first step of many protein structure prediction methods, and is particularly crucial (and particularly difficult) when there is little sequence similarity between the query and any structurally solved protein. Improper domain segmentation was one of the major sources of low-confidence predictions in our classification of the human proteome (Chapter 3). Improvements in this area will be key for higher quality predictions downstream.

Conclusion

Macromolecules can only be fully understood if they are considered in the context of both their sequence and structural characteristics. In this thesis, I have demonstrated several ways that computational structure analysis can lead to new insights and make testable predictions, and more generally help make sense of the huge amount of sequence data that is now commonplace in genomics experiments. There are still many improvements that can be made, and experimental follow up will often be needed to verify predictions. Nonetheless, there is little doubt that structure analysis tools that can handle large-scale datasets will be instrumental to the field of genomics as it continues to mature.

References

1 Miura, P. *et al.* (2013) Widespread and extensive lengthening of 3’ UTRs in the mammalian brain. *Genome Res.* 23, 812–25

2 Liu-Yesucevitz, L. *et al.* (2011) Local RNA translation at the synapse and in disease. *J. Neurosci.* 31, 16086–93

3 Nussbacher, J.K. *et al.* (2015) RNA-binding proteins in neurodegeneration: Seq and you shall receive. *Trends Neurosci.* DOI: 10.1016/j.tins.2015.02.003

4 Ule, J. *et al.* (2003) CLIP identifies Nova-regulated RNA networks in the brain. *Science* 302, 1212–5

5 Licatalosi, D.D. *et al.* (2008) HITS-CLIP yields genome-wide insights into brain alternative RNA processing. *Nature* 456, 464–9

6 Hafner, M. *et al.* (2010) Transcriptome-wide identification of RNA-binding protein and microRNA target sites by PAR-CLIP. *Cell* 141, 129–41

7 Zielinski, J. *et al.* (2006) In vivo identification of ribonucleoprotein-RNA interactions. *Proc. Natl. Acad. Sci. U. S. A.* 103, 1557–62

8 Silverman, I.M. *et al.* (2014) RNase-mediated protein footprint sequencing reveals protein-binding sites throughout the human transcriptome. *Genome Biol.* 15, R3

9 Goers, E.S. *et al.* (2010) MBNL1 binds GC motifs embedded in pyrimidines to regulate alternative splicing. *Nucleic Acids Res.* 38, 2467–2484

10 Jensen, K.B. *et al.* (2000) The tetranucleotide UCAY directs the specific recognition of RNA by the Nova K-homology 3 domain. *Proc. Natl. Acad. Sci. U. S. A.* 97, 5740–5

11 McDonald, J.F. (1995) Transposable elements: possible catalysts of organismic evolution. *Trends Ecol. Evol.* 10, 123–126

12 Brosius, J. (1999) RNAs from all categories generate retrosequences that may be exapted as novel genes or regulatory elements. *Gene* 238, 115–134

13 Jordan, I.K. *et al.* (2003) Origin of a substantial fraction of human regulatory sequences from transposable elements. *Trends Genet.* 19, 68–72

14 G, B. *et al.* (2008) Evolution of the mammalian transcription factor binding repertoire via transposable elements. DOI: 10.1101/gr.080663.108.These

15 Tajnik, M. *et al.* (2015) Intergenic Alu exonisation facilitates the evolution of tissue-specific transcript ends. *Nucleic Acids Res.* 43, gkv956

16 Muslimov, I.A. *et al.* (2006) Spatial codes in dendritic BC1 RNA. *J. Cell Biol.* 175, 427–439

17 Buckley, P.T. *et al.* (2011) Cytoplasmic intron sequence-retaining transcripts can be dendritically targeted via ID element retrotransposons. *Neuron* 69, 877–84

18 Muslimov, I. a. *et al.* (2014) Interactions of noncanonical motifs with hnRNP A2 promote activity-dependent RNA transport in neurons. *J. Cell Biol.* 205, 493–510

19 Khanam, T. *et al.* (2007) Can ID repetitive elements serve as cis-acting dendritic targeting elements? An in vivo study. *PLoS One* 2, e961

20 Robeck, T. *et al.* (2016) BC1 RNA motifs required for dendritic transport in vivo. *Sci. Rep.* 6, 28300

21 Tsirigos, A. and Rigoutsos, I. (2008) Human and mouse introns are linked to the same processes and functions through each genome's most frequent non-conserved motifs. *Nucleic Acids Res.* 36, 3484–3493

22 Deininger, P. *et al.* (2011) Alu elements: know the SINEs. *Genome Biol.* 12, 236

23 Tiedge, H. *et al.* (1993) Primary structure, neural-specific expression, and dendritic location of human BC200 RNA. *J. Neurosci.* 13, 2382–2390

24 Espinoza, C.A. *et al.* (2007) Characterization of the structure, function, and mechanism of B2 RNA, an ncRNA repressor of RNA polymerase II transcription. *RNA* 13, 583–596

25 Wu, B. *et al.* (2016) Translation dynamics of single mRNAs in live cells and neurons. *Science (80-.).* 1084,

26 Morisaki, T. *et al.* (2016) Real-time quantification of single RNA translation dynamics in living cells. *Science (80-.).* 899, 1–10

27 Aakalu, G. *et al.* (2001) Dynamic visualization of local protein synthesis in hippocampal neurons. *Neuron* 30, 489–502

28 Raab-Graham, K.F. *et al.* (2006) Activity- and mTOR-Dependent Suppression of Kv1.1 Channel mRNA Translation in Dendrites. *Science (80-.).* 314, 144–148

29 Wang, D.O. *et al.* (2009) Synapse- and stimulus-specific local translation during long-term neuronal plasticity. *Science* 324, 1536–40

30 Swanger, S.A. *et al.* (2013) Dendritic GluN2A Synthesis Mediates Activity-Induced NMDA Receptor Insertion. *J. Neurosci.* 33, 8898–8908

31 Kim, T.K. *et al.* (2013) Dendritic glutamate receptor mRNAs show contingent local hotspot-dependent translational dynamics. *Cell Rep.* 5, 114–25

32 Burroughs, A.M. *et al.* (2013) Two novel PIWI families: roles in inter-genomic conflicts in bacteria and Mediator-dependent modulation of transcription in eukaryotes. *Biol. Direct* 8, 13

33 Swarts, D.C. *et al.* (2014) The evolutionary journey of Argonaute proteins. *Nat Struct Mol Biol* 21, 743–753

34 CATH CATH Superfamily 3.40.50.2300. . [Online]. Available: http://www.cathdb.info/version/v4_1_0/superfamily/3.40.50.2300

35 Lunde, B.M. *et al.* (2007) RNA-binding proteins: modular design for efficient function. *Nat. Rev. Mol. Cell Biol.* 8, 479–90

36 Maris, C. *et al.* (2005) The RNA recognition motif, a plastic RNA-binding platform to regulate post-transcriptional gene expression. *FEBS J.* 272, 2118–2131

37 Williamson, J.R. (2000) Induced fit in RNA-protein recognition. *Nat. Struct. Biol.* 7, 834–837

38 Patel, V.L. *et al.* (2012) Spatial arrangement of an RNA zipcode identifies mRNAs under post-transcriptional control. *Genes Dev.* 26, 43–53